UNIVERSITAT POLITÈCNICA DE CATALUNYA BARCELONATECH

PhD program in ELECTRICAL ENGINEERING

Enhance of SOGI-FLL and SOGI-PLL response to voltage sags and swells perturbations

Doctoral thesis by:

Sajad Abdali Nejad

Thesis advisor:

José Matas Alcalá

Co-supervisor:

Jordi de La Hoz

ELECTRICAL ENGINEERING

Barcelona, 11/03/2022

Contents

1. Setting the context

The aim of this work is to contribute to the power quality of the grid by improving the response of grid monitoring systems to grid distortions. To this purpose, the response of different grid monitoring methods had been assessed and, in particular, the response to voltage sags, induced by faults in the grid, is concluded to be a challenge, since it can have a deep impact in the estimate frequency provided by these methods. Therefore, initially, the thesis has been focused into improving the impact that voltage sags have specifically for the SOGI-FLL structure, due to the simplicity of this structure. Then, the main objective it is to propose strategies and changes in the operation of the SOGI-FLL to minimize the impact of voltage sags in the dynamic behavior of the system. Furthermore, during the development of this work, it has been found that that this problem is also correlated to the impact that voltage swells have in the SOGI-FLL. Then, the developed strategies and changes in the operation for voltage sags had been also extended for voltages swells, despite the fact the impact of voltage swells in the estimated frequency is less strong that in the case of voltage sags. And, finally, the final adopted approach for the SOGI-FLL has been applied to the SOGI-PLL structure with some modifications. The results achieved for this case are satisfactory, showing that the approach improves the performance in front of voltage sags and swells.

2. Problem definition and thesis justification

2.1. Power quality issues

This section intends to briefly present some of the most common power quality issues related to the electric network. The power quality of the grid network is a multifactorial issue that involves all the parts of the system, such as generation, transmission, distribution, and load consumption. Power quality is an attempt to guarantee high standards for the supplied energy. Ideally, the provided voltages should have a sinusoidal waveform with low distortion levels, and its frequency and amplitude should range within small margins around nominal values. This implies measuring the amplitude voltages, frequency, and phases of the network to determine how much are deviated from the expected values, which allows adopting correction actions and ensuring operation inside the quality margins.

The main problems that distort the grid and worsen power quality are caused by unpredictable events like faults that might lead customers to lack service. Another source of issues is the interaction produced between the grid elements, like motors, transformers, distributed generators, loads, etc. The consequence is a set of perturbations that directly impact all the electronic or electrical connected equipment.

Moreover, the problems related to power quality increase with the high level of nonlinear electronic equipment connected to the grid and the high penetration of renewable energy such as wind turbines and photovoltaic systems interfaced as distributed generators. Therefore, the grid can be considered a high-complex system in which the regulation of voltage to meet the standards is of great concern. Maintaining the power quality to acceptable levels has become a challenge today since any current, or voltage distortion, is propagated to the entire network through the impedance of the lines and connected devices and equipment.

A poor-quality network can induce malfunctions to connected electrical or electronic devices. The following list shows some examples of electrical and electronic machines issues:

- Malfunction and torque distortion in electrical motors
- Overheating of transformers and motor
- Lifespan reduction of electrical and electronic machines
- Poor power factor leading to copper losses and bad efficiency
- Undesired disconnection (tripping) of contactors and electromechanical relays
- Undesired tripping of sensitive loads
- Undesired fuses blowing
- Interruption of industrial production and damage on computers
- Interference on electronic equipment
- Lightning flicker

A solution for achieving a high power quality consists in regulating the power factor to reduce the fundamental frequency currents circulating into the lines due to reactive power. Another

contribution is using active filters for reducing the harmonic pollution introduced by nonsinusoidal conditions due to linear loads. Also, the utilization of voltage stabilizers to mitigate voltage variations ensures operation around nominal values.

Monitoring the grid parameters using smart meters spread all over the network is necessary to keep power quality standards. This monitoring employs several well-known techniques based on Phase-Locked Loops (PLLs), Second Order Generalized Integrators (SOGIs) tuned with Frequency Locked Loops (SOGI-FLLs), or Adaptive Notch Filters (ANFs), among others. These techniques synchronize interconnected power inverters with the grid providing active and reactive powers with high-quality standards. These methods should obtain the grid parameters in the shortest possible time and with high accuracy for returning the network operating to nominal values under different conditions. However, all these methods work under disturbances like harmonics, voltage sags, wells, flicker, dc offset, abrupt frequency drifts and phase jumps.

These perturbations distort the estimated frequency, amplitude voltage, and phase, which degrades the operation point of the equipment that relies on these estimates, like power inverters, worsening the problem. Therefore, it is necessary to enhance the robustness of PLLs, SOGI-FLL or ANF against these disturbances. This research focused-on analyzing the problems that impact the behavior of the SOGI-FLL, developing novel strategies for mitigating the degradation in the monitoring of grid parameters, improving the operation of grid-connected inverters under nonsinusoidal conditions.

2.1.1. Power Quality

Several standards define power quality. The more relevant of those are IEC 61000 series, IEEE1159:2009, IEEE 1100:2005. According to the I.E.C. series, it is "The ability of a device, equipment or system to function satisfactorily in its electromagnetic environment without introducing intolerable electromagnetic disturbances to anything in that environment". Also, IEEE standards can refer to it as a "set of parameters defining the properties of the power supply as delivered to the user in normal operating conditions in terms of continuity of supply and characteristics of voltage (magnitude, frequency, waveform)". In this work, the IEEE 1100:2005 standard has been adopted to characterize power quality. Regarding this standard, factors that influence Power quality are:

1) Harmonics, sub-harmonics and inter-harmonics
2) Undesired DC components in AC systems (DC-Offset)
3) Voltages Sags and Swells
4) Over-voltages
5) Under-voltages

From those, the more relevant for this research were identified as Harmonics, sub-harmonics, DC-Offset, Voltage Sags and Swells, due to the aforementioned perturbations such as power outages, voltage drop, abrupt load changes, lightning and switching surges, and nonlinear steady-state load conditions.

2.1.2. Harmonics

The most common harmonics in power systems are those which are of an integer multiple of the fundamental frequency. In 1822 J.B.J. Fourier proposed in [5] that any function that is continuously repetitive on a time interval can be represented as the summation of a D.C. component, a fundamental sinusoid component and a series of higher-order sinusoids at frequencies which are multiples of the fundamental frequencies. These harmonics usually have a magnitude, which is much smaller than the magnitude of the fundamental and are shifted in phase from the fundamental. An example of a power system signal with harmonic components for the electrical grid can be seen in Fig. 1.

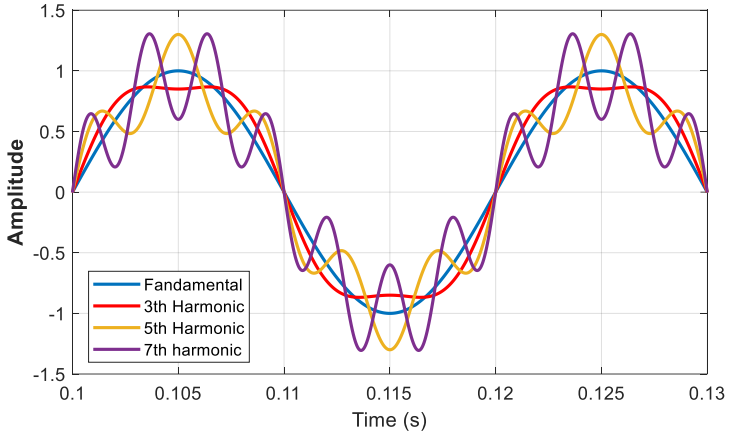

Fig. 1. Representative signals that can be found in power networks: Fundamental, Some Odd Harmonics and their Combined Waveform [6].

Fig. 1 illustrates some power system signals: a fundamental and 3rd, 5th, and 7th harmonic components Power systems signals consists primarily on measurements made over voltages and currents existing in the network. These voltages and current can be expressed by the following [8-13].

$$v(t) = V_0 + \frac{1}{\sqrt{2}}\sum_{n=1}^{\infty} v_{n(rms)}\cos(n\omega_1 t + \alpha_n) \tag{1}$$

$$i(t) = I_0 + \frac{1}{\sqrt{2}}\sum_{n=1}^{\infty} i_{n(rms)}\cos(n\omega_1 t + \beta_n) \tag{2}$$

where V_0 and I_0 are the DC components of the voltage and current, $v_{n(rms)}$ and $i_{n(rms)}$ are the root mean squared values of the n^{th}-voltage and current harmonics, and α_n and β_n are their respective phases. An important quantity which gives an overall measure of the "distortion" of the signal is referred to as the total harmonic distortion (THD) [14, 15]. Some last and final quantities that may be of interest when performing a study on power systems harmonics are the active and reactive powers, which are given as:

$$P_n = V_{n(rms)} I_{n(rms)} \cos(\alpha_n - \beta_n) \tag{3}$$

$$Q_n = V_{n(rms)} I_{n(rms)} \sin(\alpha_n - \beta_n) \tag{4}$$

2.1.3. Sub-harmonics

As described in previous section, sub-harmonics have a frequency which is a non-integer multiple of the fundamental frequency and their frequency is less than the fundamental frequency. A subharmonic frequency f_{subh} is described by:

$$0 < f_{subh} < f_1, \tag{5}$$

where f_1 is the fundamental frequency. Subharmonics and the fundamental component can be seen clearly in the frequency spectrum of a cycloconverter, illustrated in Fig. 2.

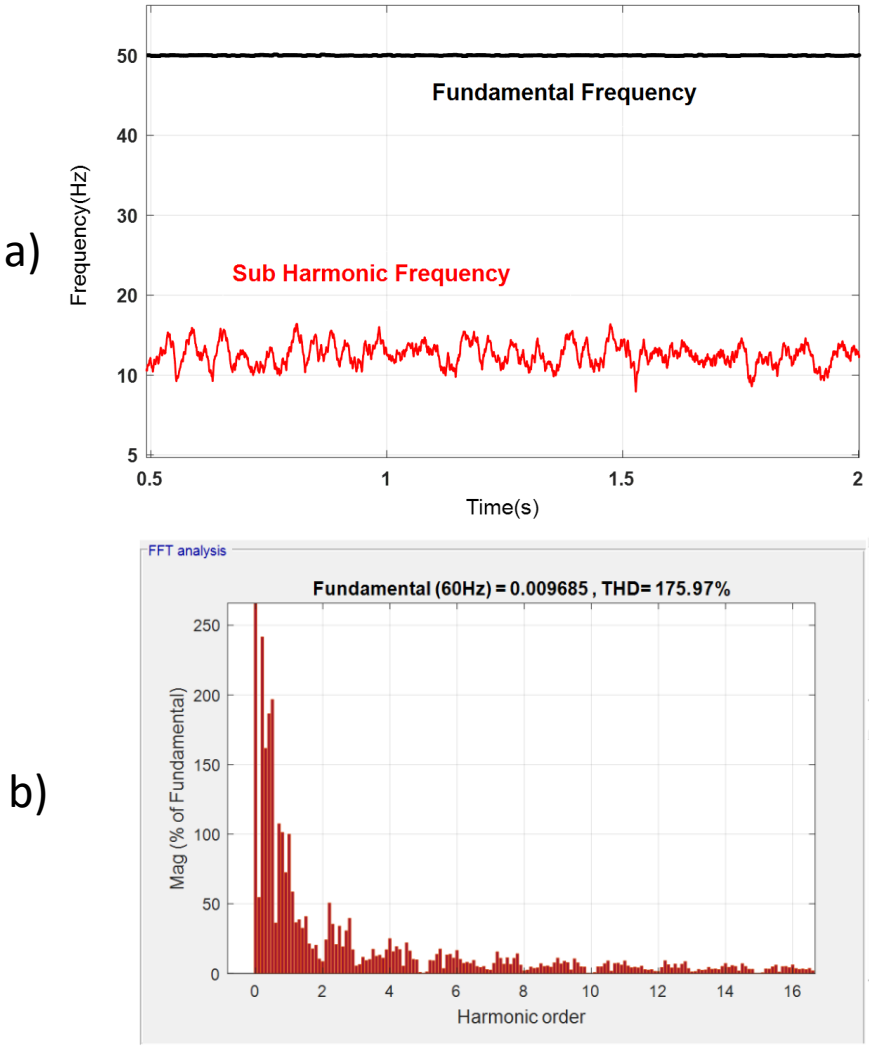

Fig. 2. Illustration of Subharmonic Frequencies in the Frequency Spectrum of a Typical Cycloconverter. a) frequency of nominal and sub harmonic, b) magnitude of harmonic order (%)

Subharmonics are a specific type of inter-harmonic. The sources of subharmonics can be cycloconverters, arc furnaces, geomagnetical currents [4-6,12,13].

2.1.4 DC Offset

DC-offset is a distortion phenomenon that appears in the electrical grid due to asymmetrical faults that generates a transient that decays to a steady state situation, see Fig. 3, DC-offset can also be induced by the injection of DC small current in the AC grid due to power inverters [16]. This DC current injection can saturate the distribution transformers, which can lead to waveform distortion, errors in the protective relays, losses, overheating, and reduced life expectancy in equipment.

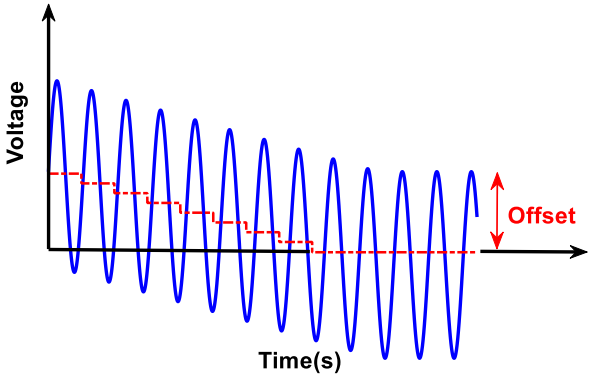

Fig. 3. Transient DC-offset.

2.1.5 Voltage Sags

Voltage sags, or dips, are defined by the IEEE 1159 as a short-time reduction in the grid voltage amplitude due to a fault in the line, which can be caused by a short circuit, overload, or starting of large motors, the Energizing higher-capacity power transformer, or the disconnection of a large reactive power source [17-19]. A voltage sag can have a duration that can range from of 0.5 $cycles$ to 1 $minute$ and can go from 0.9 per-unit (pu) to 0.1 pu in voltage magnitude. According to their duration, voltage sags are classified into three categories: instantaneous sags lasting from 0.5 $cycles$ to 30 $cycles$, momentary sags from 30 $cycles$ to 3 s, and temporary sags from 3 s to 1 $minute$. If the sag lasts more than 1 $minute$, it is classified.

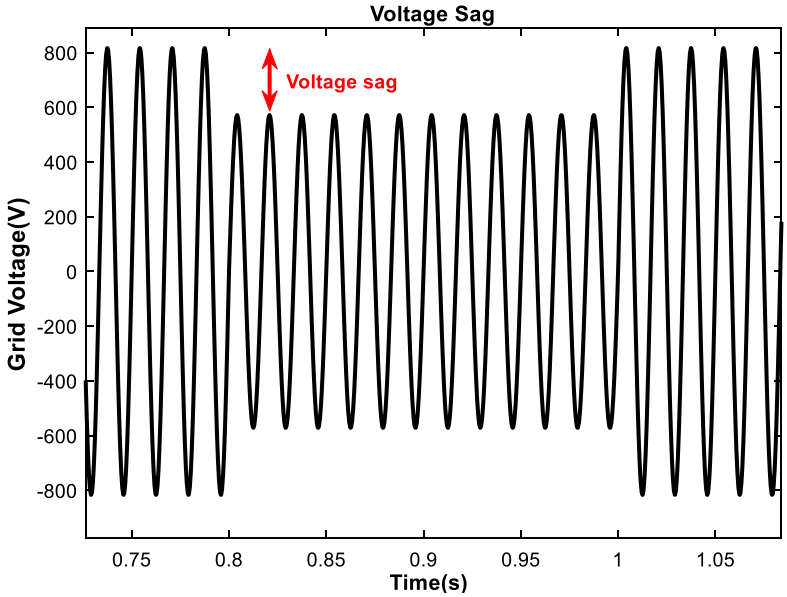

Fig. 4. Example of a voltage sag caused in the grid voltage by a fault.

Voltage sags produce peak currents, speed loos, peak torques in electrical motors, and problems in motor contactors during the sag and during the sag recovery. Also, the tripping of adjustable speed drives, problems in automation programmable logic controllers, and sensitive electronic equipment (Fig. 4).

2.1.6 Voltage swells

Voltage swells are defined are defined by the IEEE 1159 as a short-time increase in the grid voltage amplitude due to a single line-to ground fault, by the de-energization of huge loads or energization of a capacitor banks, among other causes. Voltage swells are also classified into the same three categories as for voltage sags. Voltage swells can be instantaneous, from 0.5 $cycles$ to 30 $cycles$ and from 1.1 pu to 1.8 pu; momentary, from 30 cycles to 3 s and from 1.1 pu to 1.4 pu; and temporary, from 3 s to 1 min and from 1.1 pu to 1.2 pu. The impact of strong voltage swells such as 1.8 pu in the SOGI-FLL estimated frequency is also high but with less magnitude than the case of 0.2 pu voltage sags [17, 18].

The appearance of voltage swells in the grid line can induce problems in electric controls and in the electric motor drives, particularly in common adjustable-speed drives, which can trip because of their built-in protective circuitry. Swells can induce stress in computers with delicate components, shortening its lifespan. A voltage swell is defined as an increase in the R.M.S voltage between 110 % to 180% of the amplitude voltage for durations from 0.5 $cycles$ to 1 min. They appear on the switching-off of a large load; energizing a capacitor bank; or voltage increase of the unfaulted phases during a single line-to ground fault. Fig. 5 shows a waveform of voltage swell [19].

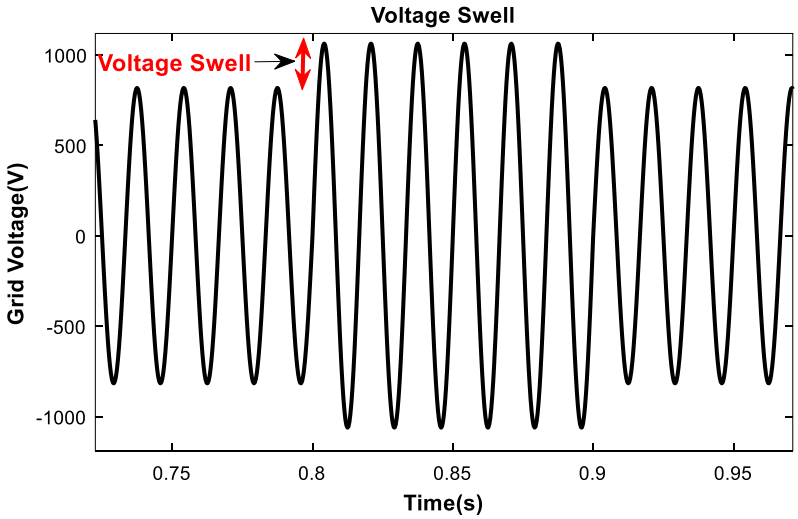

Fig. 5. Example of a voltage swell caused in the grid voltage by a fault.

2.2. Grid Synchronization techniques

Synchronization techniques like Phase-locked loop (PLL) had been widely used in radio, telecommunications and computers. They mainly have been used to demodulate signals, provide stable frequency clock signals for electronics and microprocessors, or to generate clock and frequency multiples of the input frequency.

For the electrical system there are several methods reported in literature for the synchronization of single-phase and three-phase systems. These methods can be grouped into frequency and time domain methods. Frequency domain techniques are based in Fast Fourier Transforms (FFT) and Discrete Time Fourier Transforms and its variants that are complicated to implement due to its high computational burden [20,21]. As time domain methods it can be found Zero-crossing detection methods (ZC) [22], Kalman filters (KF) and Extended Kalman Filters (EKF) [23], Least-Square (LS) and Recursive Least-Square (RLS) [24,25], adaptive notch filters (ANF) PLLs [26,27], and Frequency-Locked Loop (FLL) based methods [28,29].

ZC methods use the zero crossing point of the grid voltage for synchronizing, but are sensitive to grid distortion and faults. KF and EKF is a signal processing technique that offer a stable and accurate estimation under harmonic and distorted conditions. LS and RLS apply the Least-Square estimation technique to fit the grid voltages into a series of sinus and cosinus functions or the phases to a line with a slope that is the frequency of the grid, but the accuracy strongly depends on the frequency level of the grid, which deteriorates when the grid is distorted. ANF are second-order notch filters with an adaptive mechanism used to cancel unwanted components of the grid voltage or estimate the grid voltage parameters. Among all the reported methods, PLL based methods are widely used due to their inherent simplicity and robustness. There are several methods in literature, such as the synchronous reference frame PLL (SRF-PLL) [30, 31], the inverse-park PLL (IP-PLL) [32], the transport-delay PLL (TD-PLL) [33, 34], the quadrature PLL (QPLL) [35, 36], the enhanced PLL (EPLL) [37-46], or the SOGI-PLL. This last one, based on the SOGI filter that generates quadrature components of the input signal to be linked with the PLL [47-55]. However, they have associated in common drawbacks like sensitivity to grid voltage distortions and time-response dependency on the parameters of their proportional-integral (PI) inner control blocks. The FLL methods are based on a simple gradient descent estimator [56], requiring only three math terms: a multiplication, a gain, and an integrator. The FLL is used with the SOGI filter to tune the SOGI with the grid frequency in different applications due to its robustness, behavior and simplicity of implementation [57-60].

In [60], the SOGI-FLL problems with dc-offset voltage were solved by inserting a third integrator using an additional inner loop. This method leads to a simple inner algorithm that enhances the performance of the system. In [61] the nonlinear behavior of the FLL was compensated using a fuzzy logic controller to improve the SOGI-FLL performance at the event of grid-faults. In [62] a model of the SOGI-FLL was derived for the adaptive tuning of a resonant regulator for a single-

phase inverter. In [63-65], an additional SOGI was added as a pre-filter to the SOGI-FLL leading to a double-SOGI structure (DSOGI-FLL). The DSOGI-FLL provide robustness against a vast source of distortion in the grid, like harmonics, subharmonics, and dc-offset voltage. In these last two works, a deep analysis about the SOGI trade-off between settling-time response and harmonic rejection was provided for design considerations and system tuning. In [66, 67], a dynamic phasor modelling (DPM) technique was introduced for a better analysis of stability margins of single-phase PLLs. In this work, the SOGI-FLL was transformed to the rotating reference frame, reformulated as a PLL using a PI controller, and compared with an Inverse Park-PLL (IP-PLL) and EPLL. Detailed dynamics and stability boundary limits were provided for these systems, concluding that the EPLL was adequate for networks with frequent phase-jump faults, while the SOGI-FLL was for networks with voltage sags. However, to this regard, it should be considered that the SOGI-FLL structure is simpler than the EPLL and that the EPLL requires of sine/cosine math functions, typically implemented with lookup tables, which increase the computation load of the system.

The power quality problems of the grid networks impacts the performance of all these different grid synchronization techniques in a different manner, depending on their particular structure and gain-parameters, distorting the estimated frequencies, amplitudes and phases. An accurate performance comparison between all these techniques it is difficult to achieve because some of them are simple structures and others more complex and they have trade-off relationships that are related to the complexity of the implementation. When a given method provides a noticeable rejection to harmonic distortion, it can present a bad response to DC-offset, have a slow response to frequency changes, or being highly perturbed by voltage sags. For this reason, this work presents the behavior of some of these structures, like the SFR-PLL, EPLL, SOGI-PLL, and SOGI-FLL, to the most frequent distortions in the grid: dc-offset, harmonics, subharmonics, voltage sags, and voltage swells. For the case of the SFR-PLL in front of voltage sags, it is shown its performance when they are affected by an asymmetrical fault, like a voltage sag in only one of the phases. This scenario has been selected because is the one that best shows the distortion effects on the SFR-PLL.

Continuous and discrete models of these techniques have been built with the objective of showing their affectation by the grid distortions mentioned above. Many works have been presented in literature to study how to mitigate the impact of these distortions, especially in the case of harmonics, subharmonics and DC-offset. However, there is almost nothing presented regarding mitigating the impact of voltage sags or swells to our knowledge. Particularly, the case of voltage sags is the most important, because it usually have a profound impact in the frequency estimate achieved by a given method, because they by definition can arrive to $0.1\ pu$, which is a significant perturbation to face.

2.2.1 Phase Locked Loop (PLL)

The PLL concept was proposed first at 1923 by Appelton as a synchronization for triode oscillators [68], and used by Belleslice in 1932 for synchronization of radio signals [69], but it was not since 1970s that it was widely applied due to its difficulty in the implementation [70].
The PLL structure can be seen in Fig. 6 and consists on a feedback loop formed by a phase detector (PD), a loop filter (LF) and a voltage controlled oscillator (VCO).

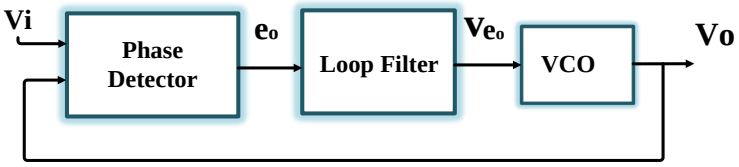

Fig. 6. Block diagram of a PLL.

The phase detector (PD) consists in a product between the input and the output signals, i.e. by $v_e = v_i \cdot v_o$, that is filtered by the loop filter (LF), which is usually a low-pass-filter (LPF). The LF provides its DC-component of the PD product, named as v_{e0}. This component drives the VCO that generates a sinusoidal output frequency that is proportional to the voltage level of v_{e0}.

Assuming that the input signal (6) and the VCO generated signal is also sinusoidal (7):

$$v_i(t) = \sin[\omega_i t + \theta_i], \tag{6}$$

$$v_o(t) = \cos(\omega_o t + \theta_o), \tag{7}$$

where $v_i(t)$ is the input signal, $v_o(t)$ is the VCO signal, ω_i and ω_o are the input and ouput frequencies, respectively, and θ_i and θ_o are the input and output phase angles, respectively.

The VCO generates a sinusoidal signal with an output frequency that is proportional to LPF output voltage:

$$\omega_o = \omega_c + k_o v_{e0} \tag{8}$$

where v_{e0} is the output of the LPF, k_o is the VCO gain, and ω_c is a minimum frequency value in which the VCO can oscillate. The PD is usually carried out by a product operation between the input and output signals, i.e.:

$$v_e(t) = k_{PD} \cdot v_i(t) \cdot v_o(t) = k_{PD} \cdot \sin(\omega_i t + \theta_i) \cdot \cos(\omega_o t + \theta_o) \tag{9}$$

where k_{PD} represents the gain of the PD. The PD applying a trigonometric identity can be expressed as:

$$v_e(t) = \frac{k_{PD}}{2}[sin(\omega_i t + \omega_o t + \theta_i + \theta_o) + sin(\omega_i t - \omega_o t + \theta_i - \theta_o)] \tag{10}$$

In (10) there are two frequency components: one corresponding $(\omega_i + \omega_o)t + \theta_i + \theta_o$ and the other to $(\omega_i - \omega_o)t + \theta_i - \theta_o$. The LPF filters the high frequency component and leaves the low frequency unaffected. Therefore, at the output of the LPF there is:

$$v_{e_o}(t) = \frac{k_{PD}}{2} sin(\omega_i t - \omega_o t + \theta_i - \theta_o), \tag{11}$$

which, assuming that $\omega_o \cong \omega_i$, and that $\theta_i - \theta_o$ is small, could be approximated to:

$$v_{e_o}(t) = \frac{k_{PD}}{2}(\theta_i - \theta_o) = k_d \cdot \theta_e \tag{12}$$

being $k_d = k_{PD}/2$ Then, a closed loop between the input and output phase signals can be distinguished in these equations, which is depicted in Fig. 7.

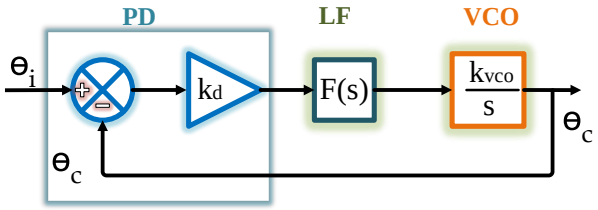

Fig. 7. Basic PLL Block Diagram.

2.2.2 Synchronous Reference Frame-PLL (SRF PLL)

Fig. 8 shows the block diagram of a SRF-PLL in which V_{abc} are the 3-phase voltage signals. The first block represents the Clark and Park Transformations, which translates a 3-phase voltages from the abc-natural reference frame to *αβ*-stationary reference frame and then to *dq*-rotating frame. A Proportional Integrator (PI) controller is used as loop filter [71,72].

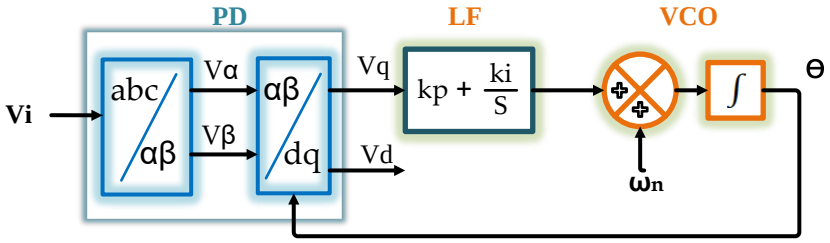

Fig. 8. SRF PLL block diagram.

The Clark transformation from *abc* to *αβ*-coordinates is:

$$\begin{bmatrix} V_\alpha \\ V_\beta \end{bmatrix} = \frac{2}{3}\begin{bmatrix} 1 & -\frac{1}{2} & -\frac{1}{2} \\ 0 & -\frac{\sqrt{3}}{2} & -\frac{\sqrt{3}}{2} \end{bmatrix}\begin{bmatrix} V_a \\ V_b \\ V_c \end{bmatrix} \tag{13}$$

And, the Park transformation, *dq*-coordinates is defined as:

$$\begin{bmatrix} V_d \\ V_q \end{bmatrix} = \begin{bmatrix} \cos(\theta_o) & \sin(\theta_o) \\ -\sin(\theta_o) & \cos(\theta_o) \end{bmatrix}\begin{bmatrix} V_\alpha \\ V_\beta \end{bmatrix} \tag{14}$$

The transformation from *abc* to *dq*-coordinates acts in the PLL as a phase detector. The outputs of the PD detector can be expressed at steady state [72-74].

$$V_q = V \cdot \sin(\theta_i - \theta_o) \tag{15}$$

$$V_d = V \cdot \cos(\theta_i - \theta_o) \tag{16}$$

where V is the estimated amplitude voltage of the grid. Assuming that the grid is balanced and that the estimated frequency is close to the grid frequency, i.e. $\omega_o \cong \omega_i$ and $\theta_o \approx \theta_i$, can be simplified to:

$$V_d \approx V \tag{17}$$

$$V_q \approx V \cdot (\theta_i - \theta_o) = V \cdot \theta_e \tag{18}$$

Therefore, V_d provides an estimate of the amplitude voltage of the grid and V_q provides the phase error of the PLL, which is used to provide a grid frequency using a PI control. This frequency is converter into phase by using an integrator, see Fig. 8 and is feedback to the PD to perform the Park transformation [75]. The SFR-PLL can be seen as a closed loop in phase, according the following Fig. 9.

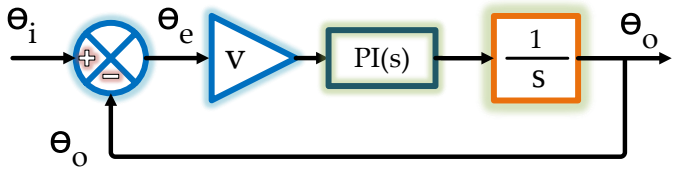

Fig. 9. Phase closed loop phase scheme of the SFR-PLL.

The close transfer function of the SFR-PLL (small-signal) can be defined as:

$$\frac{\theta(s)}{\theta_i(s)} = \frac{V \cdot PI(s)}{s + V \cdot PI(s)} \tag{19}$$

Which can be identified as a second order normalized system:

$$\frac{\theta(s)}{\theta_i(s)} = \frac{2\xi\omega_n \cdot s + \omega_n^2}{s^2 + 2\xi\omega_n \cdot s + \omega_n^2} \tag{20}$$

In which ξ and ω_n are the damping factor and the undamped natural frequency, respectively. Therefore, the response of the system can be determined by adjusting the parameters of the SFR-PLL by selecting the appropriated ξ and ω_n.

Figs. 10 to 15 show the performance of the SFR-PLL under different grid distorting conditions achieved by simulations using Matlab/Simulink for $k_p = 0.36$ and $k_i = 22$. The SFR-PLL has been perturbed by a step change frequency (Fig. 10), DC-offset voltage (Fig. 11), harmonics (Fig. 12), subharmonics (Fig. 13), and voltage sag and voltage swell in one of the phases (Figs. 14 and 15, respectively).

In Fig. 10 the response to a step change frequency from $50Hz$ to $55Hz$ at $0.2s$ is shown. The SFR-PLL is able to follow the perturbation in the estimated frequency, but note that the amplitude is also perturbed, transitorily, returning to the value that should have at steady state. This effect is common in all the monitoring methods, since there is a coupling between the amplitude and frequency estimates that do not appear in the small-signal model, due to the simplifications made to arrive to the model. This also happens when the perturbations are not in fact small and they are huge, like in the case of deep voltage sags.

In Fig. 11 a DC-offset voltage of $10V$ is applied at $0.2s$ to one of the phases of the grid. Note how this perturbation makes the estimated amplitude voltage and frequency oscillate around the

nominal values. This shows how the SFR-PLL is sensitive unsymmetrical perturbations because of the Clark's and Park's transformations.

In Fig. 12 a 5th harmonic with a 10% amplitude regarding nominal is introduced in the grid at $0.2s$. In Fig. 13 a $1.6Hz$ subharmonic with a 10% amplitude is introduced in the grid. Note how the SFR-PLL's amplitude and frequency estimates are perturbed in both cases.

In Fig. 14 a 60% deep voltage sag, that goes form $1\ pu$ to $0.4pu$, is introduced in one of the phases of the grid. Note how the SFR-PLL has a bad and oscillating response in the amplitude estimate and an oscillating response is also achieved in the frequency. Fig. 15 shows a similar response in face of a voltage swell in one of the phases going from $1pu$ to $1.6\ pu$.

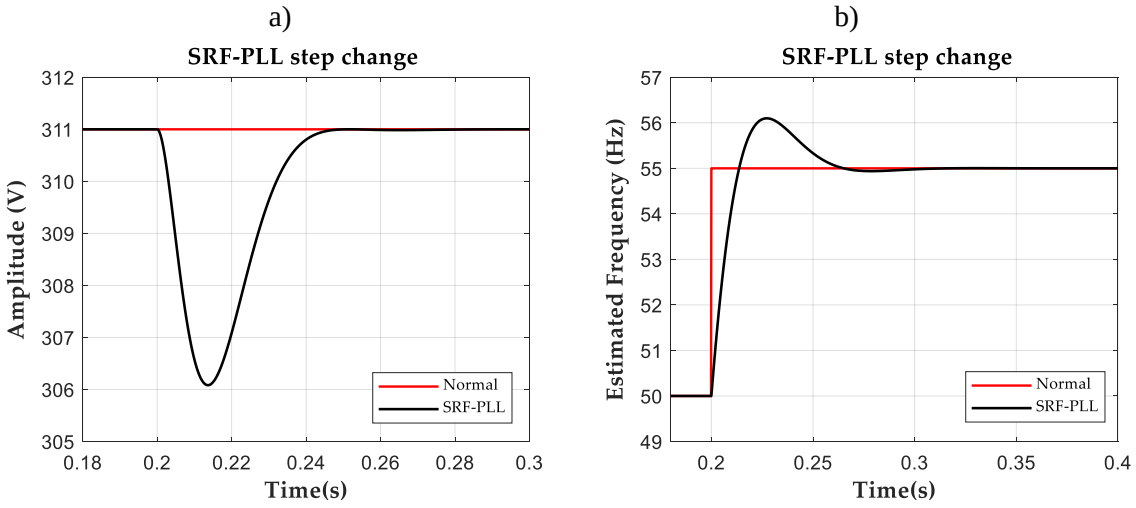

Fig. 10. Response of the SFR-PLL to a frequency step change in the grid $50Hz$ to $55Hz$ at $t = 0.2s$: a) Estimate amplitude voltage, b) Estimate frequency.

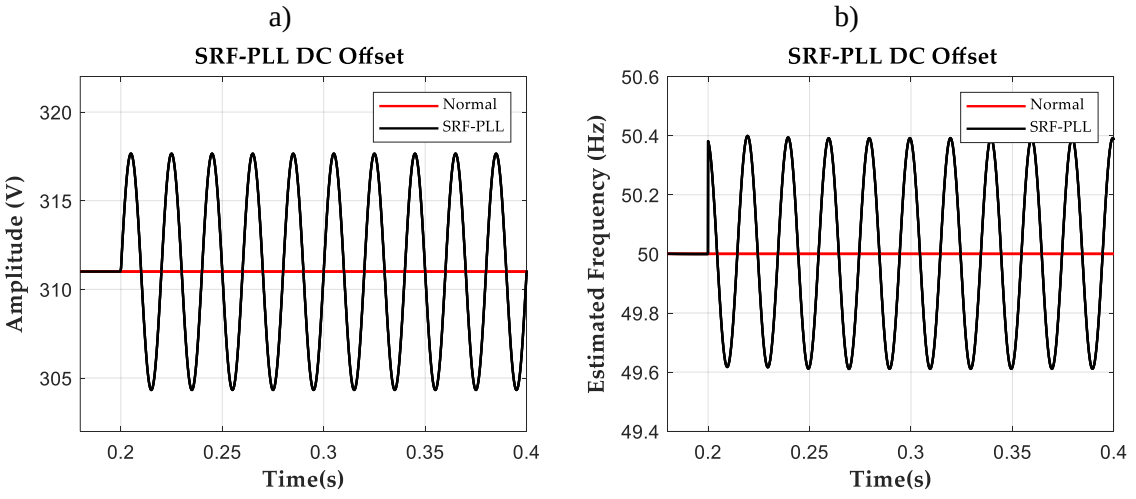

Fig. 11. Response of the SFR-PLL to the appearance of $10V$ DC-offset in the grid voltage at $t = 0.2s$: a) Estimate amplitude voltage, b) Estimate frequency.

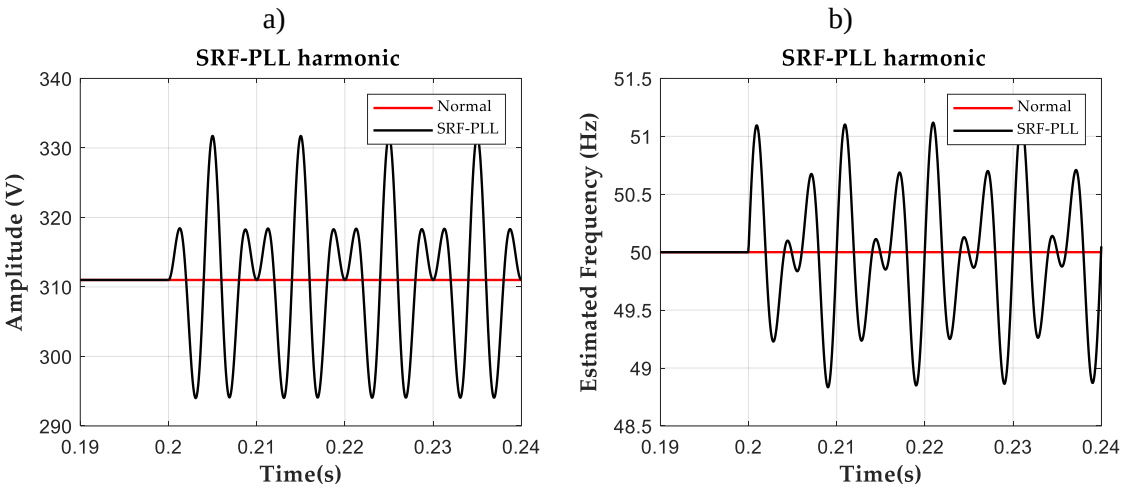

Fig. 12. Response of the SFR-PLL to a 5th harmonic with 10% amplitude appearing at at $t = 0.2s$: a) Estimate amplitude voltage, b) Estimate frequency.

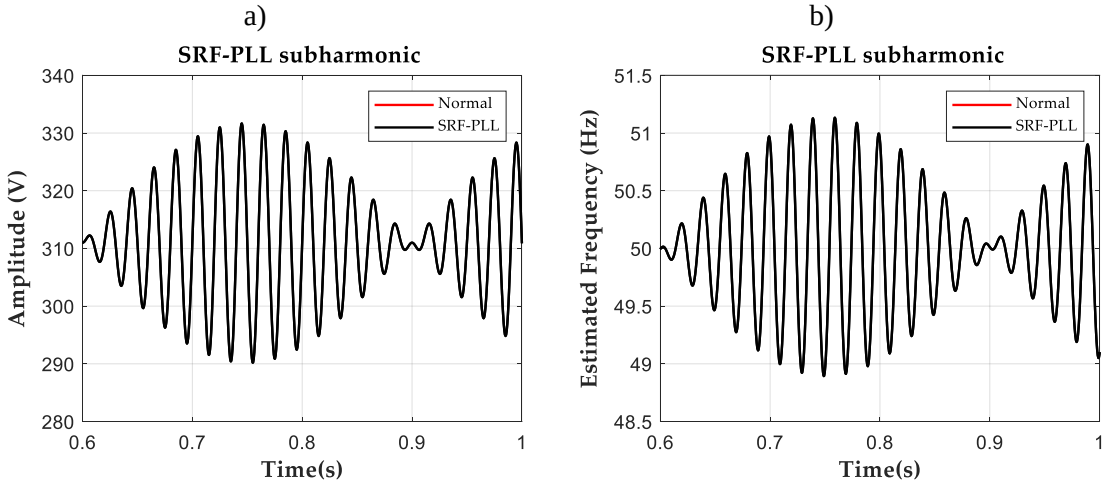

Fig. 13. Response of the SFR-PLL to a $1.6Hz$ subharmonic with 10% amplitude: a) Estimate amplitude, b) Estimate frequency.

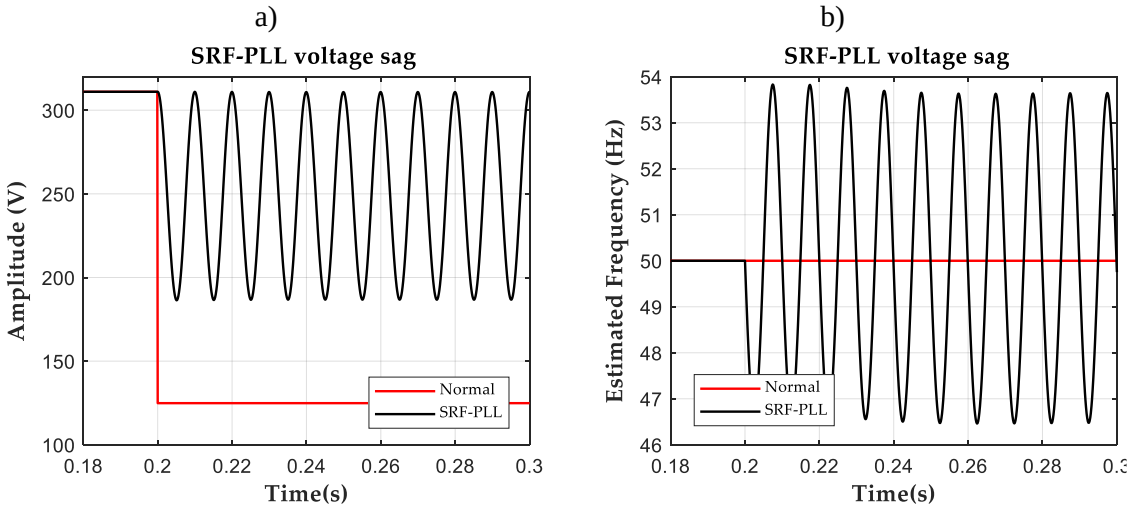

Fig. 14. Response the SFR-PLL to a voltage sag at $t = 0.2s$ going from $1pu$ to $0.4pu$: a) Estimate amplitude, b) Estimate frequency.

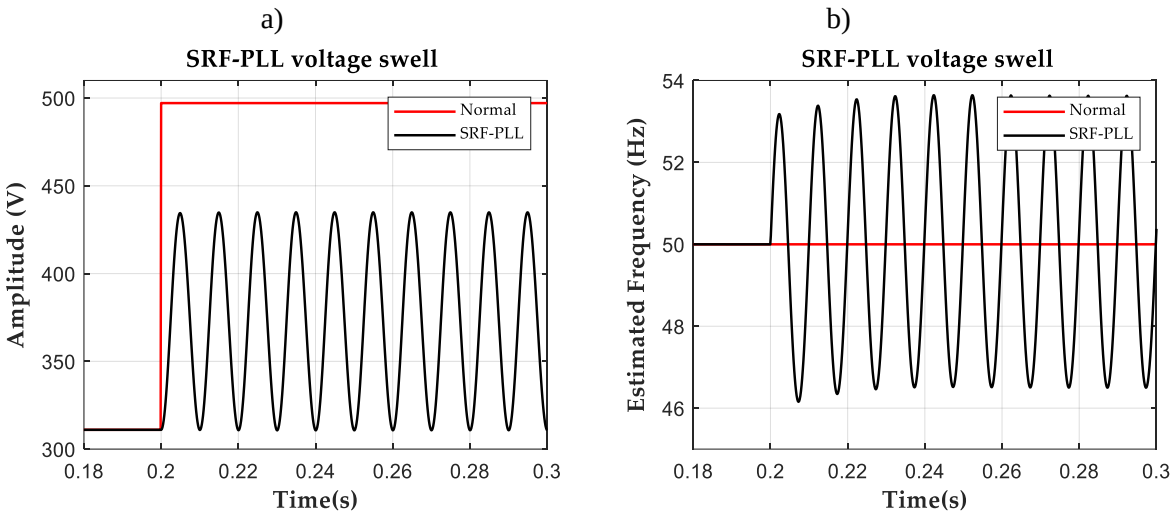

Fig. 15. Response of the SFR-PLL to voltage swell at $t = 0.2s$ going from $1pu$ to $1.6pu$: a) Estimate amplitude, b) Estimate frequency.

2.2.3 Transport Delay-based PLLs

The transport delay PLL is a single-phase PLL in which the input signal is delayed by $T/4$ (T is the period of the input signal) for providing the 90° delayed signal needed for the β-component needed for the Park transformation. Fig. 16 shows the block diagram of a TD-PLL which corresponds to that of a SFR-PLL but without using the Clak transformation.

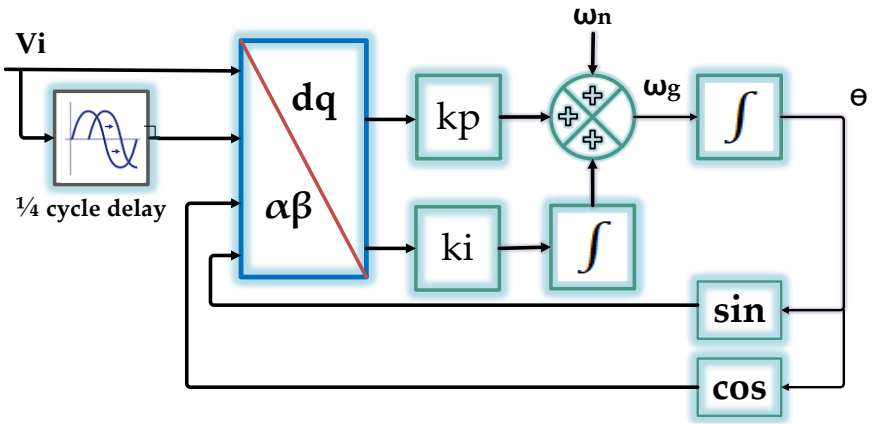

Fig. 16. Standard TD-PLL.

The TD-PLL has been affected by the same type of perturbations than the performed for the SFR-PLL. The parameters in this case are $k_p = 0.36$ and $k_i = 22$. The TD-PLL has been perturbed by a step change frequency (Fig. 17), DC-offset voltage (Fig. 18), harmonics (Fig. 19), subharmonics (Fig. 20), and voltage sag and voltage swell (Figs. 21 and 22 respectively).

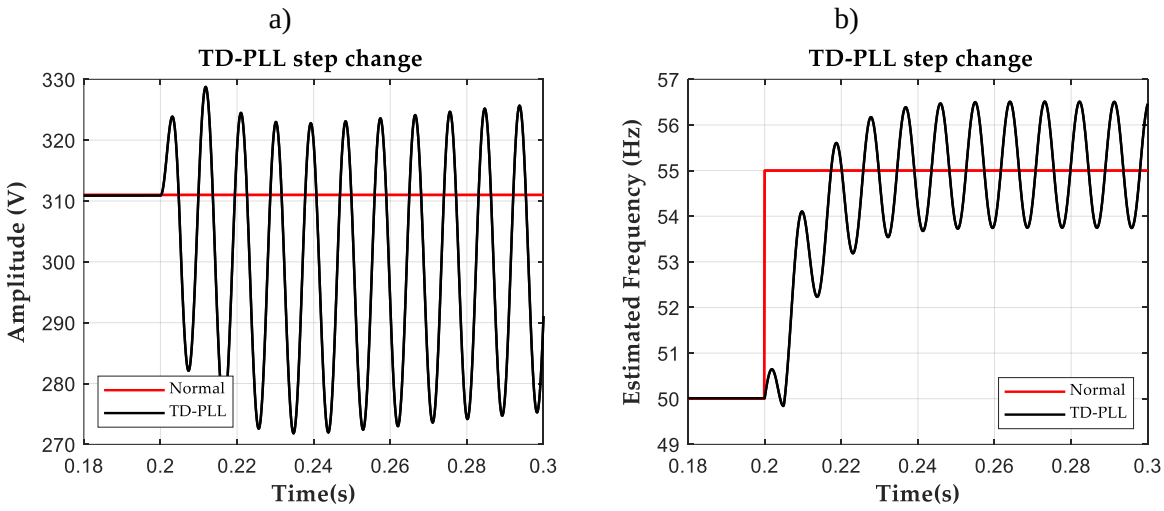

Fig. 17. Response of the TD-PLL to a frequency step change in the grid $50Hz$ to $55Hz$ at $t = 0.2s$: a) Estimate amplitude voltage, b) Estimate frequency.

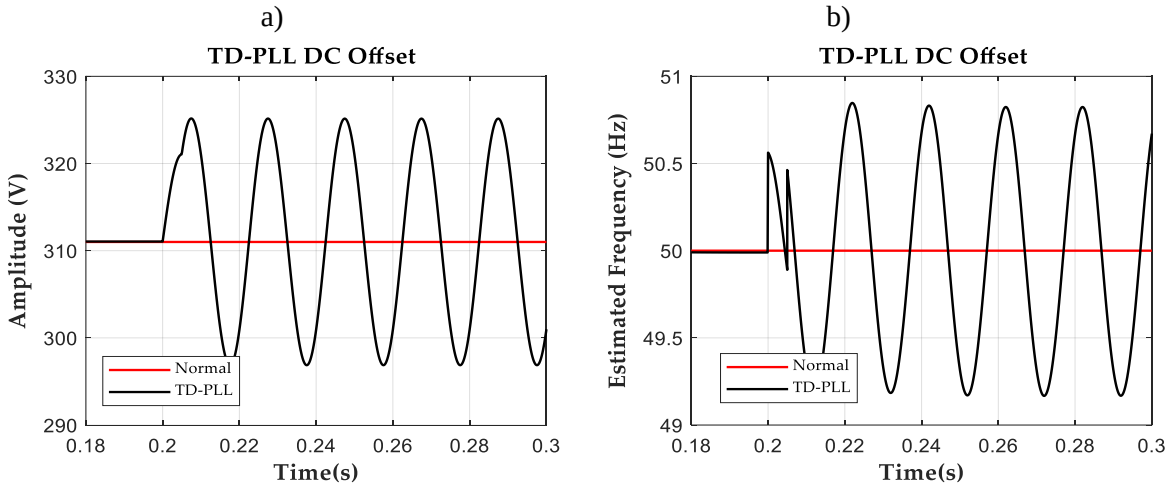

Fig. 18. Response of the TD-PLL to the appearance of $10V$ DC-offset in the grid voltage at $t = 0.2s$: a) Estimate amplitude voltage, b) Estimate frequency.

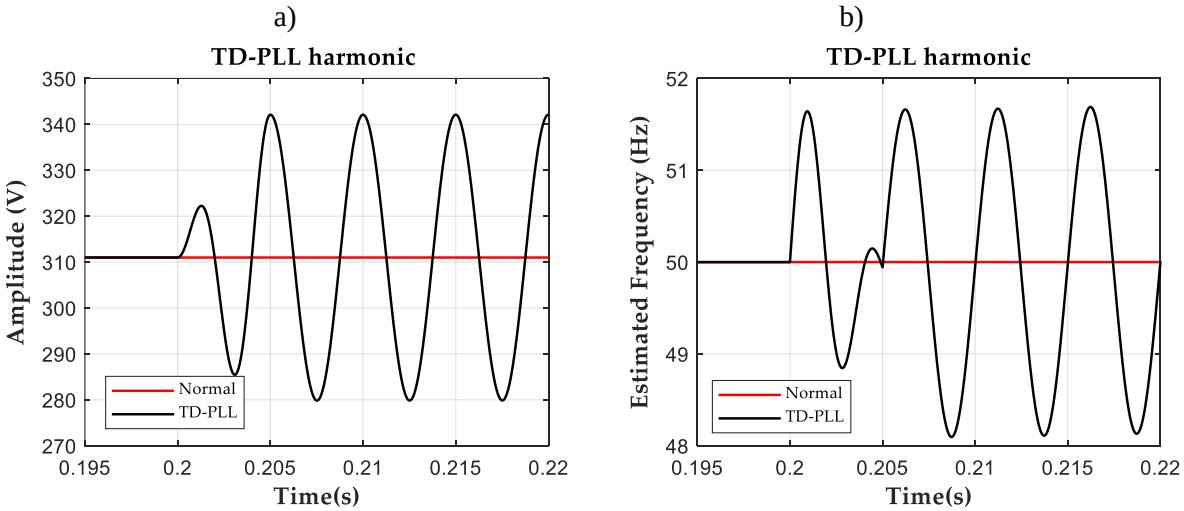

Fig. 19. Response of the TD-PLL to a 5th harmonic with 10% amplitude appearing at at $t = 0.2s$: a) Estimate amplitude voltage, b) Estimate frequency.

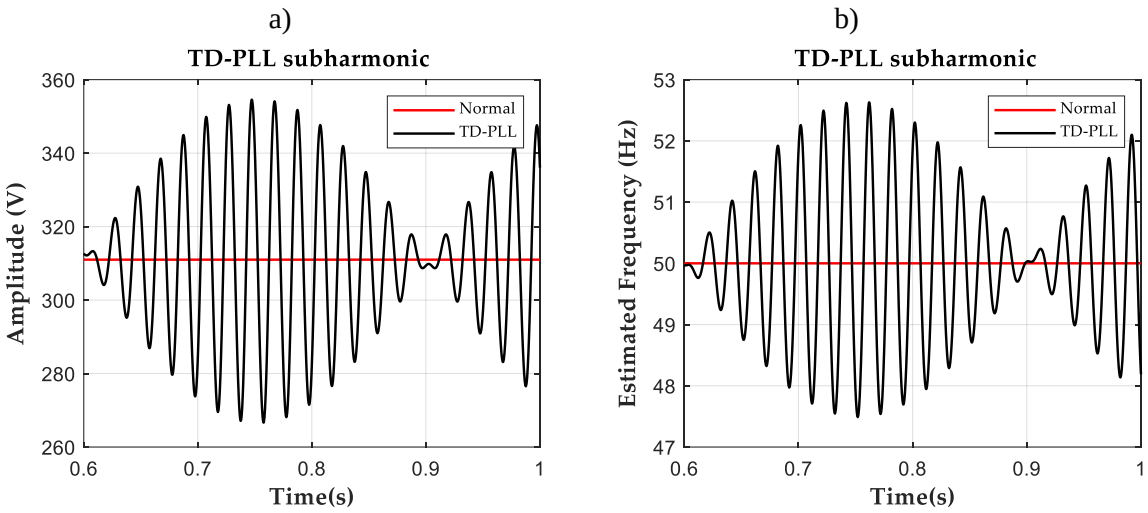

Fig. 20. Response of the TD-PLL to a 1.6Hz subharmonic with 10% amplitude: a) Estimate amplitude, b) Estimate frequency.

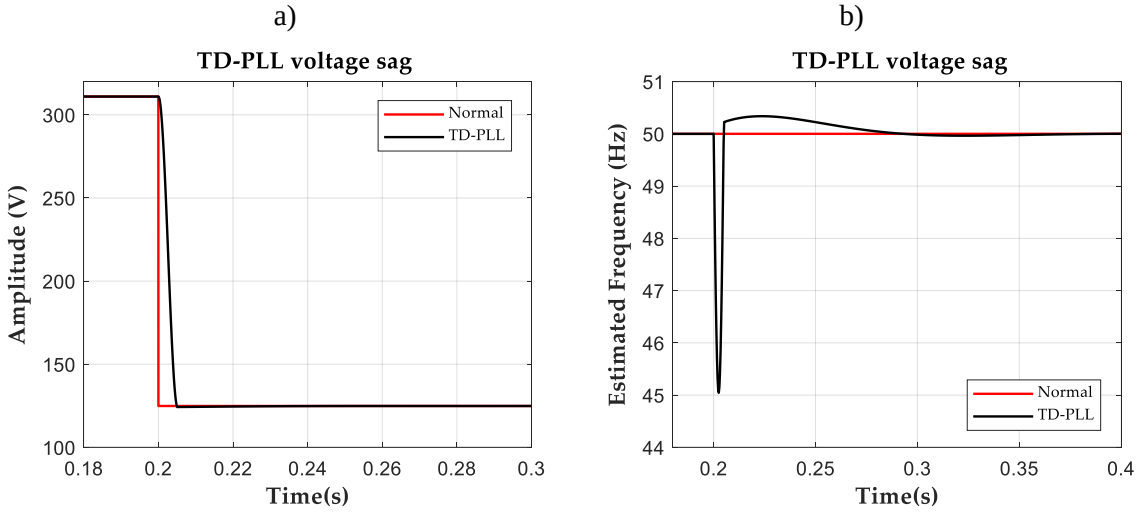

Fig. 21 . Response the TD-PLL to a voltage sag at $t = 0.2s$ going from $1pu$ to $0.4pu$: a) Estimate amplitude, b) Estimate frequency.

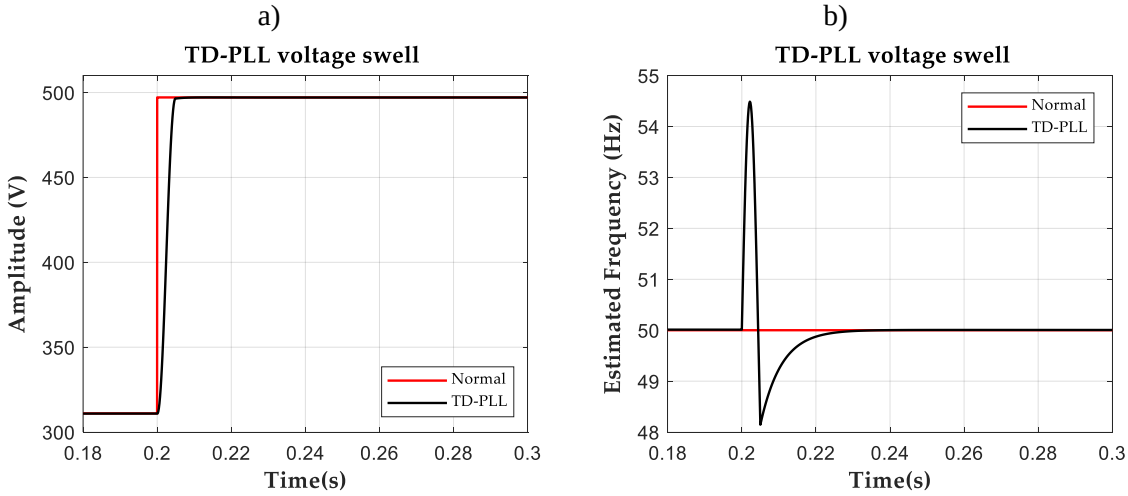

Fig. 22 . Response of the TD-PLL to voltage swell at $t = 0.2s$ going from $1pu$ to $1.6pu$: a) Estimate amplitude, b) Estimate frequency.

In the case of Fig. 17 notice that the transient to a frequency step change in the input signal produces an oscillatory response in both amplitude and frequency estimates. This response is due to the own nature of the transport delay that uses a fixed time to achieve the $T/4$ delay. In this case the delay is set to $T = 1/50 = 0.02ms$. Therefore, when the frequency changes to $55Hz$, the delay still is fixed to $0.02ms$, causing the generated β-component not to be accurately at 90º from the α-component, which induces the oscillation in the estimates. This is one of the drawbacks of this technique, which has been dealt and minimized in literature [34]. Fig. 23 shows how these oscillations disappear if, at the instant that the step change is made, the delay is updated to is correct value $T = 1/55$.

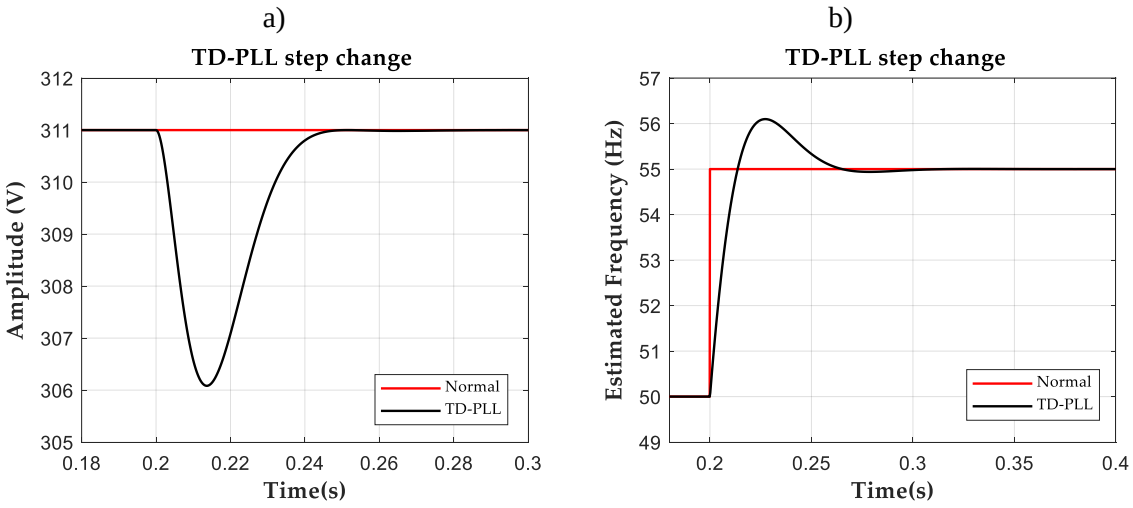

Fig. 23. Response of the TD-PLL to a frequency step change in the grid $50Hz$ to $55Hz$ at $t = 0.2s$ and modifying the transport delay value: a) Estimate amplitude voltage, b) Estimate frequency.

2.2.4 EPLL

The enhanced phase-locked loop (EPLL) [38-45] is a single-phase frequency-adaptive nonlinear synchronization approach, which uses an amplitude voltage estimation loop with the structure of a standard PLL. The block diagram of EPLL is shown in Fig. 24. Its major improvement over the conventional PLL lies in the PD mechanism that uses an amplitude voltage estimation loop as novelty. The EPLL has three internal independent parameters: in which V_i is the single-phase input signal, V θ, and ω are estimates of the amplitude, phase angle, and angular frequency of this signal, respectively, and k_p, k_i, and k_v are the control gains. The parameter k_v determines the convergence speed of the amplitude estimate. The parameters k_p and k_i are in charge of the PLL part, determining the dynamics of the estimate frequency and phase.

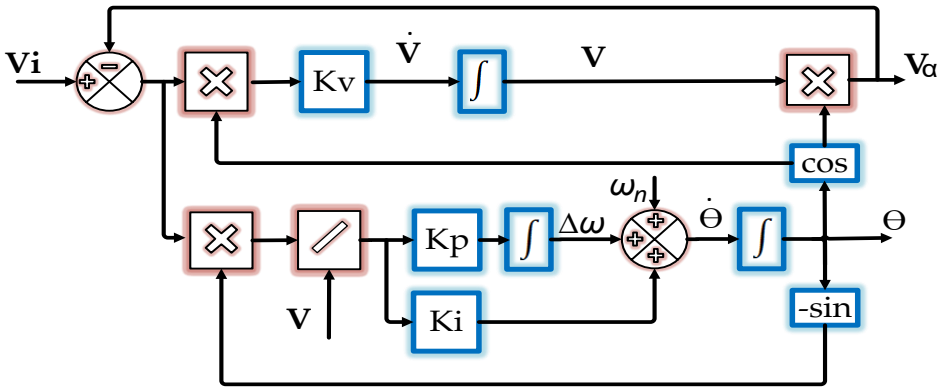

Fig. 24. Block diagram of single-phase EPLL.

The EPLL phase detection is achieved using an Adaptive Filter (AF) and a sinusoidal multiplier, as it is shown in Fig. 24. This PD is what makes different to an EPLL from a PLL and improves the performance [45, 47]. The adaptive filter estimates the amplitude voltage of the grid using a sinusoidal signal generated with the PLL estimated phase. According to Fig. 24, the estimated grid voltage amplitude V can be expressed as:

$$\dot{V} = k_v \cdot e \cdot \cos(\theta) \tag{21}$$

in which:

$$e = (V_i - V) \tag{22}$$

where V_i it is the amplitude voltage of the grid and V is the estimate. Assuming that the PLL is synchronized with the input frequency, i.e. $\theta \cong \theta_i$, the dynamics of the amplitude voltage estimate correspond to a first-order system that can be described by (23),

$$\frac{V(s)}{V_i(s)} = \frac{1}{\tau s + 1} \tag{23}$$

where $\tau = \frac{2}{\pi}$ [40]. The EPLL has been affected by the same type of perturbations than the performed for the SFR-PLL. The parameters in this case are $k_p = 0.7$, $k_i = 22$, and $k_v = 1.4$. The EPLL has been perturbed by a step change frequency (Fig. 25), DC-offset voltage (Fig. 26), harmonics (Fig. 27), subharmonics (Fig. 28), and voltage sag and voltage swell (Figs. 29 and 30, respectively). Note that the harmonic response of the EPLL is better than in the previous cases,

having a ripple noise distortion over the frequency response that is about 1.1 Hz, while for the SFR-PLL is of 2.2Hz and for the TD-PLL is of 3.5Hz. However, the EPLL has a worse response to voltage sag and swell than the rest of the approaches.

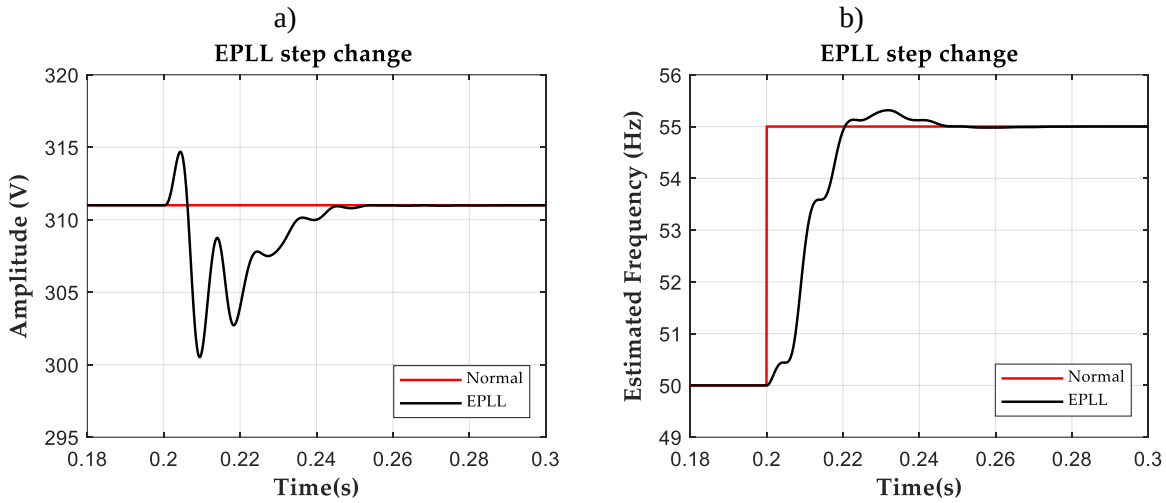

Fig. 25. Response of the EPLL to a frequency step change in the grid 50Hz to 55Hz at $t = 0.2s$: a) Estimate amplitude voltage, b) Estimate frequency.

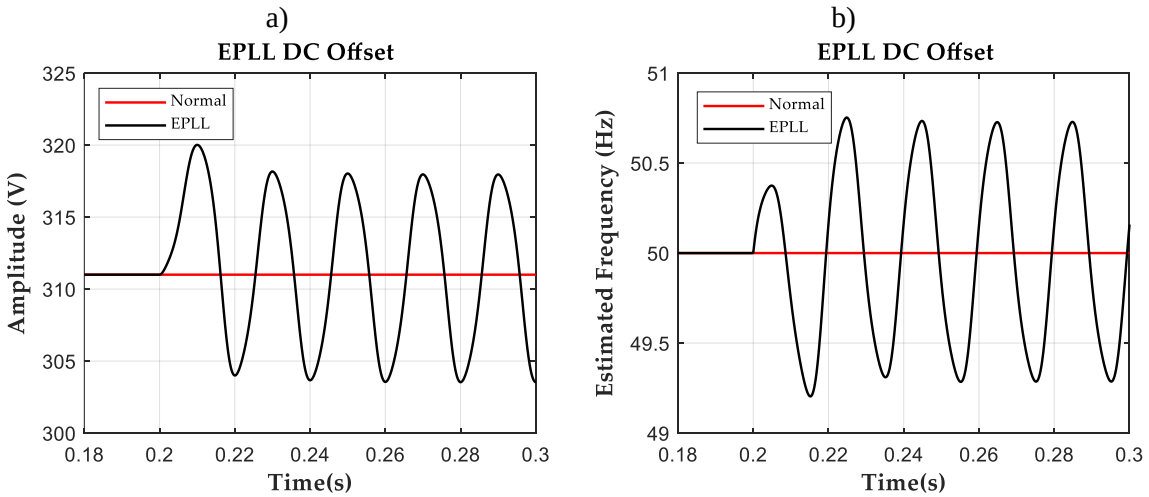

Fig. 26. Response of the EPLL to the appearance of 10V DC-offset in the grid voltage at $t = 0.2s$: a) Estimate amplitude voltage, b) Estimate frequency.

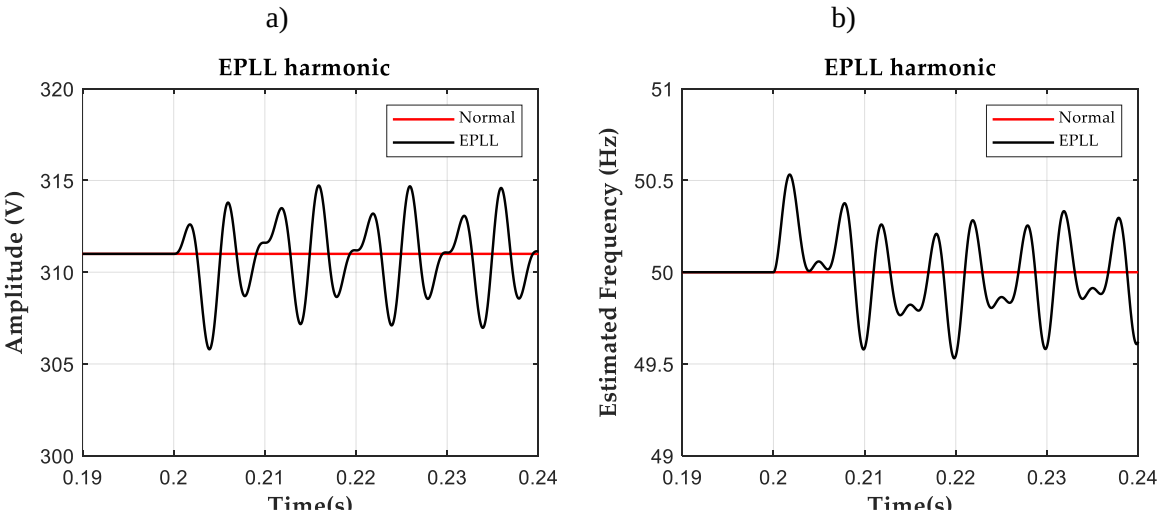

Fig. 27. Response of the EPLL to a 5th harmonic with 10% amplitude appearing at at $t = 0.2s$: a) Estimate amplitude voltage, b) Estimate frequency.

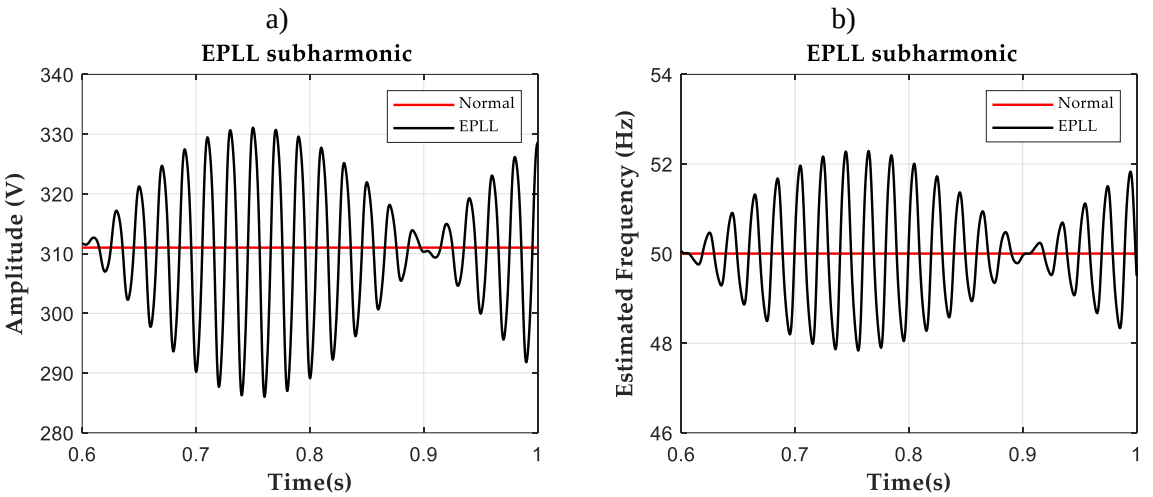

Fig. 28. Response of the EPLL to a $1.6Hz$ subharmonic with 10% amplitude: a) Estimate amplitude, b) Estimate frequency.

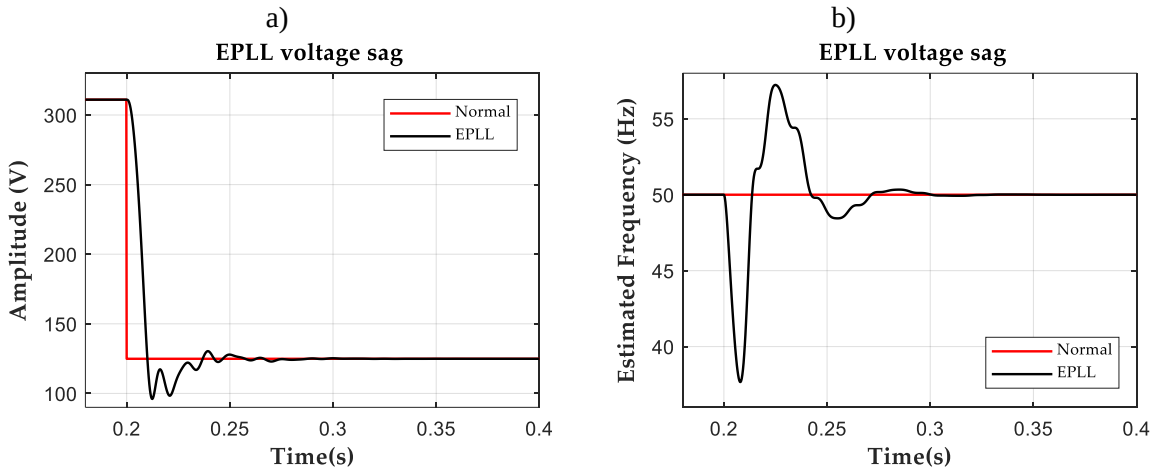

Fig. 29. Response the EPLL to a voltage sag at $t = 0.2s$ going from $1pu$ to $0.4pu$: a) Estimate amplitude, b) Estimate frequency.

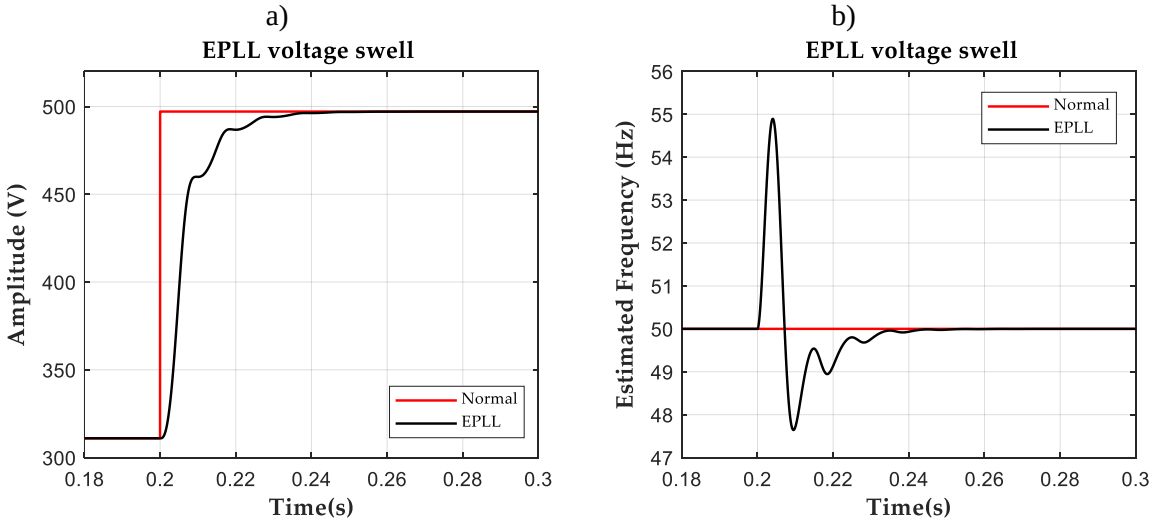

Fig. 30. Response of the EPLL to voltage swell at $t = 0.2s$ going from $1pu$ to $1.6pu$: a) Estimate amplitude, b) Estimate frequency.

2.2.5 SOGI-PLL

The SOGI-PLL is similar to the TD-PLL, but in this case uses a SOGI structure to provide the α and β-components of the grid voltage to the Park transformation. The advantage of using a SOGI instead of a TD is that the SOGI can be tuned with the estimated frequency delivered by the PLL and that the SOGI has filtering capabilities over the provided α and β-components. The SOGI does a band-pass filtering (BPF) over the α-component and low-pass filtering (LPF) on the β-components, which enhances the response of the system to harmonic distortion in the grid. The block diagram of the SOGI-PLL is depicted in Fig. 3, [48-50].

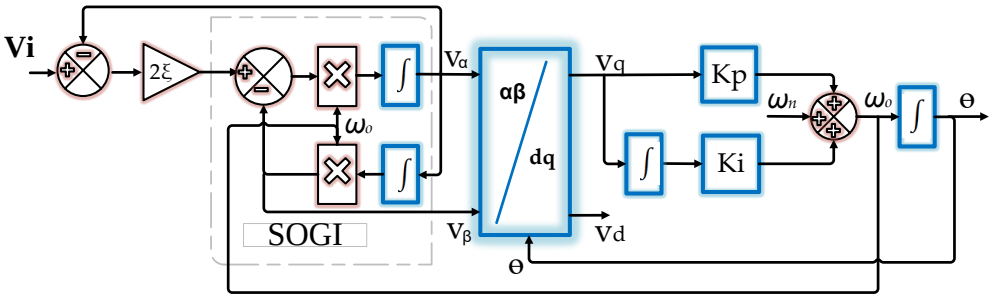

Fig. 31. Block diagram of the SOGI-PLL.

The α and β-components have the following transfer function using the SOGI structure are

$$V_{\alpha\beta}(s) = \begin{bmatrix} V_\alpha(s) \\ V_\beta(s) \end{bmatrix} = \begin{bmatrix} \dfrac{k\omega_o s}{s^2 + k\omega_o s + \omega_o^2} \\ \dfrac{k\omega_o^2 s}{s^2 + k\omega_o s + \omega_o^2} \end{bmatrix} A_g(s) \tag{24}$$

where A_g is defined here also as the amplitude voltage of the grid, $k = 2\xi$ is the SOGI gain, ξ the damping factor, ω_o is the SOGI tuning frequency, and ω_n is the nominal frequency.

The SOGI-PLL has been affected by the same type of perturbations than the performed for the previous PLLs. The parameters in this case are $k_p = 0.24$, $k_i = 10$, $k = 1.4$. The SOGI-PLL has been perturbed by a step change frequency (Fig. 32), DC-offset voltage (Fig. 33), harmonics (Fig. 34), subharmonics (Fig. 35), and voltage sag and voltage swell (Figs. 36 and 37, respectively).

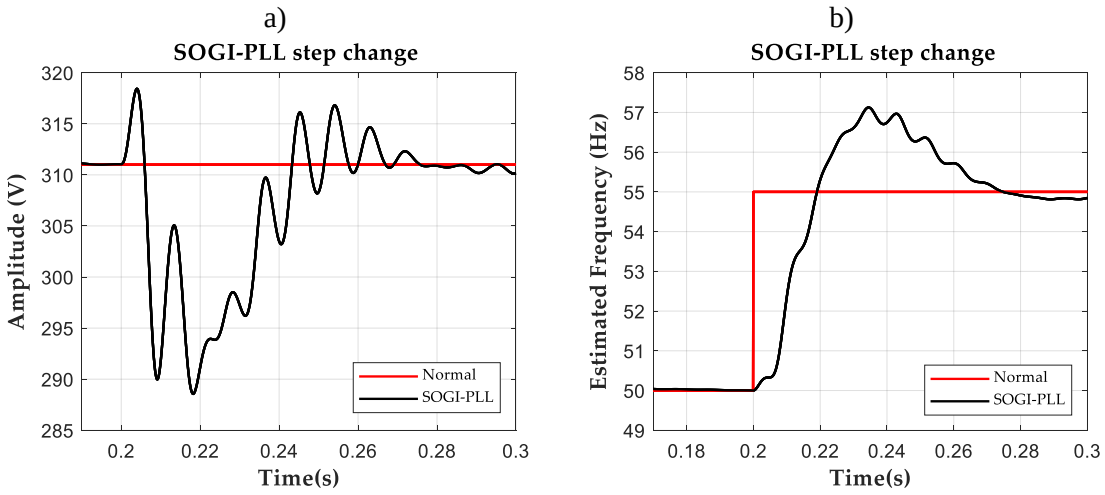

Fig. 32. Response of the SOGI-PLL to a frequency step change in the grid $50Hz$ to $55Hz$ at $t = 0.2s$: a) Estimate amplitude voltage, b) Estimate frequency.

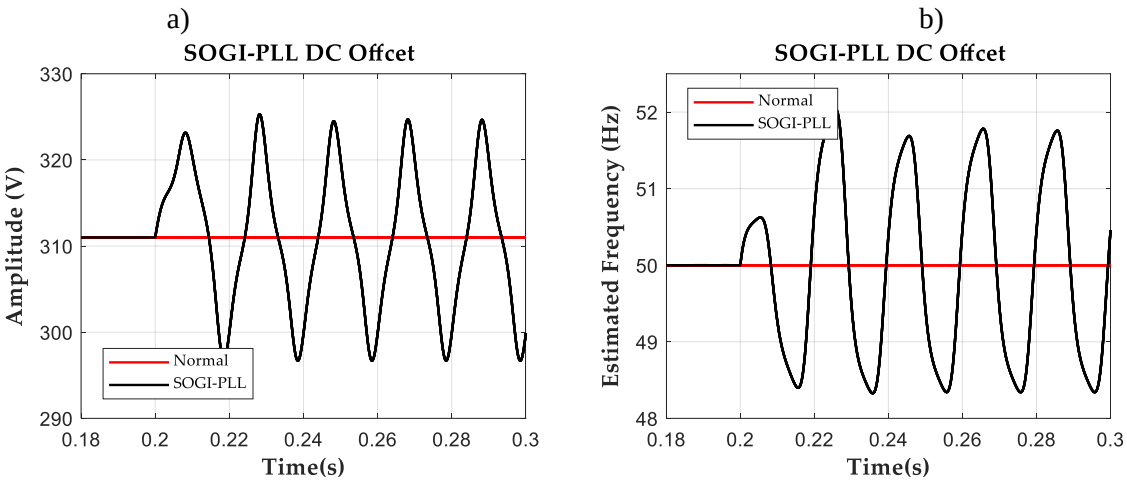

Fig. 33. Response of the SOGI-PLL to the appearance of $10V$ DC-offset in the grid voltage at $t = 0.2s$: a) Estimate amplitude voltage, b) Estimate frequency.

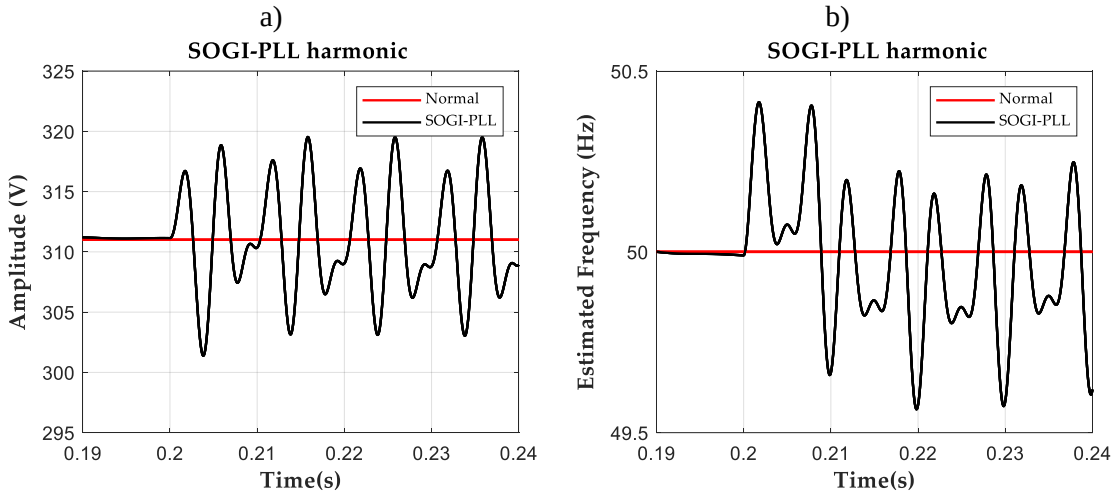

Fig. 34. Response of the SOGI-PLL to a 5th harmonic with 10% amplitude appearing at at $t = 0.2s$: a) Estimate amplitude voltage, b) Estimate frequency.

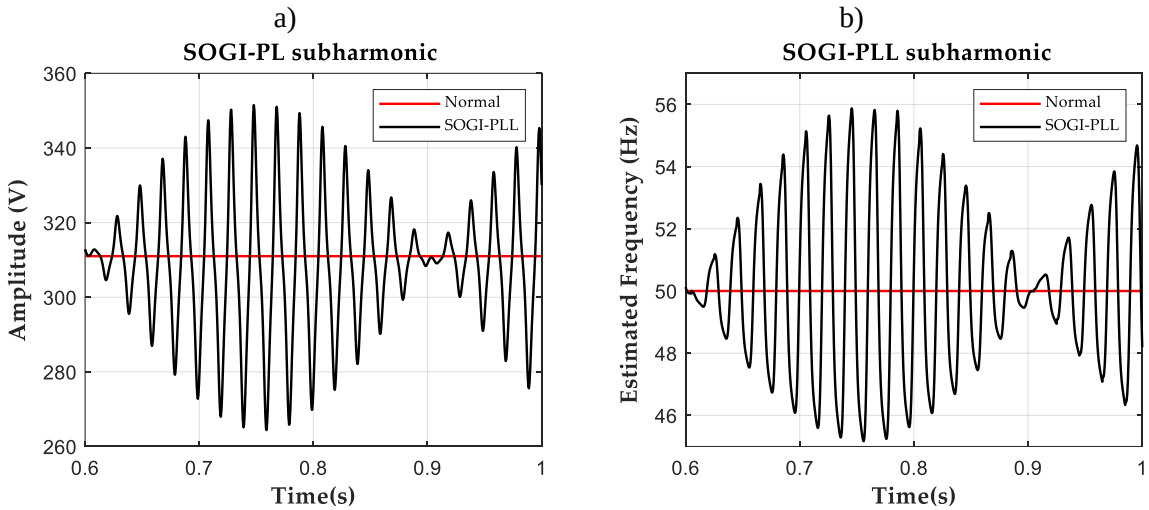

Fig. 35. Response of the SOGI-PLL to a 1.6Hz subharmonic with 10% amplitude: a) Estimate amplitude, b) Estimate frequency.

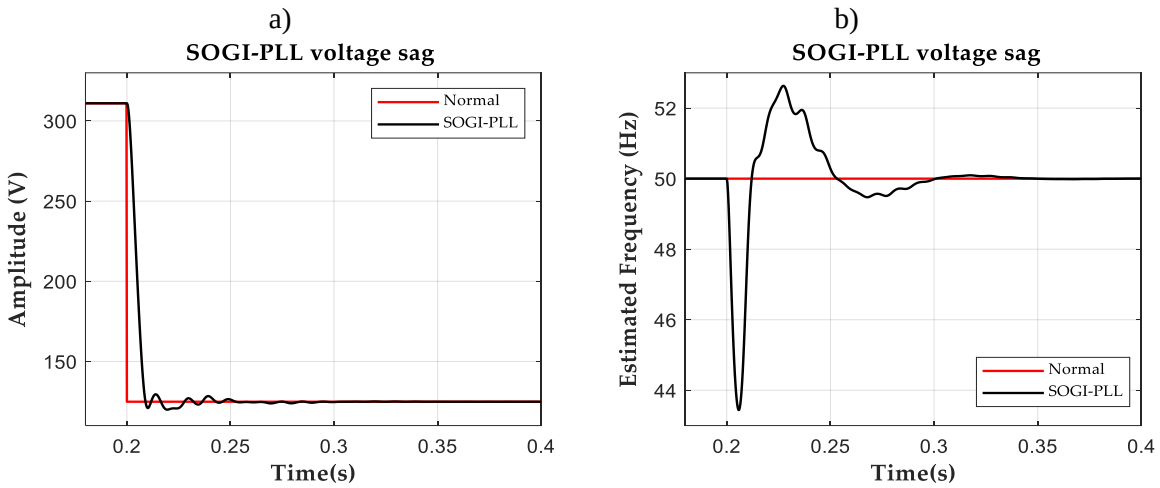

Fig. 36. Response the SOGI-PLL to a voltage sag at $t = 0.2s$ going from $1pu$ to $0.4pu$: a) Estimate amplitude, b) Estimate frequency.

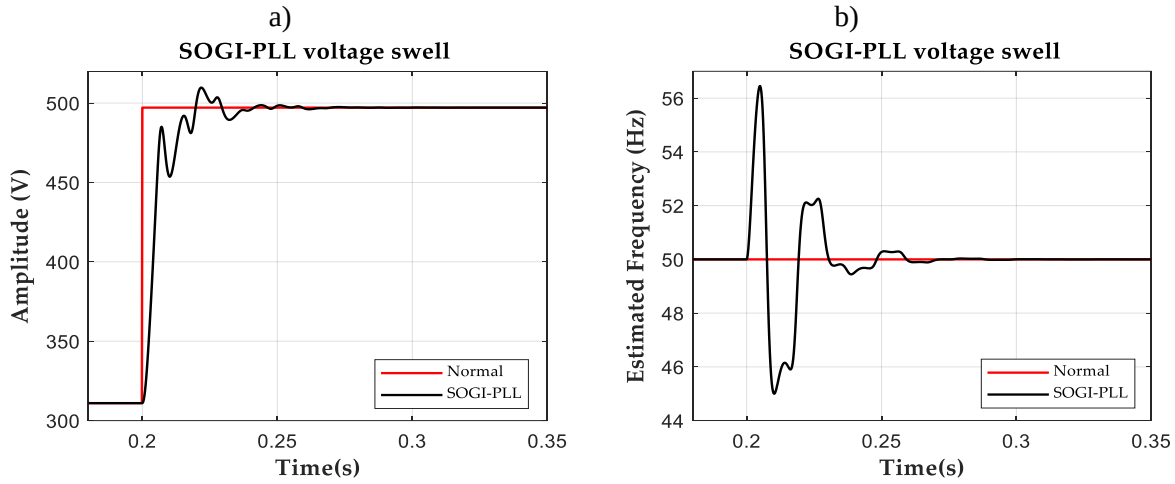

Fig. 37. Response of the SOGI-PLL to voltage swell at $t = 0.2s$ going from $1pu$ to $1.6pu$: a) Estimate amplitude, b) Estimate frequency.

2.2.6 SOGI-FLL

The block diagram of a SOGI-FLL structure is shown at Fig. 38. The SOGI-FLL is a Frequency-Locked-Loop that consist in a gradient descent estimator that provides the estimate of the grid frequency to tune the SOGI filter with the grid frequency [56].

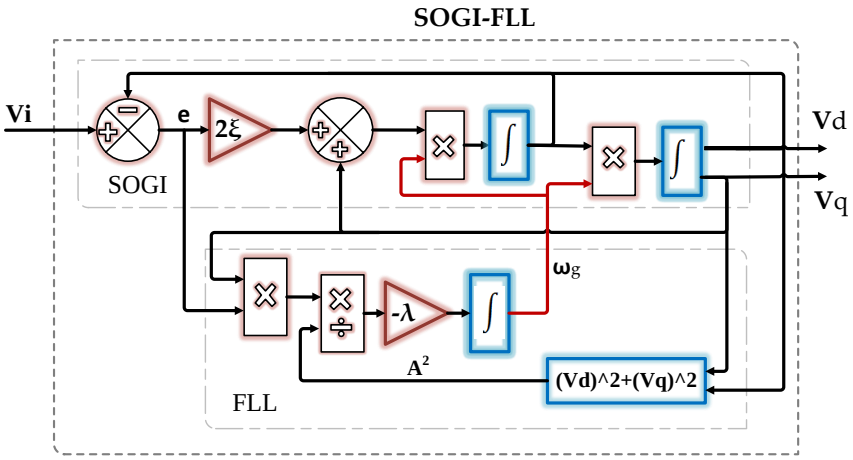

Fig. 38. Block diagram structure of the SOGI-FLL.

The SOGI is a frequency-adjustable resonator that is damped by an outer loop [76,77], shown at Fig. 39. This external loop introduces an error *e* between the SOGI output and the input signal in the resonator input through a gain 2ξ, where the parameter ξ is the damping factor of the system.

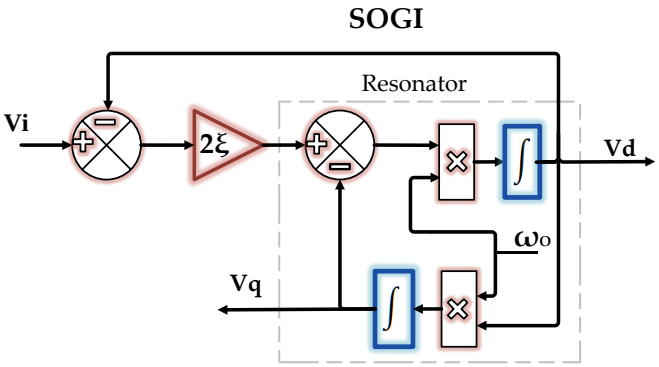

Fig. 39. Block diagram of the SOGI

The SOGI outputs are v_d and v_q, which are in-phase and quadrature-phase with respect to the input signal v_{in}. As mentioned before, the input-to-output point of view, the SOGI behaves as a BPF for v_d, and as a LPF for v_q, with the following transfer functions

$$H_d(s) = \frac{v_d(s)}{v_g(s)} = \frac{2\xi\omega_o \cdot s}{s^2 + 2\xi\omega_o \cdot s + \omega_o^2}, \tag{25}$$

$$H_q(s) = \frac{v_q(s)}{v_g(s)} = \frac{2\xi\omega_o^2}{s^2 + 2\xi\omega_o \cdot s + \omega_o^2}. \tag{26}$$

where ω_o is the input frequency and $0 < \xi < 1$. The Bode magnitude plots of (24) and (26) are depicted in the following Fig. 39 [26, 27], for $\xi = 0.707$.

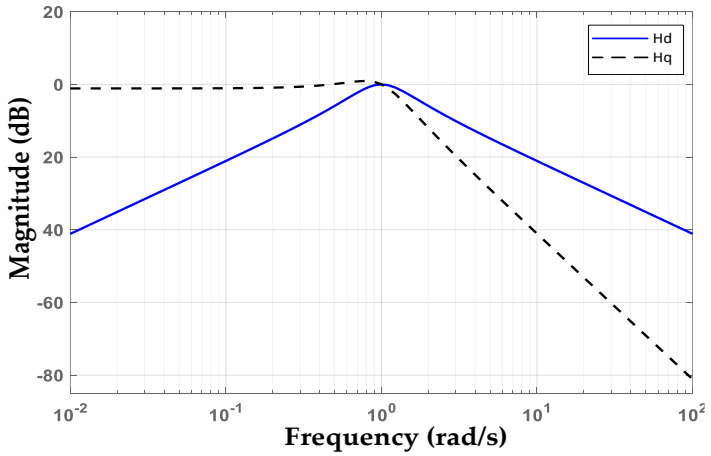

Fig. 40. Magnitude plots of $H_d(s)$ and $H_q(s)$ for $\xi = 0.707$.

The FLL is a grid gradient descent estimator described by the following equation:

$$\frac{d\omega}{dt} = -\frac{\lambda}{A^2} e \cdot v_q \tag{27}$$

where λ is the gain of the FLL, A is the amplitude voltage estimate, and $e = v_{in} - v_d$.

Moreover, the error signal e has a notch-filter (NF) transfer function regarding the input as

$$H_e(s) = \frac{v_e(s)}{v_{in}(s)} = \frac{s^2 + \omega_o^2}{s^2 + 2\xi\omega_o s + \omega_o^2} \tag{28}$$

whose magnitude bode plot of (33) can be seen in Fig. 41 [27].

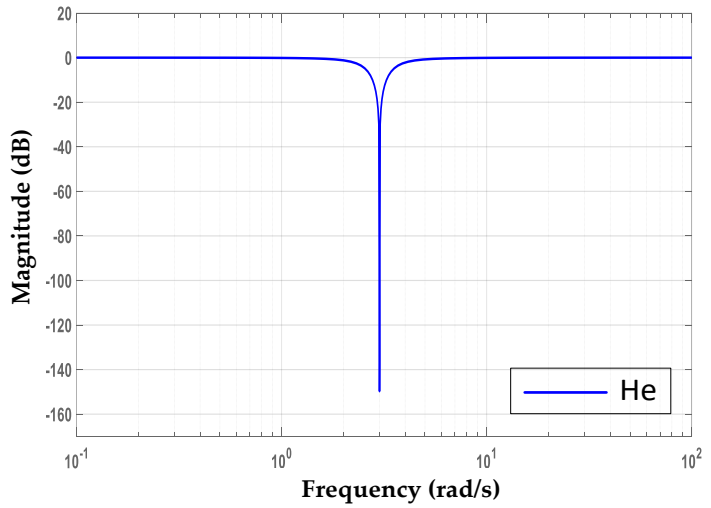

Fig. 41. Magnitude bode diagram of $H_e(s)$ for $\xi = 0.707$.

The damping factor is related with the bandwidth of the SOGI filter, (25) and (26), and, at the same time, determines its transient time response, with the settling time t_s, which comes determined by ξ and ω_o.

$$t_s \approx \frac{4}{\xi\omega_0} \tag{29}$$

It can be seen that the SOGI has a trade-off relationship between harmonic attenuation and settling time, i.e., for small values of ξ, ($\xi << 1$), it has a strong harmonic attenuation, but at an expense of a very slow settling time. As a contrast, for high values of ξ, the time response is fast but with small harmonic attenuation. The presence of subharmonics and DC-offset voltage in the input signal have a direct impact on the SOGI quadrature-phase output, since this output behaves has a LPF with gain $k = 2\xi$. The SOGI-FLL is in fact a system formed by a SOGI coupled by a FLL. The linearized model of the SOGI-FLL in a quasi-locked operating point has a second order dynamic behavior to a frequency change, described in [60,62] as:

$$\frac{\omega(s)}{\omega_g(s)} = \frac{\lambda/2}{s^2+\xi\cdot\omega_n\cdot s+\lambda/2}, \tag{30}$$

where ω_g is the grid frequency and ω_n its nominal value. As seen in (30), the transient response of the estimated frequency to a change in the grid frequency is determined by the system parameters, i.e. the SOGI damping factor ξ and the FLL gain λ. These parameters are also responsible of the estimated frequency behavior, (30). As in the previous cases, the SOGI-FLL has been affected by the same type of perturbations. The parameters in this case are $\lambda = 0.28 \cdot \omega_n^2$, being $\omega_n = 2\pi \cdot 50$ rad/s, and $k = 1.4$. The SOGI-FLL has been perturbed by a step change frequency (Fig. 42), DC-offset voltage (Fig. 43), harmonics (Fig. 44), subharmonics (Fig. 45), and voltage sag and voltage swell (Figs. 46 and 47, respectively).

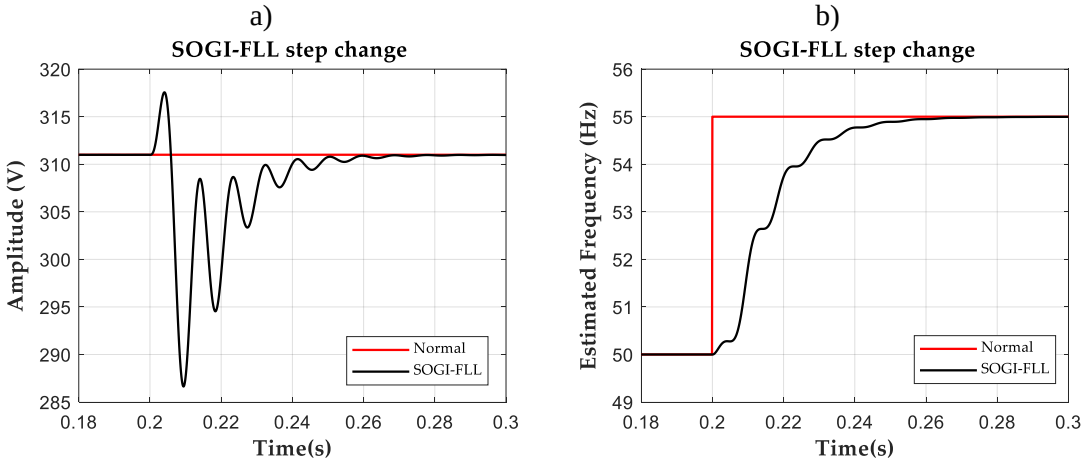

Fig. 42. Response of the SOGI-FLL to a frequency step change in the grid $50Hz$ to $55Hz$ at $t = 0.2s$: a) Estimate amplitude, b) Estimate frequency.

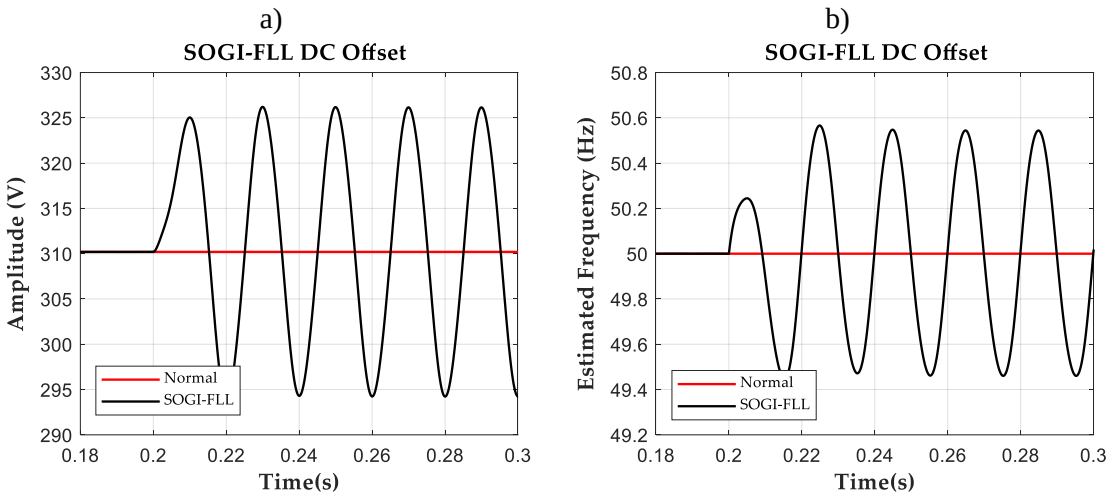

Fig. 43. Response of the SOGI-FLL to the appearance of $10V$ DC-offset in the grid voltage at $t = 0.2s$: a) Estimate amplitude voltage, b) Estimate frequency.

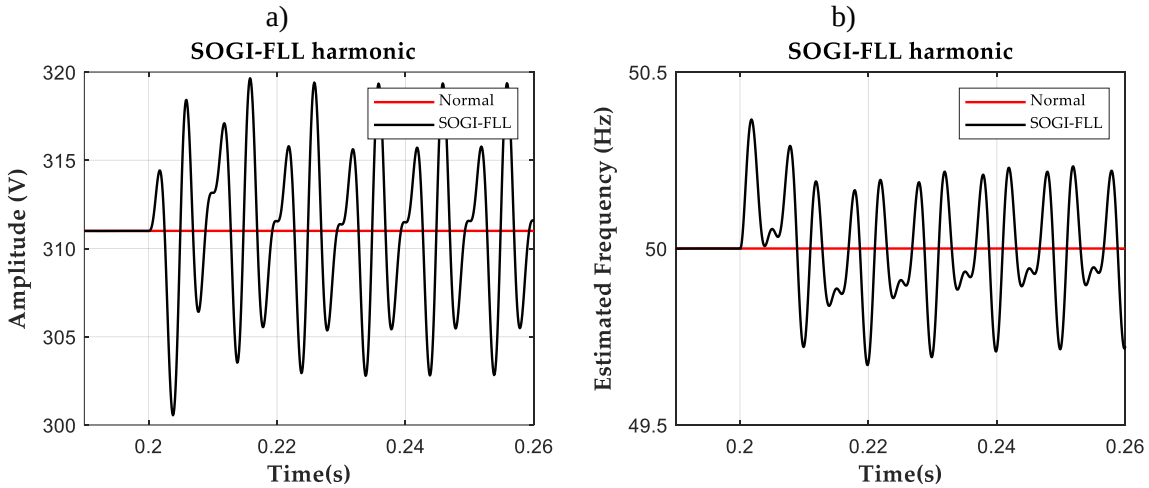

Fig. 44. Response of the SOGI-FLL to a 5th harmonic with 10% amplitude appearing at $t = 0.2s$: a) Estimate amplitude voltage, b) Estimate frequency.

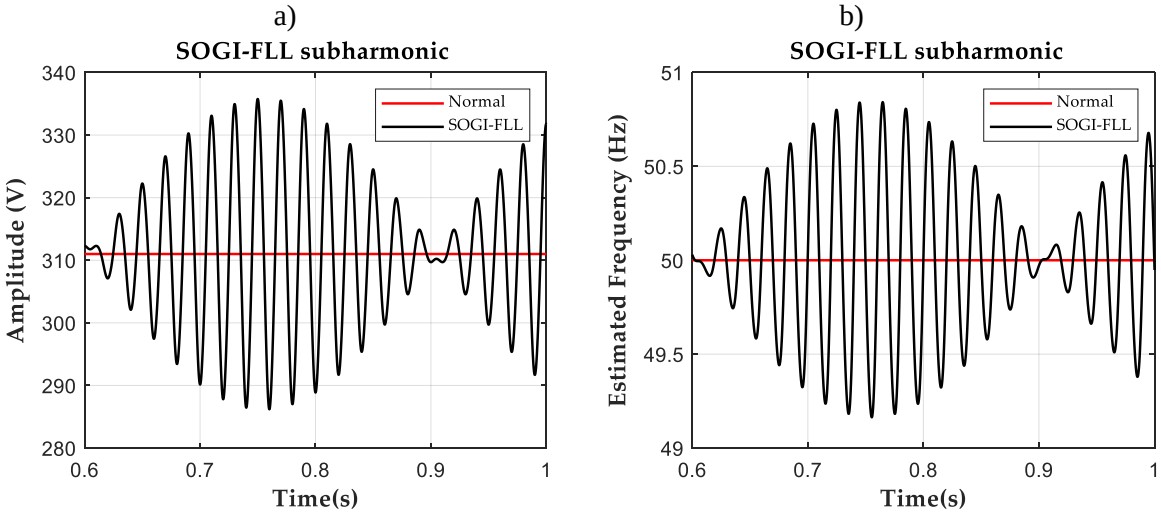

Fig. 45. Response of the SOGI-FLL to a $1.6Hz$ subharmonic with 10% amplitude: a) Estimate amplitude voltage, b) Estimate frequency.

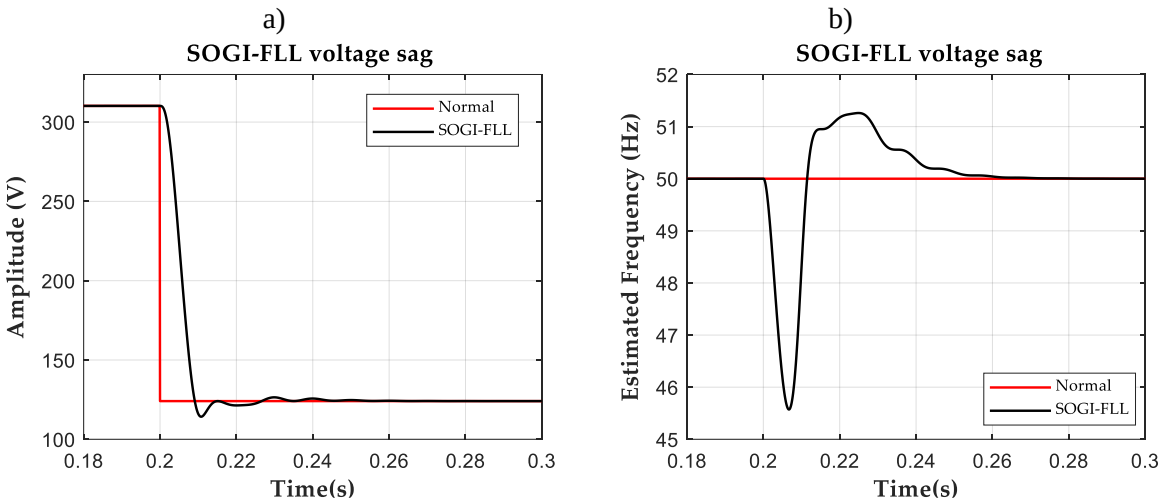

Fig. 46. Response the SOGI-FLL to a voltage sag at $t = 0.2s$ going from $1pu$ to $0.4pu$: a) Estimate amplitude voltage, b) Estimate frequency.

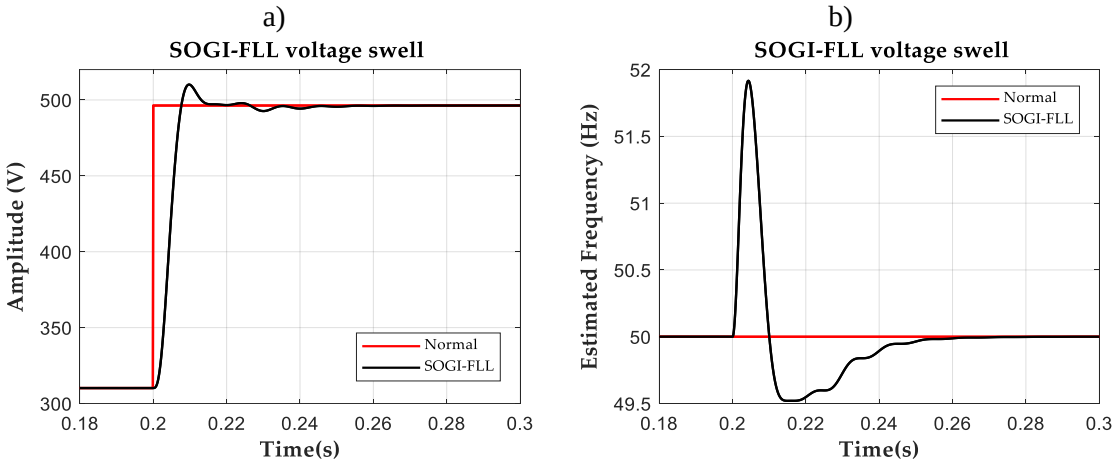

Fig. 47. Response of the SOGI-FLL to voltage swell at $t = 0.2s$ going from $1pu$ to $1.6\ pu$: a) Estimate amplitude voltage, b) Estimate frequency.

2.3 Thesis justification and objectives

At this stage, the behavior of different PLLs and of the SOGI-FLL had been exposed when they had been affected by different types of distortions in the grid voltage. The objective had been to show the impacts that these distortions have on the amplitude voltage and frequency estimates. There are many works presented in literature for studying how to mitigate the impact of these perturbations in these PLLs and in the SOGI-FLL, especially for the case of harmonics, subharmonics and DC-offset [55-59]. However, to our knowledge, there is almost nothing presented regarding mitigating the impact of voltage sags, or swells. Particularly, the case of voltage sags is the most important, because it usually have a deep impact in the frequency estimate achieved by all the methods. Voltage sags are perturbations induced by faults in the grid that, by definition, can arrive until $0.1pu$, which is a big perturbation to face. The voltage sag used to test all the structures had been from $1pu$ to $0.4\ pu$. From simulations can be seen that this fault has a strong impact in the SOGI-FLL. Particularly, the magnitude size of this impact, which could be oscillatory or not, had been measured and is of $7.5Hz$ for the SFR-PLL, $5.3Hz$ for the TD-PLL, $19.6Hz$ for the EPLL, $9.2Hz$ for the SOGI-PLL, and $5.7Hz$ for the SOGI-FLL. Note that the impact is particularly huge for the EPLL. These values are given to have just an idea of the magnitude of the perturbation, which is big considering that the deep of the voltage sag is of a 60%. Have in mind also that the grid frequency should be restrained to be between $\pm 1Hz$ from nominal value ($50Hz$), the perturbation exceed by far these limits. Consider that the magnitude of the impact depends a lot on the deep of the voltage sag and on the gains of the systems. It should also be mentioned that the gains of the PLLs and of the SOGI-FLL had not been tuned to perform a comparison in similar and fear conditions, like to achieve the same overshoot in the transient response to step frequency change, or to achieve the same harmonic ripple amplitude to a given harmonic distortion, which is out of the scope of this thesis. Because voltage sag is a common problem to all the structures, in this thesis the approach to mitigate the impact has been tackled considering only the SOGI-FLL. In this thesis, three consecutive approaches had been studied for the SOGI-FLL that are exposed from now on. Due to the achieved results that mitigate the impact of voltage sags and also of voltage swells, it is expected in future to try to apply these approaches, or similar ones, to the rest of grid monitoring techniques.

3. Analysis of the SOGI-FLL response to voltage sags and swells

The structure of the SOGI-FLL is shown in Fig. 38, where v_g is the grid voltage, ω_o is the center frequency of the SOGI filter, v_d and v_q are the in-phase and quadrature-phase outputs and ω is the FLL estimated grid frequency acting as center frequency of the SOGI filter. The SOGI has a second-order BPF and LPF behavior for $v_d$and v_q [77]. The FLL is a gradient descent estimator [56], defined as:

$$\frac{d\omega}{dt} = -\frac{\lambda}{A^2} e \cdot v_q \,, \tag{31}$$

where A is the estimate of the grid amplitude voltage, $A = \sqrt{v_d^2 + v_q^2}$.

The linearized model of the SOGI-FLL in a quasi-locked operating point regarding the voltage amplitude and frequency is defined in [78, 79], as (32) and (33), depicted in Fig. 48.

$$\frac{A(s)}{A_g(s)} = \frac{\xi\omega_n}{s + \xi\omega_n}, \tag{32}$$

$$\frac{\omega(s)}{\omega_g(s)} = \frac{\lambda/2}{s^2 + \xi\omega_n \cdot s + \lambda/2}, \tag{33}$$

where $\omega_g$and A_g are the frequency and amplitude of the grid voltage, respectively, and ω_n is the nominal value of the grid frequency, $\omega_n = 2\pi 50$ rad/s.

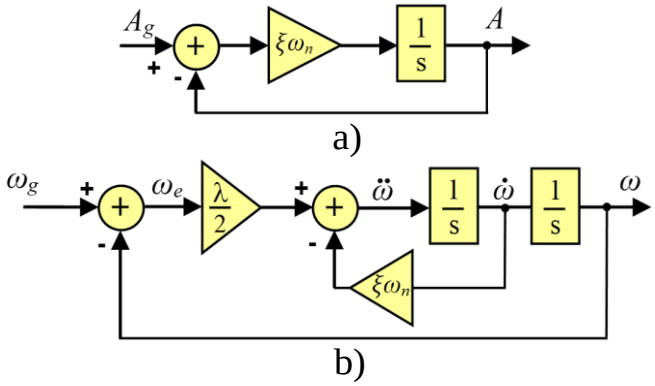

Fig. 48. Linearized models of the SOGI-FLL. a) Estimated amplitude voltage. b) Estimated frequency.

The linearized models of (32) and (33) allow to obtain the transient response of estimates A and ω for a sudden change in A_g and ω_g, respectively, for a given value of ξ and λ. The model of (32) is of a first-order system with constant time $\tau = 1/\xi\omega_n$ and, from linear control theory, it is well known that using $\xi = 1/\sqrt{2}$ an optimal relationship is achieved in the transient response of the system. The model of (33) corresponds to a second-order system, whose transient response comes determined by the roots of (34)

$$s^2 + \xi\omega_n \cdot s + \lambda/2 = 0 \,. \tag{34}$$

In (34), it can be seen that $\xi\omega_n$ and $\lambda/2$ are related to the damping factor, ξ', and natural undamped frequency, ω', respectively, in the standard definition of a second-order system, i.e. a system with

roots $s^2 + 2\xi'\omega' \cdot s + (\omega')^2 = 0$. Then, by identifying $\xi\omega_n = 2\xi'\omega'$ and $\lambda/2 = (\omega')^2$, it can be inferred that

$$\lambda = 2(\omega')^2 , \tag{35}$$

and extracting ω' from the other identification

$$\omega' = \frac{\xi\omega_n}{2\xi'} , \tag{36}$$

and, putting (36) in (35) leads to

$$\lambda = \frac{\xi^2\omega_n^2}{2\xi'^2} , \tag{37}$$

which choosing the optimal $\xi' = \xi = 1/\sqrt{2}$ leads to a transient response that only relies on λ

$$\lambda = 0.5\omega_n^2 . \tag{38}$$

Therefore, by inserting these gains, ξ and λ, in (34) gives roots located $s_{1,2} = -111.07 \pm 111.07j$, which corresponds to a transient response in ω that achieves an overshoot of $Mp = 4.32\%$, depicted in blue as the pair of gains (ξ_1, λ_1) in Fig. 49.

By choosing this pair of gains, the transient response is optimal for the second-order system. From the harmonic rejection point of view, it implies that a3rd harmonic with a 3% amplitude voltage regarding nominal produces a ripple distortion around ω of 0.435Hz, measured peak-to-peak. However, another interesting design point can be chosen instead for $\lambda = 0.25\omega_n^2$ that corresponds to double roots at $s_{1,2} = -111.07$, i.e. a transient response without overshoot depicted in red as the pair (ξ_2, λ_2) in Fig. 49. In this case, as the gain has been reduced by half, an extra attenuation to harmonics has been achieved and the ripple is reduced also by half, to $0.217Hz$. Notice that this gain can be considered as an optimal election from the point of view of rejection capability to harmonic distortion and speed in the transient response. From now on, λ_1 and λ_2 are considered as two reference optimal gains for facing the perturbation induced by voltage sags and swells in the estimated frequency.

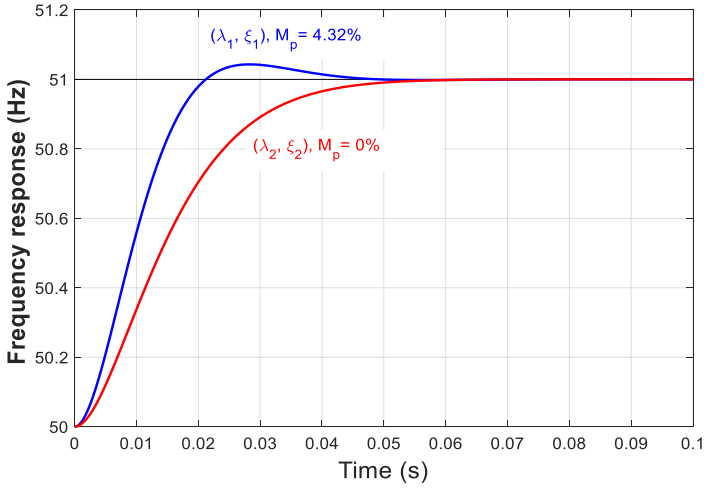

Fig. 49. Linearized response to a frequency step perturbation of 1 Hz for two sets parameters: ($\xi_1 = 0.707$, $\lambda_1 = 0.5\omega_n^2$), in blue with $Mp = 4.32\%$ and ($\xi_2 = 0.707$, $\lambda_2 = 0.25\omega_n^2$), in red with $Mp = 0\%$.

Regarding the impact of voltage sags in the SOGI-FLL, the model in (32) can be used to obtain the transient response to the fault in the estimated grid voltage amplitude. But the model in (33) can provide the transient response of ω to a perturbation in the grid frequency, ω_g, but not to changes in A_g since there are no-crossing terms between (32) and (33). Therefore, the impact in ω should be assessed using the real model depicted in Fig. 38. And, it is well known that the impact of voltage sags in the estimated ω_g is really high. Moreover, the transient response induced by the fault is nonlinear, and its magnitude size depends nonlinearly on the voltage sag's depth, being worst for the deepest voltage sags.

Fig. 50 provides an idea about the high impact of the perturbation induced in the estimated frequency by a voltage sag. Fig. 50.a depicts the estimated frequency for a series of voltage sags ranging from $0.8\,pu$ to $0.2\,pu$ for the optimal pair ($\xi_1 = 0.707$, $\lambda_1 = 0.5\omega_n^2$). Fig. 50.b depicts the measured peak-to-peak value of the perturbation for each case. In this figure the two pair of optimal gains, ($\xi_1 = 0.707$, $\lambda_1 = 0.5\omega_n^2$) and ($\xi_2 = 0.707$, $\lambda_2 = 0.25\omega_n^2$), had been considered. Notice that the size of the perturbation for λ_1 can arrive to 12Hz for the pair (ξ_1, λ_1) and of $5Hz$ for (ξ_2, λ_2).

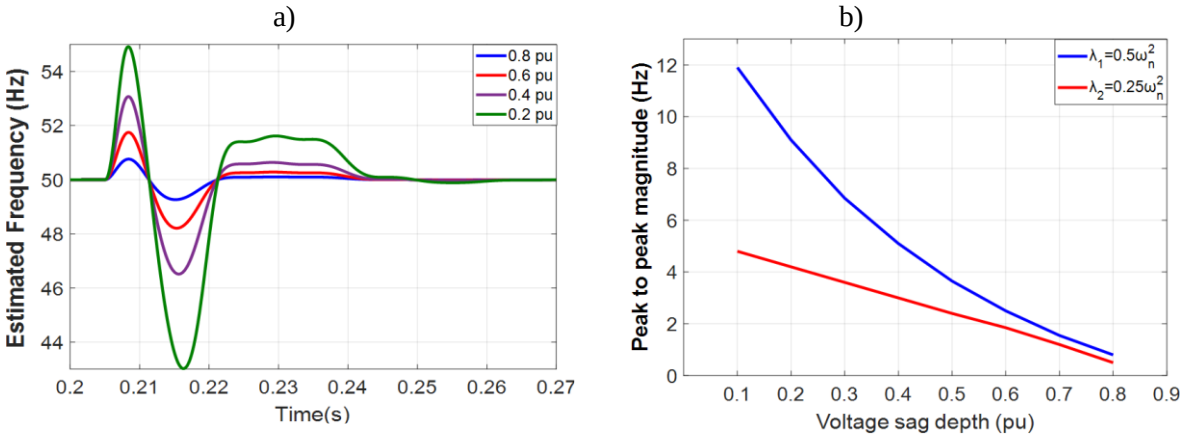

Fig. 50. a) Estimated frequency perturbations in the SOGI-FLL for different voltage sag depths ranging from $0.8pu$ to $0.2pu$ and FLL gain $\lambda_1 = 0.5\omega_n^2$. b) Measured peak-to-peak maximum amplitude distortion in Hz, in blue for $\lambda_1 = 0.5\omega_n^2$, in red for $\lambda_2 = 0.25\omega_n^2$.

A similar impact, but with less peak-to-peak size, can be observed for a voltage swell in Fig. 51.a for voltage swells ranging from $1.2\,pu$ to $1.8\,pu$ and for the pair (ξ_1, λ_1). Also, Fig. 51.b depicts the measured peak-to-peak magnitude for the two pair of optimal gains, (ξ_1, λ_1) in blue and (ξ_2, λ_2) in red.

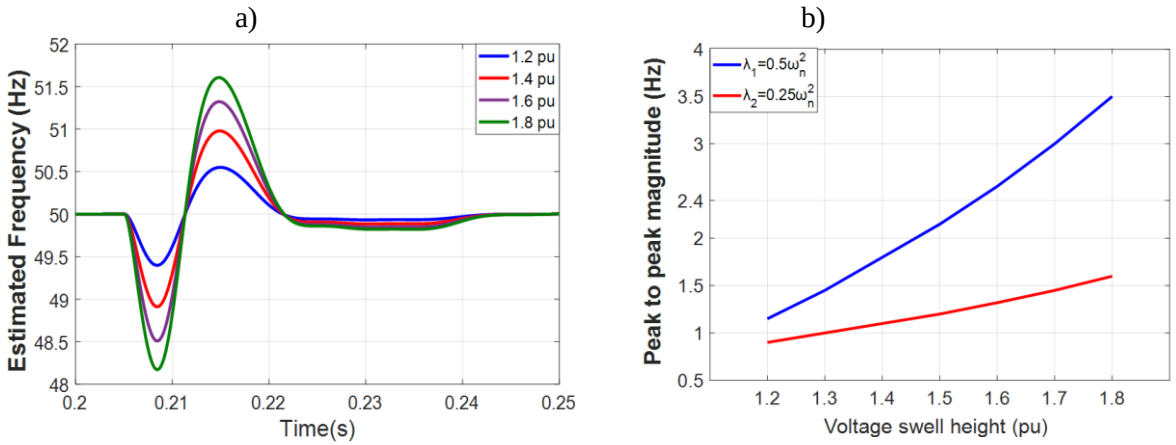

Fig. 51. a) Estimated frequency perturbations in the SOGI-FLL for different voltage sag swells ranging from 1.2 pu to 1.8 pu and FLL gain $\lambda_1 = 0.5\omega_n^2$. b) Measured peak-to-peak maximum amplitude distortion in Hz, in blue for $\lambda_1 = 0.5\omega_n^2$, in red for $\lambda_2 = 0.25\omega_n^2$.

3.1 Impact voltage of sags and swells on the SOGI's v_d and v_q outputs

Voltage sags and swells, because of the perturbation induced in ω, cause noticeable errors in the outputs of the SOGI filter, v_d and v_q. During the fault, ω swings around its nominal value, ω_n, and causes attenuations in v_d and v_q through the SOGI's BPF and LPF transfer functions of (32) and (33). To assess these errors, the SOGI outputs (depicted in the SOGI-a block of Fig. 52) had been compared with the outputs of an identical SOGI (depicted as SOGI-b), operating at fixed nominal frequency.

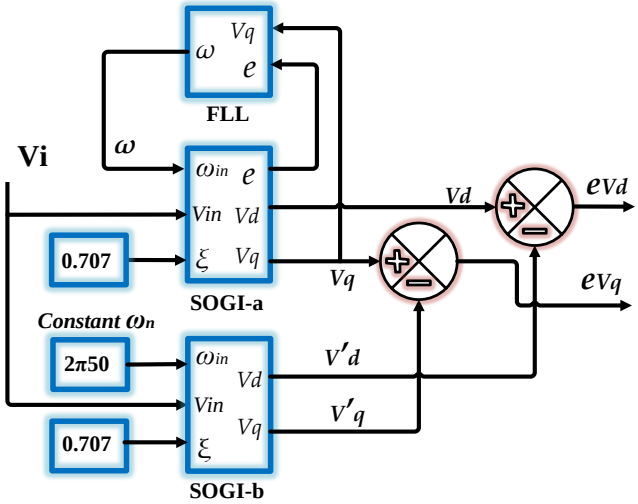

Fig. 52. Structure comparison employed for assessing the errors induced by voltage sags at the outputs of the SOGI-FLL filter.

Fig. 53 shows the magnitude of these errors for the same voltage sags simulated in Fig. 50.a. In this figure, for $ev_d = v_d - v'_d$ the peak-to-peak size arrives to $83.7V$ and for $ev_q = v_q - v'_q$ to $82.8V$, which supposes respectively a 27% and 26.7% of A_n. This assessment has been performed also for voltage swells, which for the worst case arrives to $37V$ for ev_d and $57V$ for ev_q, i.e. an 11.9% and 18.3% of the level of A_n. Therefore, According to the Table 1, the impact of sags and swells in the performance of the SOGI-FLL can be considered as strong.

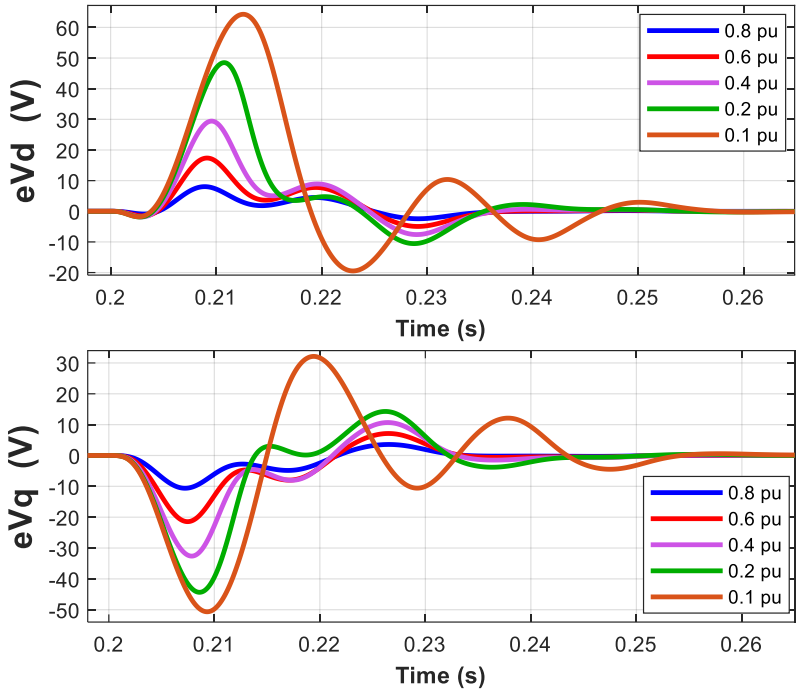

Fig. 53. Induced errors on the outputs of the SOGI filter, ev_d and ev_q, due to the impact of voltage sags with different depth size.

Table 1. Peak-to-peak magnitude ev_d and ev_q.

Sag depth level (pu)	ev_d (V)	ev_q (V)
0.1	83.7	82.8
0.2	58.4	56.7
0.4	35.8	34. 6
0.6	21	24
0.8	13	15

4. Approaches to mitigate the impact of voltage sags and swells

4.1. SOGI-FLL with a saturation approach

The first approach to face the fault is simply the insertion of a saturation block at the output of the FLL in order to bound the frequency estimation to the $49Hz - 51Hz$ band, see Fig. 54.

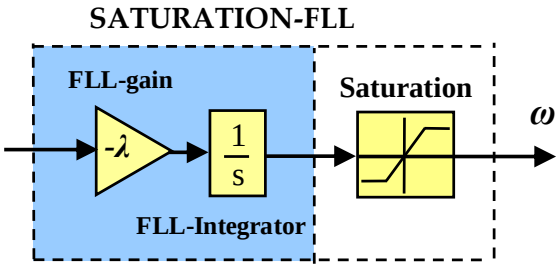

Fig. 54. FLL with a saturation block.

Fig. 55 depicts the simulation results of this approach. Note that the frequency is limited to the bounds, which limits the frequency to $\pm 1Hz$ around nominal. Note that the perturbation is reduced but that the transient time response last almost the same that without doing nothing.

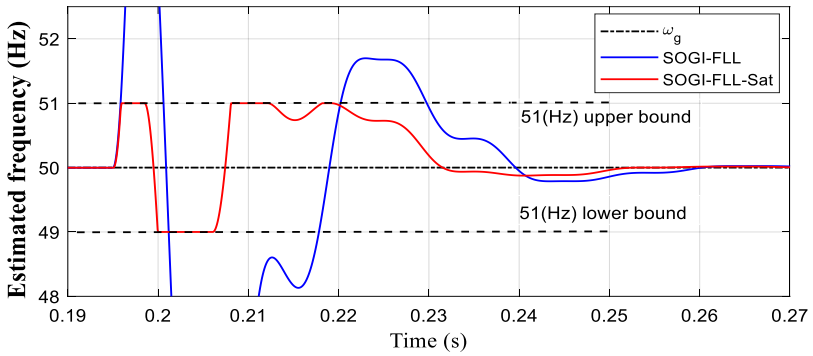

Fig. 55. SOGI-FLL response to an 80% depth type-a voltage sag. In blue: without a saturation block. In red: with a saturation block.

4.2. SOGI-FLL with a FSM approach

The SOGI-FLL response can be further improved by adopting a finite state machine (FSM) for identifying different stages in the frequency response of the system. This approach allows defining better gain-parameters for each stage of the response, in order to reduce the distortion impact and improve the transient response. A total of five stages in the operation of the SOGI-FLL during the fault are employed for the definition of the FSM.

A FSM is normally used in the definition of automatic control actions for the control of a wide variety of systems. It is defined according to the states identified in the operative steps needed to perform a given process. The FSM evolves from one state to another according to the value of its inputs and outputs in a given moment [80, 81]. The proper tuning of the SOGI-FLL parameters is the key point to optimize its response through each one of the possible stages at the face of a fault. The optimization objective consists into carrying out the system to normal condition as soon as possible with the aim of reduction the time duration of the perturbation and its impact.

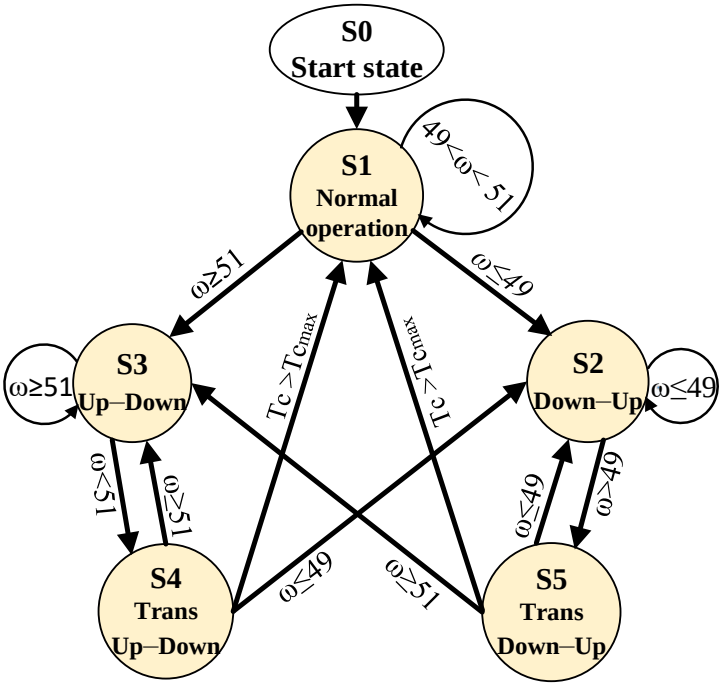

Fig. 56. Proposed FSM for the SOGI-FLL.

In this work, the operation of the SOGI-FLL during a fault is depicted in the FSM of Fig. 56 in which the following five stages are defined:

4.2.1. State S1. Normal operation

The FLL frequency is between the maximum (51Hz) and minimum ($49Hz$) bounds. The SOGI-FLL operates with nominal parameters, designed for obtaining a given estimated frequency behavior. In this work the nominal parameters are $\xi = 0.707$ and $\lambda = 0.28 \cdot \omega_n^2$ (rad/s^2). In this state, the system is waiting for a fault event and the FSM will not perform any action until a saturation bound is reached.

4.2.2. State S2. Down-saturation

The FLL frequency goes below 49Hz due to a fault event and the FSM keeps the output frequency saturated to $49Hz$. Here, ξ and λ parameters are changed to different values designed by a trial and error procedure, in order to minimize the duration of the SOGI-FLL time response.

4.2.3. State S3. Up-saturation

The FLL frequency goes beyond $51Hz$ due to a fault and the FSM holds the output frequency saturated to $51Hz$. Then, ξ and λ are optimized in order to achieve a better transient response.

4.2.4. State S4. Up to Down transient

The FSM transits from state S3 (up-saturation) to S4 when the FLL frequency is lower or equal to $51Hz$. Once in S4, the FSM might transit to three different states: either to S2 (down-saturation) if the FLL frequency reduces below $49Hz$, or to S3 (up-saturation) if the FLL frequency exceeds again $51Hz$, or to S1 (normal operation). The transition from S4 to S1 is decided by a counter T_C which is activated whenever the FLL frequency enters a narrow $\pm 0.02\%$ band, named as Δ, around $50Hz$, i.e. between 50.1Hz and $49.9Hz$, respectively. The counter Tc is reset if the FLL

frequency leaves this band. Therefore, a return to normal state S1 is only produced if Tc reaches a given maximum value $T_{C_{max}}$, i.e Tc $\geq T_{C_{max}}$.

4.2.5. State S5. Down to Up transient.

S5 is reached from S2 (down –saturation) when the FLL frequency is higher or equal to $49Hz$. Once in S5, the FSM can either go to S3 (up-saturation), or return back to S2 (down-saturation), or go to S1 (normal operation). The returning mechanism to the S1 state is the same defined previously for S4. If $T_C > T_{C_{max}}$ then the FSM returns to S1.

Fig. 57 depicts an example of a usual response of the SOGI-FLL during a voltage sag. Note in this figure how the FSM goes from S1 to S3 when the voltage sag begins, and then transits from S3 to S4, then to S2, then to S5, and finally returns to S1. It can be seen how at S5 the estimated frequency enters inside the boundary labeled as 2Δ. From this moment, the counter T_C is started and the FSM returns to normal state S1 when the maximum count $T_{C_{max}}$ is reached, i.e. when $T_C > T_{C_{max}}$. Note that the checking of the returning condition illustrated for a response entering in the S5 state also applies the responses entering state S4.

Fig. 57 depicts an example of a usual response of the SOGI-FLL during a voltage sag. Note in this figure how the FSM goes from S1 to S3 when the voltage sag begins, and then transitions from S3 to S4, then to S2, then to S5, and finally returns to S1. It can be seen how at S5 the estimated frequency enters the boundary labeled as 2Δ. From this moment, the counter T_C is started, and the FSM returns to normal state S1 when the maximum count $T_{C_{max}}$ is reached, i.e., when $T_C > T_{C_{max}}$. Note that the checking of the return condition illustrated for a response entering the S5 state also applies to responses entering the S4 state.

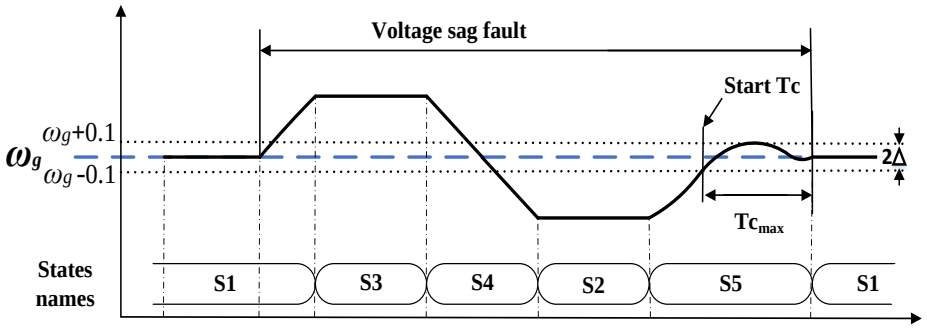

Fig. 57. Example of the FSM evolution during a voltage sag.

Fig. 58 shows the transient responses to a 90% depth type-a voltage sag of the unsaturated (in blue) and the saturated (in red) SOGI-FLL and also of the FSM-based SOGI-FLL (in green).

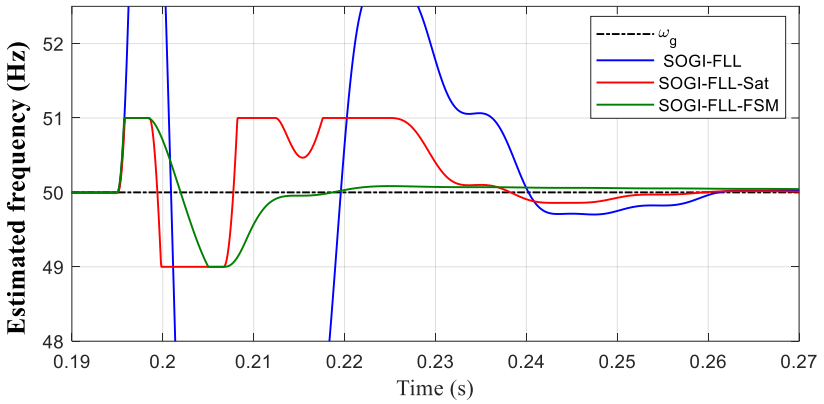

Fig. 58. Transient response to a 90% depth type-a voltage sag. In blue: SOGI-FLL. In red: SOGI-FLL with saturation. In green: FSM-based SOGI-FLL.

During the fault, the FSM-based SOGI-FLL is operated with different ξ and λ gains for each state. The SOGI gain has been optimized by a series of trial and error simulations for 90%, 80%, 60% and 40% sag depths and the parameter values are shown at upper section of Table 2. (notice that λ is expressed as a fraction of ω_n^2).

Table 2. FSM-based SOGI-FLL parameters for 90% to 40% depth type-a and type-b voltage sags.

Parameter	**State**				
Type-a	**S1**	**S2**	**S3**	**S4**	**S5**
$\lambda_{90\%}$	0.28	0.07	0.07	0.08	0.05
$\lambda_{80\%}$	0.28	0.11	0.11	0.1	0.07
$\lambda_{60\%}$	0.28	0.12	0.12	0.14	0.13
$\lambda_{40\%}$	0.28	0.2	0.2	0.22	0.19
$\xi_{90\%}$	0.707	0.8	0.8	0.8	0.8
$\xi_{80\%}$	0.707	0.75	0.75	0.75	0.75
$\xi_{60\%}$	0.707	0.65	0.65	0.65	0.65
$\xi_{40\%}$	0.707	0.55	0.55	0.55	0.55
Type-b	**S1**	**S2**	**S3**	**S4**	**S5**
$\lambda_{90\%}$	0.28	0.07	0.07	0.04	0.03
$\lambda_{80\%}$	0.28	0.11	0.11	0.1	0.034
$\lambda_{60\%}$	0.28	0.12	0.12	0.2	0.055
$\lambda_{40\%}$	0.28	0.2	0.2	0.3	0.08
$\xi_{90\%}$	0.707	0.75	0.75	0.75	0.75
$\xi_{80\%}$	0.707	0.7	0.7	0.7	0.7
$\xi_{60\%}$	0.707	0.6	0.6	0.6	0.6
$\xi_{40\%}$	0.707	0.5	0.5	0.5	0.5

The same procedure has been carried out for voltage sags of type-b. The values of ξ and λ are shown at the lower section of Table 2. Fig. 59 shows the transient responses to a 90% sag of the SOGI-FLL (in blue) and the saturated (in red) SOGI-FLL and also of the FSM-based SOGI-FLL (in green) for this case. As seen in Fig. 59 the FSM-based transient response returns faster to normal operation.

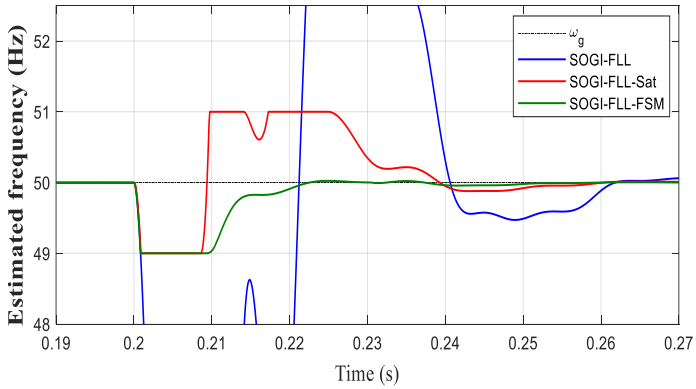

Fig. 59. Transient response to a 90% depth type-b voltage sag. In blue: unsaturated SOGI-FLL. In red: SOGI-FLL with saturation. In green: FSM-based SOGI-FLL.

As seen in Table 2, for each state and each depth percentage of a voltage sag, there is a progression in the values of ξ and λ. In general, there is an increase in the values of λ and ξ as the voltage sag depth decreases. This behavior allows determining the sustained progression trend of the parameters according to the sag depth. To do that, the sag depth is determined as:

$$x = 1 - A_{pu}\,, \tag{39}$$

where A_{pu} is the estimated peak voltage amplitude in pu (i.e. $A_{pu} = A/A_n$,where $A_n = \sqrt{2} \cdot 230V_{rms}$ is the nominal grid voltage amplitude) and **x** is the voltage sag depth in pu. A is obtained by means of the quadrature outputs of the SOGI as (see Fig. 38)

$$A = (v_d{}^2 + v_q{}^2)^{1/2}. \tag{40}$$

Now, with (39) and (40) the equations depicted in Table 3, can be used for obtaining λ for type-a and -b sags and for any depth ranging from 40% to 90%. In the case of ξ, the relationship is simpler and only two equations are needed, one for type-a and another for type-b the equations are depicted in Table 4.

Table 3. Equations expressing λ as a function of the sag depth x for each of the FSM states and sag types.

State	$\lambda = f(x)$ equation
Type-a	
S_2 & S_3	$\lambda = -4.58x^3 + 9.37x^2 - 6.39x + 1.57$
S_4	$\lambda = 0.36x^2 - 0.74x + 0.46$
S_5	$\lambda = 0.09x^2 - 0.41x + 0.34$
Type-b	
S_2 & S_3	$\lambda = -4.58x^3 + 9.37x^2 - 6.39x + 1.57$
S_4	$\lambda = -0.09x^2 - 0.39x + 0.47$
S_5	$\lambda = 0.1x^2 - 0.23x + 0.15$

Table 4. Equations expressing ξ as a function of the sag depth x for each of the FSM states and sag types.

Sag-type	$\xi = f(x)$ equation
Type-a	$\xi = 0.5x$+0.35
Type-b	$\xi = 0.5x$+0.3

Figs. 60 and 61 show the results of using the equations of Table 3 and 4, for obtaining ξ and λ parameters for type-a and -b sags and for 70% and 50% sag depths, respectively. Observe in these figures that the FSM-based SOGI-FLL response is less oscillating and faster than the others with a smooth returning to normal state of operation.

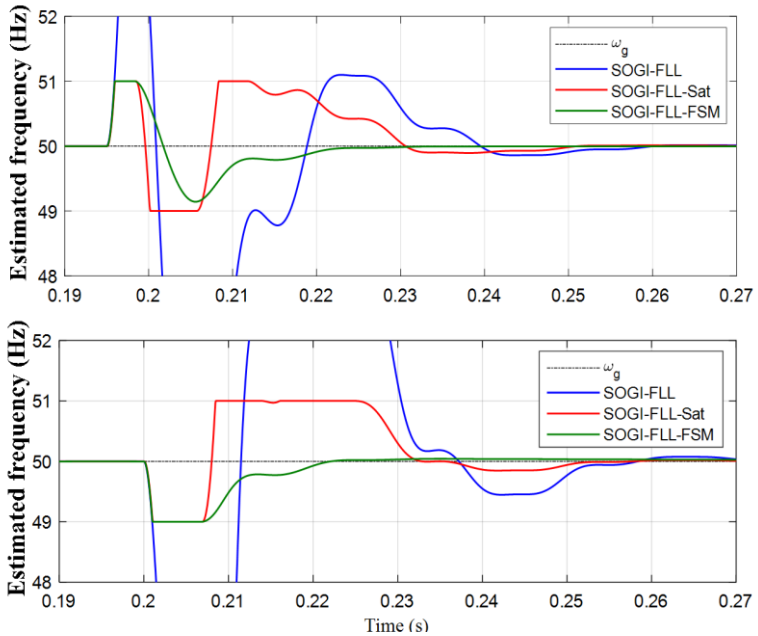

Fig. 60. Transient responses to an 70% sag depth using the equations of Table 3 and 4 for obtaining ξ and λ. In blue: SOGI-FLL. In red: SOGI-FLL with saturation. In green: FSM-based SOGI-FLL Upper: type-a sag. Lower: type-b sag.

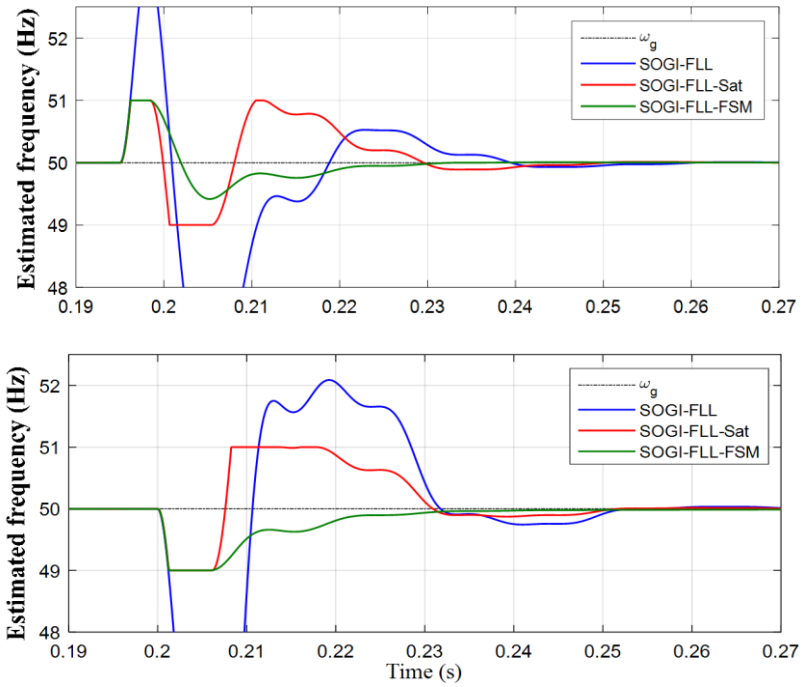

Fig. 61. Transient responses to an 50% sag depth using the equations of Table 3 and 4 for obtaining ξ and λ. In blue: unsaturated SOGI-FLL. In red: SOGI-FLL with saturation. In green: FSM-based SOGI-FLL Upper: type-a sag. Down: type-b sag.

The recovering times of the three SOGI-FLL schemes have been obtained for different sag depths, as shown in Table. 5. The percentage time reduction of the FSM scheme regarding the SOGI-FLL has also been evaluated. Notice has the FSM-based method achieves the better results for the deeper voltage sags.

Table 5. Recovering times of the different SOGI-FLL schemes for various voltage sag depths.

Sag depth	SOGI-FLL UNSAT(s)	SOGI-FLL SAT(s)	SOGI-FLL FSM(s)	% of reduction
90%	0.0439	0.0354	0.0150	66%
80%	0.0433	0.0349	0.0164	62%
70%	0.0422	0.0337	0.0213	50%
60%	0.0374	0.0324	0.0218	42%
50%	0.0360	0.0302	0.0227	37%
40%	0.0349	0.0271	0.0228	35%

4.3. FSM Modification LPF Approach

The FSM was initially designed and simulated for working at a constant $50Hz$ grid nominal frequency, with fixed saturation bounds at $\pm 1Hz$ regarding the nominal value (or $\pm 2\pi$ rad/s). Therefore, the FSM cannot work properly when the grid frequency is outside these boundaries. Then, the FSM scheme was modified for being able of tracking the grid frequency changes. The modification can be seen in Fig. 62, which consists in including a LPF in the path supplying the estimated grid frequency ω to the FSM. The LPF is of first-order and has the following transfer function:

$$\omega_{LPF}(s) = \frac{a}{s+a}\omega(s), \tag{41}$$

where ω_{LPF} is the LPF output and $a = 2\pi f_c$ is its cutoff frequency (rad/s).

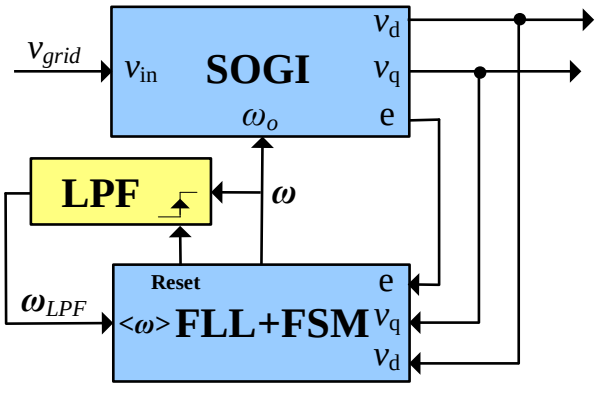

Fig. 62. Block diagram structure of the SOGI-FLL-FSM including a LPF for tracking of the grid frequency.

The LPF is designed for having a low cutoff frequency, with the purpose of achieving the average of the estimated frequency, i.e:

$$\omega_{LPF}(t) = < \omega(t) >, \tag{42}$$

where $< >$ means average. Then, the LPF transient response is slow and serves as an analog memory of the value that the estimated grid frequency ω had just before the fault event. The ω_{LPF} signal is introduced as a new input to the FSM and is used for defining the saturation bounds levels, which are now variable. The saturation bounds are determined during the normal operation of the FSM, at state S1, and are defined as:

$$\omega_{SAT_{up}} = \omega_{LPF} + 2\pi, \tag{43}$$

$$\omega_{SAT_{down}} = \omega_{LPF} - 2\pi, \tag{44}$$

where $\omega_{\mathrm{SAT_{up}}}$ and $\omega_{\mathrm{SAT_{down}}}$ are the FSM upper and lower saturation bounds (rad/s). The functioning of (43)-(44) can be well understood using the time response depicted in Fig. 63, which shows the FSM and ω_{LPF} transient responses to an 80% depth voltage sag happening at $t = 0.195s$. The LPF had a cutoff frequency of $\omega_c = 10\pi$ rad/s.

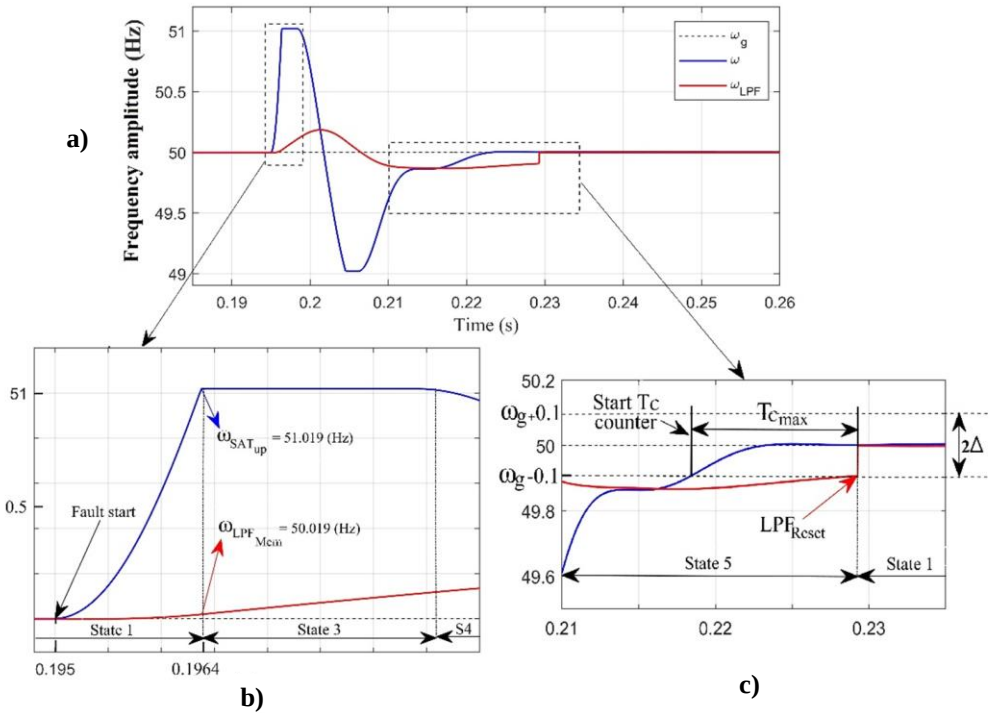

Fig. 63. Estimated grid frequency ω and its average value ω_{LPF} transient responses to an 80% depth voltage sag happening at $t = 0.195s$. a) ω and ω_{LPF} transient responses. b) and c) Transient details.

In Fig. 63 it can be seen how ω reaches very fast the upper saturation bound $\omega_{\mathrm{SAT_{up}}}$ at the end of the time interval from $0.1950s$ to $0.1964s$, during which the FSM is at the S1 normal operation state. At this point ($t = 0.1964\ s$), $\omega = \omega_{\mathrm{SAT_{up}}}$ and the FSM state changes from S1 to S3. It is also at this moment that the value of ω_{LPF} is stored in an inner memory variable named $\omega_{\mathrm{LPF_{Mem}}}$ for later use. Then, $\omega_{\mathrm{LPF_{Mem}}}$ is defined as:

$$\omega_{LPF_{Mem}} = \omega_{LPF_{|\omega=\omega_{SAT_{up}}}}. \tag{45}$$

According to Fig. 63, $\omega_{\mathrm{LPF_{Mem}}} = 2\pi \cdot 50.019$ rad/s and $\omega_{\mathrm{SAT_{up}}} = \omega_{\mathrm{LPF_{Mem}}} + 2\pi = 314.27$rad/s.

Note that $\omega_{\mathrm{LPF_{Mem}}}$ is slightly away from the nominal value, which supposes that $\omega_{\mathrm{SAT_{up}}}$ is a little bit displaced from the ideal value of $2\pi \cdot 51$rad/s. However, the effect over the behavior of ω is negligible. Consequently, the fixed upper 51Hz and lower 49Hz saturation bounds employed in Fig. 63 have now been replaced by the new saturation variables $\mathrm{SAT_{up}}$ and $\mathrm{SAT_{down}}$ determined with (43)-(44), respectively, which are stored in inner variables. Moreover, the return of the FSM to normal operative condition state S1, defined in Fig. 56, for the transitions from S4 to S1 and from S5 to S1, has also been changed. Now, $\omega_{\mathrm{LPF_{Mem}}}$ is used instead of ω_n as center of the $\pm\Delta = \pm 0.02\%$ narrow band, i.e:

$$\omega_{LPF_{Mem}} - \Delta \leq \omega \leq \omega_{LPF_{Mem}} + \Delta. \tag{46}$$

Then, when ω is confined within these bounds, the $\mathrm{T_C}$ counter is started and the returning to S1 is decided if $\mathrm{T_C} \geq \mathrm{T_{C_{Max}}}$. The counter $\mathrm{T_C}$ is reset when ω leaves the band, which can happen due to an unexpected interference or to the presence of huge levels of harmonic distortion in the grid. Otherwise, in normal conditions ω progressively stabilizes, the counter $\mathrm{T_C}$ starts to count when condition (46) is met and the FSM returns to state S1, when $\mathrm{T_C} \geq \mathrm{T_{C_{Max}}}$. The value of $\mathrm{T_{C_{Max}}}$ can be set to adjust the time needed to return to normal operation state once the band 2Δ has been reached. At returning to state S1, the integrator of the LPF is initialized to the actual grid frequency, i.e. $\omega_{\mathrm{LPF}} = \omega$ (see Fig. 63.c), which supposes that the system is ready again for facing a new fault. Finally, Fig. 64, depicts the results obtained when considering three different scenarios, which have in common the occurrence of an 80% depth voltage sag at $t = 0.22\ s$. In the first scenario the grid frequency goes from $50Hz$ to $50.5Hz$ at $t = 0.15\ s$ (blue line), while it remains at $50Hz$ in the second scenario (red line) and goes down to $49.5Hz$ also at $t = 0.22\ s$ in the third scenario (green line). It can be seen how the FSM algorithm is able now to follow the step frequency changes and the voltage sags properly. Also, the FSM keeps a saturation band of $\pm 1Hz$ on the grid frequency.

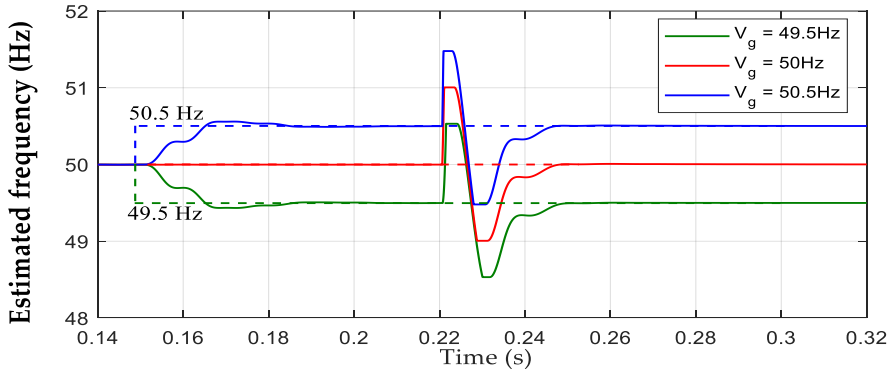

Fig. 64. Estimated frequency transient responses to 80% depth voltage sags produced at different grid frequency values. In blue: $\omega_g = 50.5$ Hz. In red: $\omega_g = 50\ Hz$. In green: $\omega_g = 49.5Hz$.

The same modification explained in this section for tracking the grid frequency changes allows the system to respond to faults happening in grid networks distorted by harmonics. Fig. 65 shows the behavior of ω and ω_{LPF} when an 80% depth voltage sag takes place at $t = 0.195\ s$ in a grid

distorted by a 5th harmonic with 3% amplitude.

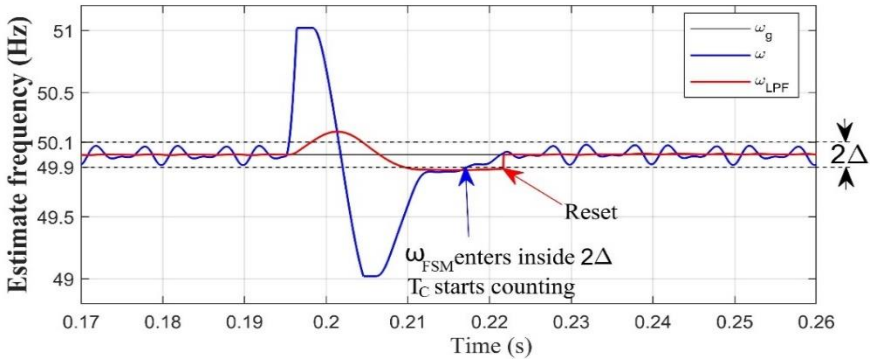

Fig. 65. ω and ω_{LPF} transient responses to an 80% depth voltage sag happening at $t = 0.195s$ for a grid voltage distorted by a 5th harmonic with 3% amplitude.

It can be seen in Fig. 65, how the FSM can work properly with the distorted grid voltage. The condition for being able to handle harmonic distortion is that the peak-to-peak amplitude Δ_ω of the distortion in the grid frequency should be less than the boundary width, i.e:

$$\Delta_\omega < 2\Delta \tag{47}$$

Then, the design of the value for the boundary 2Δ should take into consideration which is the maximum harmonic distortion that the FSM has to face. Also, a proper value for $T_{C_{Max}}$ should be chosen to determine a reasonable time for returning the state of the FSM to S1.

4.4. Swells faults and short transients' capability response

Fig. 66 depicts the response of the SOGI-FLL to voltage swell perturbations ranging from $1.1pu$ to $1.8pu$, with optimal parameters $\xi = 0.707$ and $\lambda = 0.28 \cdot \omega_n^2$ rad/s^2. This figure shows that swell perturbations have a different distortion impact than voltage sags had for the SOGI-FLL.

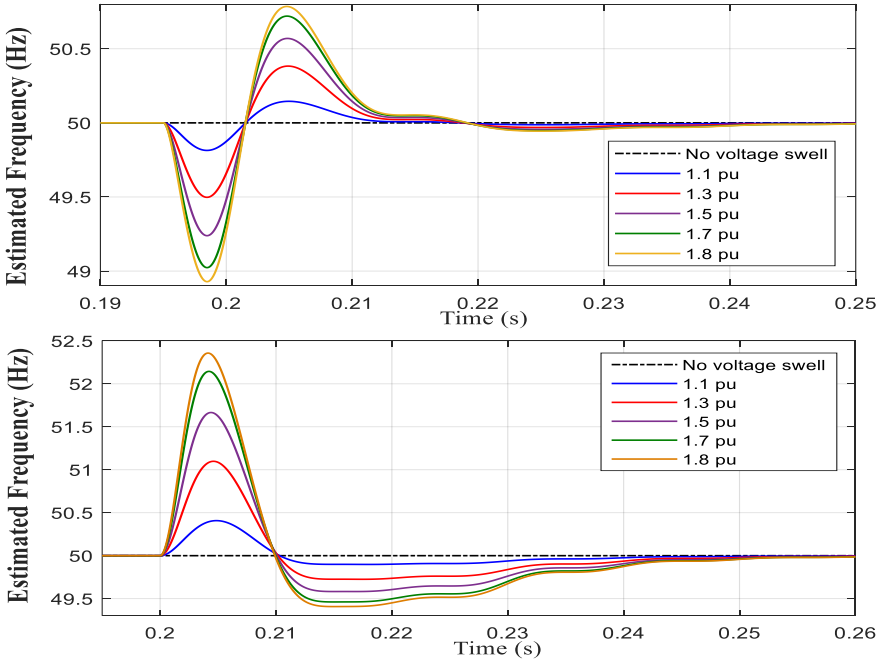

Fig. 66. Perturbations induced in the SOGI-FLL estimated frequency for different voltage swell levels. Upper: at non-zero input voltage. Lower: at zero crossing input voltage.

Notice in Fig. 66 that for swells happening at non-zero input-voltage moments (type-a) the perturbation almost don't reach the $\pm$ 1 Hz saturation bounds in almost all cases. So, for type-a swells the FSM will not act. However, for swells happening at zero voltage (type-b) the perturbations surpass the established $\pm$ 1 Hz bounds for fault levels ranging from 1.3 pu to 1.8 pu and the FSM can be applied to these cases for improving the response. As conclusion, for type-b swells, ranging from 1.3 pu to 1.8 pu, ω will reach SAT_{up} and the FSM can be applied in the same way that it was applied for voltage sags, provided the variable x defined in (48) is appropriately modified. For instance, a 1.3 pu swell can be treated by the FSM like a voltage sag of 30% depth if the variable x is set to $= 0.3\ pu$. In the same way, a 1.8 pu swell can be treated by the FSM as a sag having $x = 0.8$, or 80% depth. Therefore, the FSM can be indistinctly applied to a voltage sags and swells by using the following relation instead of (41):

$$x = 1 - abs(A_y - A_{pu}). \tag{48}$$

where $A_y = 0$ holds for voltage sags and $A_y = 2$ for voltage swells and $abs(\,)$ represents the absolute value function. The block diagram depicted in Fig. 67 clarifies well this issue and will be used in the algorithm to differentiate a voltage sag from a voltage swell.

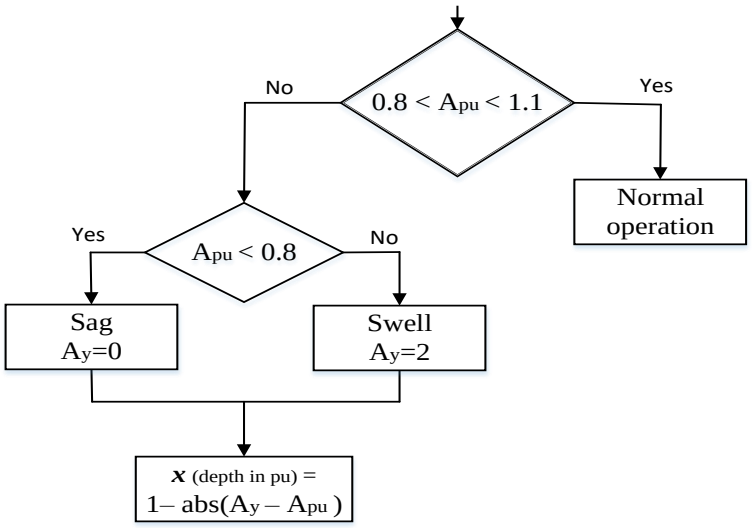

Fig. 67. Algorithm used for differentiating voltage sags from voltage swells.

Then, the FSM from now on incorporates the algorithm of Fig. 67 and uses equation (48) to respond indistinctively to voltage sags or swells. Fig. 68 illustrates the response of the SOGI-FLL-FSM to several voltage swells (subplots 68.a and 68.b) and sags (subplots 68.c and 68.d) with different durations. Fault events in subplots 68.a and 68.c extend for 4 $cycles$, while those in subplots 68.b and 68.d do for 2 $cycles$, which correspond to the shorter event duration that don't result in overlapped transients at the beginning and at the end of the faults. As a fault-transient, it is considered here the event of a voltage swell, or sag, and the recovery to nominal grid voltage in short time. In subplots 68.a and 68.b the swell series till 1.8 pu and then return to 1 pu. In subplots 68.c and 68.d the sags go down to 0.2 pu and then return to 1 pu. Notice in these figures that the

FSM can respond well for both type of faults and that can improve the capability to respond to short time-duration transients.

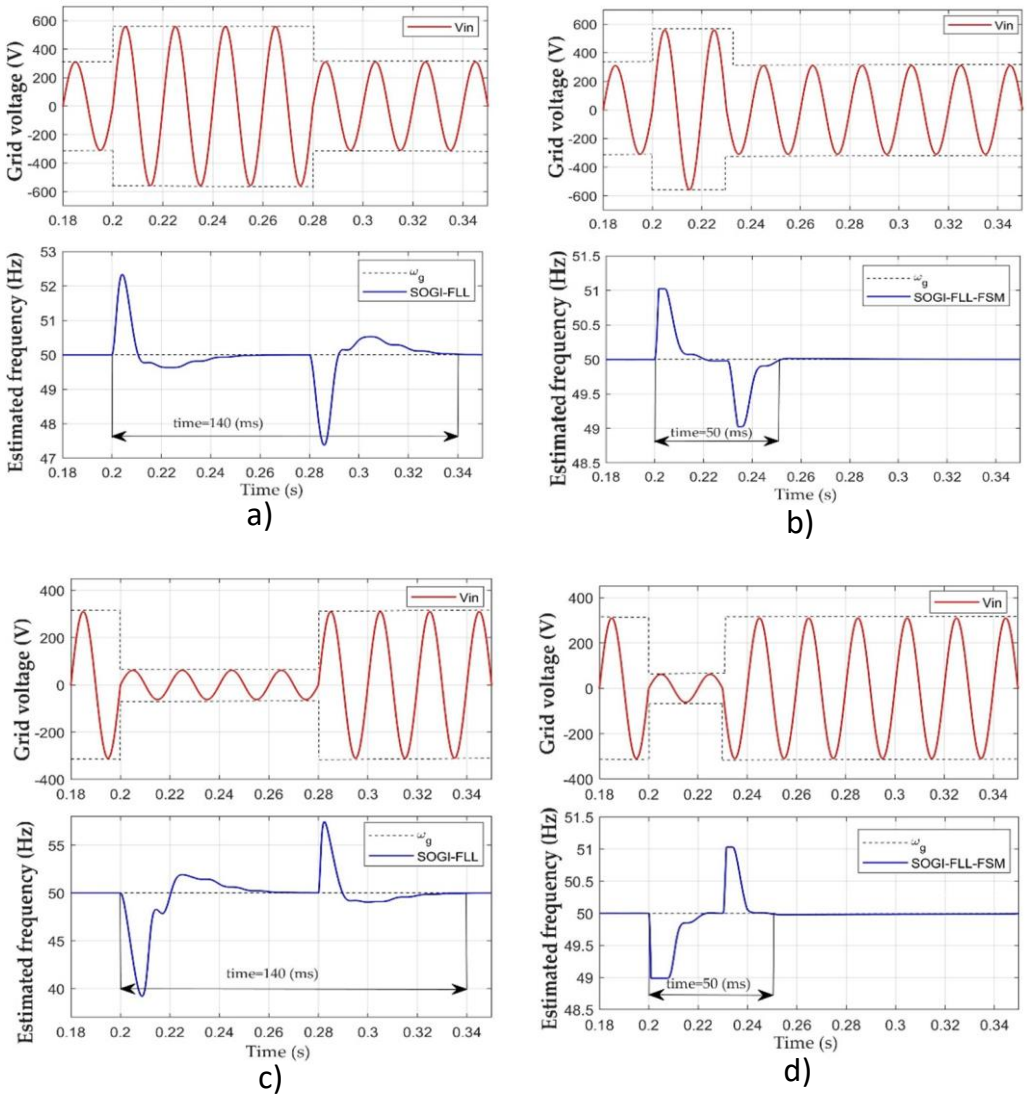

Fig. 68. Response of the SOGI-FLL-FSM to short duration voltage swells and sags. Subplots 68.a and 68.b: 1.8 pu swells at 0.2 s, with 4 and 2 $cycles$ duration, respectively. Subplots 68.c and 68.d: 0.2 pu sags at 0.2 s, with 4 and 2 $cycles$ duration, respectively.

Finally, the SOGI-FLL-FSM response to the same voltage sag than in Fig. 68.d is shown in Fig. 69, when the grid voltage is affected by a 5th-harmonic distortion with 4% amplitude. Notice in this figure that the response is similar to that achieved in Fig. 68.d but, in this case, the harmonic distortion is reflected in the estimated frequency response.

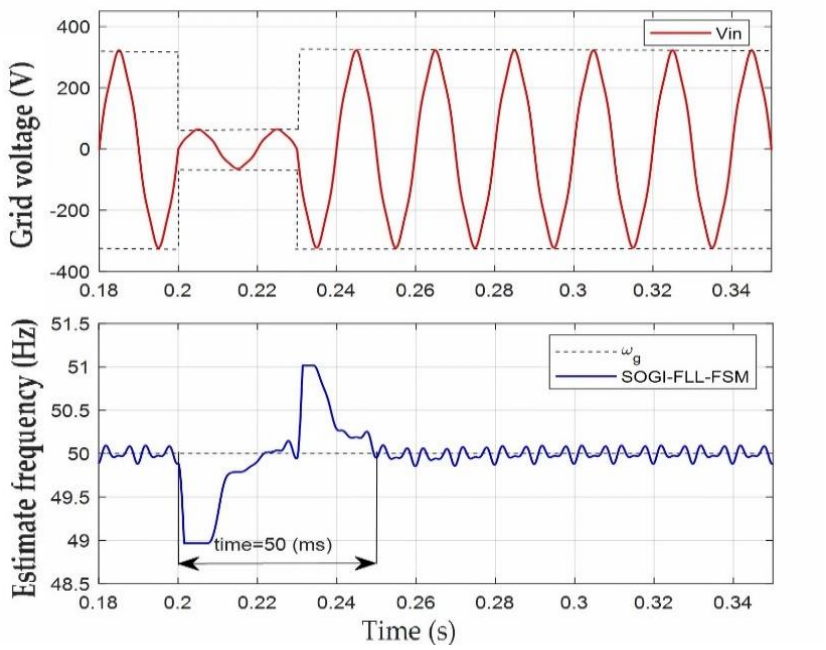

Fig. 69. Response of the SOGI-FLL-FSM to a 2 $cycles$ 0.2 pu voltage sag at 0.2 s in presence of a 5th-harmonic with 4% amplitude in the grid voltage.

4.5. SOGI-FLL-EbA using e, |e| and $avg(|e|)$

The most effective approach for reducing the perturbation in the FLL estimated frequency is by means of using directly the error signal of the SOGI filter, because it receives directly the impact of the fault through the input voltage, i.e., $e = v_g - v_d$. In thesis, a proposal is made using the error signal, the absolute value of the error signal, $|e|$, and a low-pass filtering of $|e|$, noted as $LPF(|e|)$ and also as $avg(|e|)$. The proposal consists in an algorithm that uses these variables as inputs and that provides a proper value of ξ and λ to the SOGI-FLL for facing the fault and reduce the impact of the perturbation. This proposal is defined first for voltage sags and after is also applied to voltage swells. The block diagram that schematizes this proposal can be seen in Fig. 70.

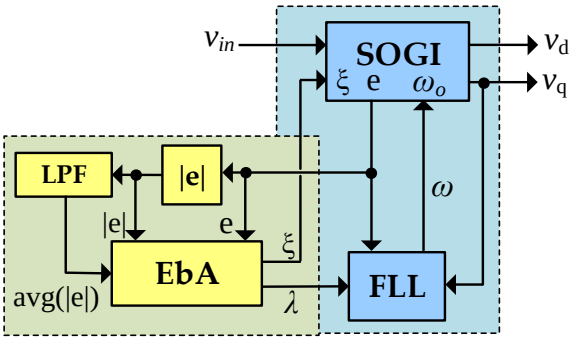

Fig. 70. SOGI-FLL-EbA proposal using e, $|e|$ and $avg(|e|)$ for reducing the impact of voltage sags and swells in the estimated frequency.

The algorithm is depicted in Fig. 71 and is defined using only three states, named as S1, S2 and S3. From now on, the proposal will be named as SOGI-FLL "Error-based Algorithm", SOGI-FLL-EbA. In the algorithm, S1 means normal operation. In this case, the SOGI-FLL-EbA operates with nominal gains (ξ_N, λ_N). This gains can be the pair (ξ_1, λ_1) or (ξ_2, λ_2), but the pair (ξ_1, λ_1) are used

mainly in this thesis. Then, at a fault event, $|e|$ spikes such as a sharp impulsive transient response. The error $|e|$ is compared to a given threshold e_γ and, if $|e| > e_\gamma$, the algorithm goes to state S2 were the SOGI-FLL-EbA runs with different gains named as (ξ_F, λ_F). These gains had been designed by a series of trial-and-error simulations for achieving a proper transient response and reduce the impact of the perturbation. The threshold e_γ is designed to be able respond to a frequency step change of $\pm 2\ Hz$ and to pass a harmonic distortion that can reach a 3% THD. The main objective had consisted into reducing the perturbation size to less than $2\ Hz$ for the case of $0.2\ pu$, i.e., an 80% depth. To this purpose, the FLL gain, λ_F, has been strongly reduced.

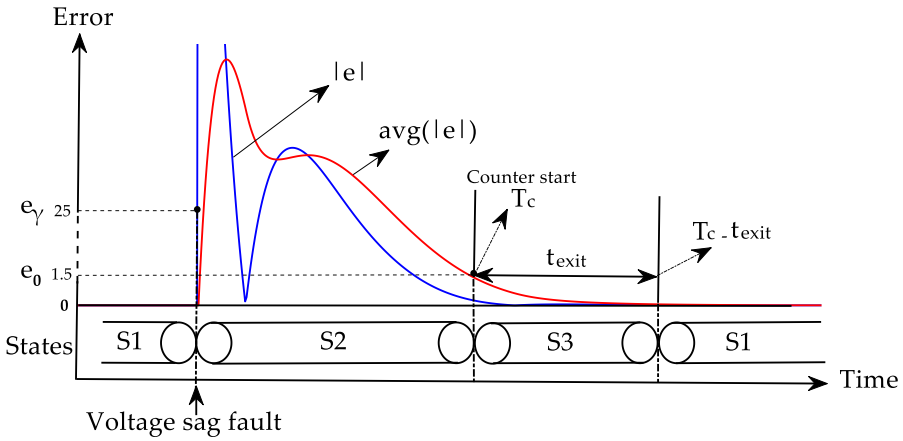

Fig. 71. SOGI-FLL-EbA using e, $|e|$ and $avg(|e|)$ signals for improving the frequency response in face of voltage sags and swells.

At this stage, the average input, $avg(|e|)$ is used for transitioning to S3. This average is obtained by using a LPF with a suitable cutoff frequency, ω_c, with the aim of filtering $|e|$ and generate an energy-like function for giving an indication of when the perturbation has passed over. The transitory of $avg(|e|)$ will consists in an impulsive function, see Fig. 71, in red, that exponentially decays to zero, which, when is close to zero, means that the perturbation is over. Therefore, the algorithm goes to S3 only when $avg(|e|)$ is a given threshold, $avg(|e|) < e_o$. Finally, a counter timer T_c is started for giving a specific exit-time, t_{exit}. This counter helps to set a specific time delay to be performed before returning to state S1, in order to ensure a smooth returning to normal state. The exit-time is designed to cover all the different voltage sag depths. When the condition $T_c > t_{exit}$ meets, the algorithm returns back to state S1 and the SOGI-FLL-EbA operates again with (ξ_N, λ_N).

And, the same algorithm can be applied to voltage swells using e to identify a swell from a voltage sag. As $e = v_g - v_d$, at the event of a fault, if $e < 0$ means that the fault consists in a voltage sag and $e > 0$ in a voltage swell. The gains (ξ_F, λ_F), threshold e_o and exit-time t_{exit} are different for voltage sags and swells and the values are depicted in Table 6.

Table 6. SOGI-FLL-EbA parameters responding to voltage sags and swells.

Parameter	Mp	State	
		S1	S2–S3
(ξ_1, λ_1)	4.32%	$(0.707, 0.5\omega_n^2)$	$(0.82, 0.06\omega_n^2)$
(ξ_2, λ_2)	0%	$(0.707, 0.25\omega_n^2)$	$(0.82, 0.16\omega_n^2)$
Parameter		**Value**	
Fault-type		**Sag**	**Swell**
e_γ		25 V	25 V
e_o		1.5 V	7 V
t_{exit}		8.5 ms	12 ms

4.6. Analysis of SOGI-FLL-EbA for voltage sag, swell perturbation

In this section the simulation perform for voltage sag and swell perturbation in SOGI-FLL-EbA method and compare result by SOGI-FLL. Figs. 72.a and 72.b depict the transient response of the SOGI-FLL and SOGI-FLL-EbA for a 0.2 pu voltage sag and 1.8 pu voltage swell, respectively. The faults happen at time 0.205 s. Notice how the perturbation in both cases had been reduced considerably, above 1Hz peak-to-peak.

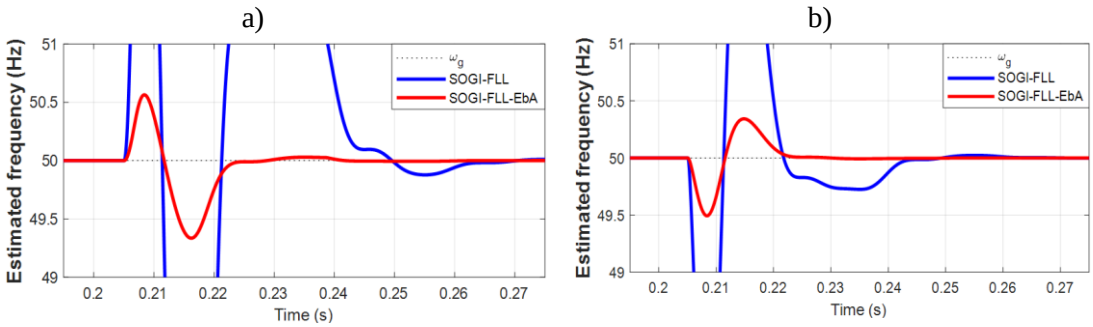

Fig. 72. SOGI-FLL and SOGI-FLL-EbA estimated frequency transient responses to 0.2 pu voltage sag and 1.8 pu voltage swell at 0.205s, respectively.

The value choosen for the threshold e_γ has been designed to be able to accommodate a frequency step change of $\pm$2Hz and including a 3% THD harmonic distortion. Fig. 73.a depicts the transient response of the SOGI-FLL-EbA for a 2Hz frequency step change at 0.2s. Fig. 73.b shows the same transient response with a 3rd harmonic with 3% amplitude from nominal. Notice how the threshold allows the SOGI-FLL-EbA to respond to these perturbations, which do not triggers the proposed algorithm.

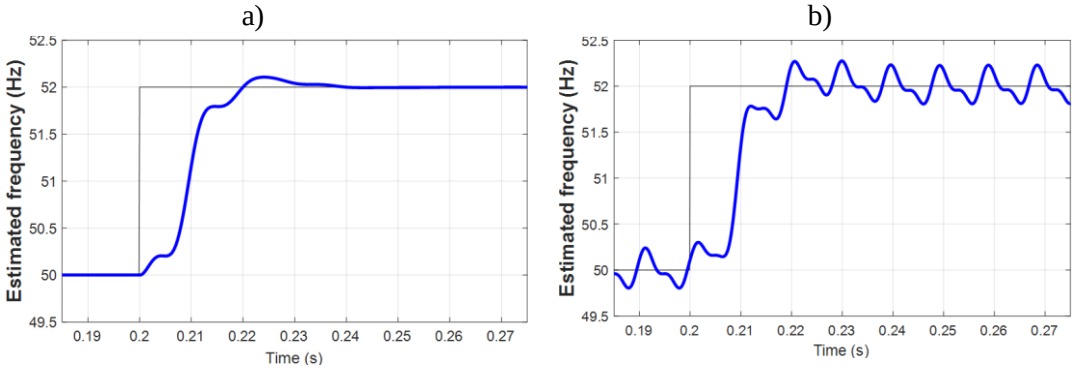

Fig. 73. Transient responses of the SOGI-FLL-EbA to a frequency step perturbation of 2Hz. a) without harmonic distortion. b) with a 3rd harmonic and 3% amplitude voltage regarding nominal.

Figs. 74 and 75 depict the transient response of the SOGI-FLL and SOGI-FLL-EbA to voltage sags and swells with diferent durations. As fault transient, we consider here the event of a voltage sag or swell and recovery to nominal grid voltage in a short time. Fault events of Fig. 74.a extend for three and three quarters cycles while those in Fig. 75.a do so for three cycles and half. These responses show that the proposed algorithm reduces the impact of the perturbacion and that allows a faster transient response. For this reason, Figs. 74.b and 75.b show the results for shorter fault lengths and have a constrast.

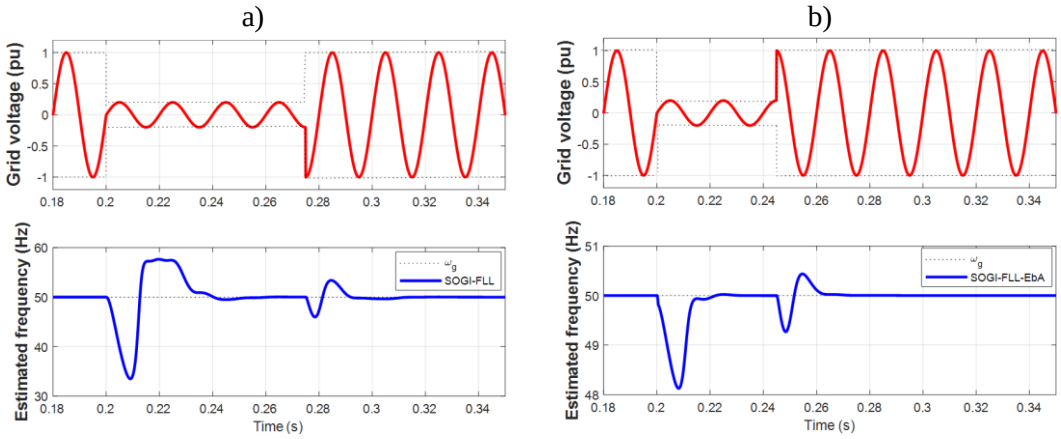

Fig. 74. Transient response of the SOGI-FLL and SOGI-FLL-EbA to short-duration voltage sags. a) SOGI-FLL response to a 0.2 pu voltage sag at $0.2s$ with three cycles and three quarters of duration. b) SOGI-FLL-EbA response to 0.2 pu voltage sag at $0.2s$ with two and half cycles of duration.

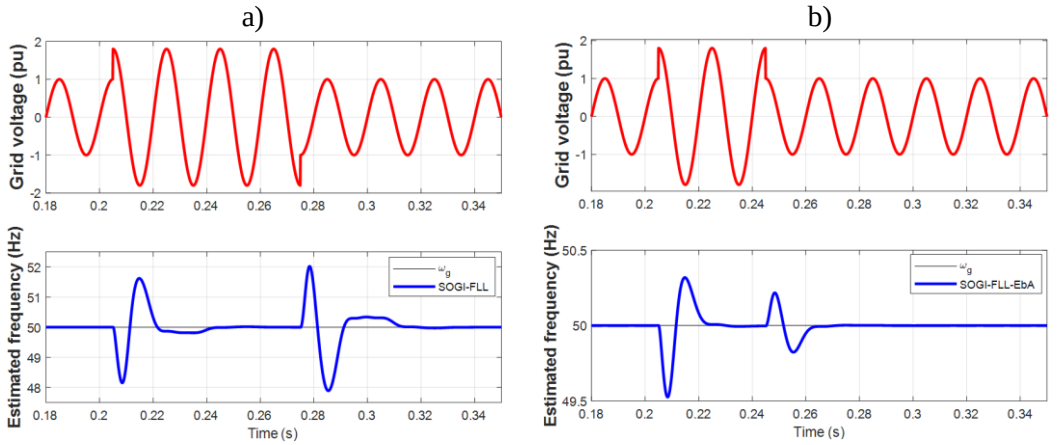

Fig. 75. Transient response of the SOGI-FLL and SOGI-FLL-EbA to short-duration voltage swell. a) SOGI-FLL response to a 1.8 pu voltage swell at $0.205s$ with three and half cycles of duration. b) SOGI-FLL-EbA response to 1.8 pu voltage swell at 0.205 s with one and half cycles of duration.

Also, the grid voltage and the SOGI-FLL and SOGI-FLL-EbA had been implemented in a real-time HIL Typhoon 402 and HIL DSP100 platforms and the responses being captured in the typhoon SCADA panel [81].

The SOGI-FLL and SOGI-FLL-EbA had been discretized with a third-order discretization method

$$\frac{1}{s} \leftrightarrow \frac{T_s}{12} \frac{5z^{-3} - 16z^{-2} + 23z^{-1}}{1 - z^1}, \tag{49}$$

meanwhile the integrator of the FLL has been discretized using a using a Backward Euler method:

$$\frac{1}{s} \leftrightarrow \frac{T_s}{1 - z^1}, \tag{50}$$

being Ts the Sample Time of 100µs, consistent with the $10kHz$ frequency.

Fig. 76 shows the HIL results for the SOGI-FLL and SOGI-FLL-EbA to a periodic voltage sag fault transient that goes from $1pu$ to $0.2\ pu$ and then return back to $1\ pu$. The voltage sag go down to $0.2\ pu$ and then return to $1\ pu$. In a similar way, Fig. 77 depicts the transient results for a voltage swell that goes from $1\ pu$ to $1.8\ pu$ and back to $1\ pu$. As is the Simulink simulations, these HIL results show how the SOGI-FLL-EbA noticeably reduces the impact of the perturbacion, allowing a faster response and respond to shoter duration transient faults.

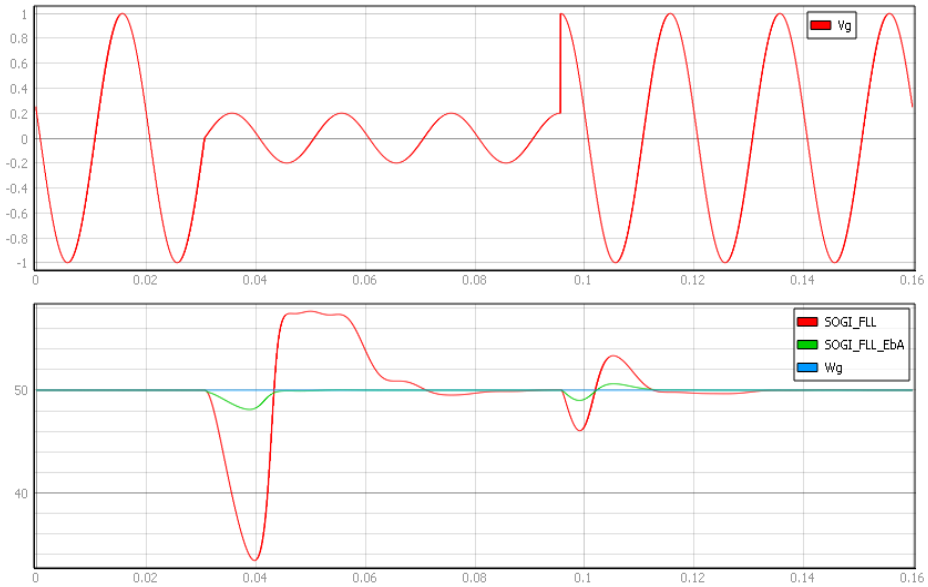

Fig. 76. HIL results for the SOGI-FLL and SOGI-FLL-EbA to short-duration voltage sag. up) Grid voltage sag fault going from $1\ pu$ to $0.2\ pu$ and going back to $1\ pu$. down) SOGI-FLL (red)and SOGI-FLL-EbA (green) estimated frequency response to the voltage sag in Hz.

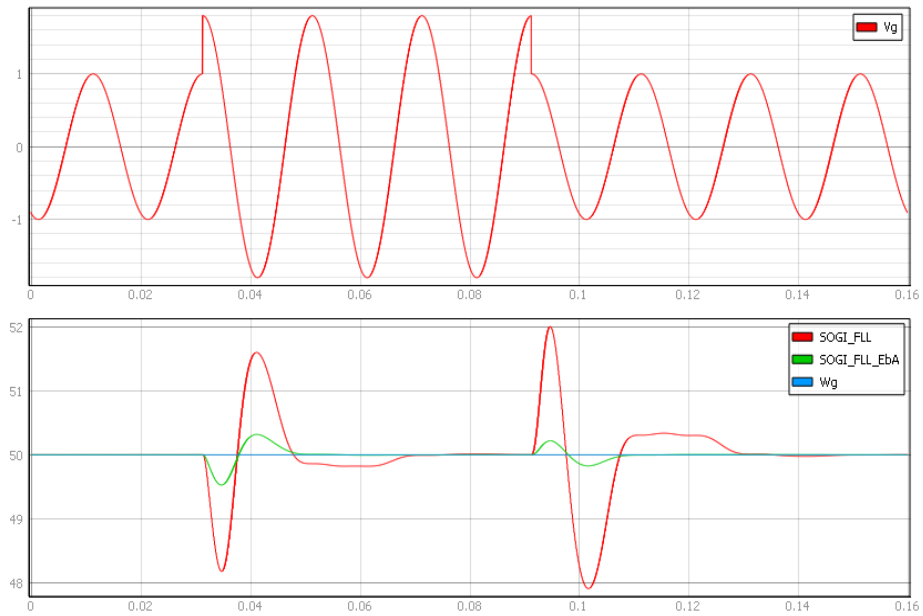

Fig. 77. HIL results for the SOGI-FLL and SOGI-FLL-EbA to short-duration voltage swell. up) Grid voltage swell fault going from 1 pu to 1.8 pu and going back to 1 pu. down) SOGI-FLL (red) and SOGI-FLL-EbA (green) estimated frequency response to the voltage sag in Hz.

Moreover, the peak-to-peak size of the perturbation had been measured for different depth and height sizes to assess the reduction in the perturbation achieved by the proposal using Matlab/Simulink. Fig. 78 depicts these measurements that show that the algorithm functions effectively in all the ranges defined for sags and swells.

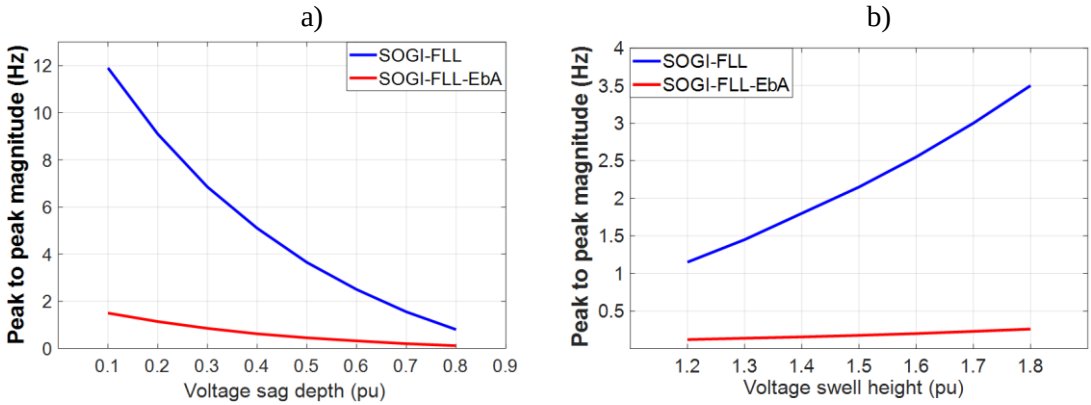

Fig. 78. Measured peak-to-peak maximum amplitude distortion in Hz for different voltage sags and swells. a)For sags with depths ranging from 0.1 pu to 0.8 pu.b) For swells with heights ranging from 1.2 pu to 1.8 pu.

5. Error-based-Algorithm applied to the SOGI-PLL

The Error-based-Algorithm defined before can be applied to the SOGI-PLL, so it will be the "SOGI-PLL-EbA" for improving the response fo this technique to woltage sags and swells. In this case, the error of the SOGI is used to tune the k_p and k_i gains of the SOGI-PLL to minimize the impact of the perturbation. Fig. 79 depicts the block diagram of this proposal.

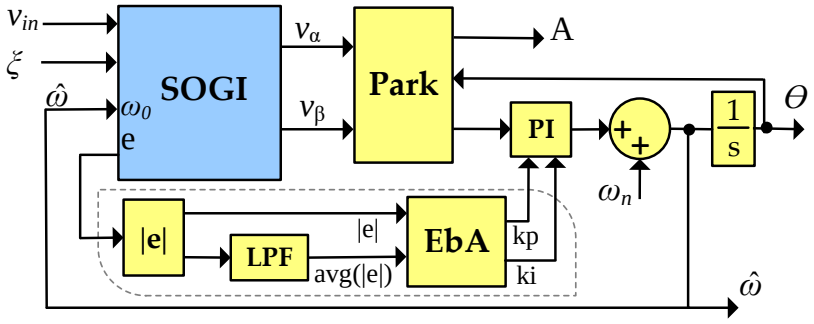

Fig. 79. Block diagram of the SOGI-PLL-EbA.

A simple application for the SOGI-PLL is that the algorithm resets k_p and k_i to zero in order to frozen the PI part of the PLL, trying to keep them unaffected by the fault. The PI remains frozen during the fault and returns to nominal gains when the fault is over. This proposal is valid for voltage sags and swells. The algorithm threshold e_γ is designed to be able respond to a frequency step change of $\pm 2\ Hz$ and to pass a harmonic distortion that can reach a 3% THD.

Since the action is taken over the PI parameters, in this case there is no need to differentiate between voltage sag and swells. Therefore, for the SOGI-PLL the algorithm it is a bit simpler. The values for the PI gains, thresholds e_γ and e_o, and exit-time t_{exit} are depicted in Table 7.

Table 7. SOGI-PLL-EbA parameters responding to voltage sags and swells.

Parameter	State	
	S1	**S2–S3**
k_p	0.24	0
k_i	10	0
e_γ	22 V	
e_o	11 V	
t_{exit}	18 ms	

Simulations had been performed for voltage sags and swells in the SOGI-PLL and SOGI-PLL-EbA. Figs. 80.a and 80.b depict the transient response for a 0.2 pu voltage sag and 1.8 pu voltage swell, respectively. The faults happen at time $0.3s$. Notice how the perturbation in both cases had been almost removed, proving that method is more effective for the SOGI-PLL. Figs. 81.a and 81.b depict a detail of the transients in which can be seen that the transient has been reduced drastically, but not removed. Furthermore, Figs. 82.a and 82.b show the estimated amplitude voltage transient in which can be seen that the method has improved the transient response. Figs. 83.a and 83.b show the transient responses to a frequency step perturbation of $2Hz$ at $t = 0.3s$. Fig. 83.a depicts the transient without harmonic distortion and Fig. 83.b with a 3rd harmonic with a 3% amplitude from nominal, respectively.

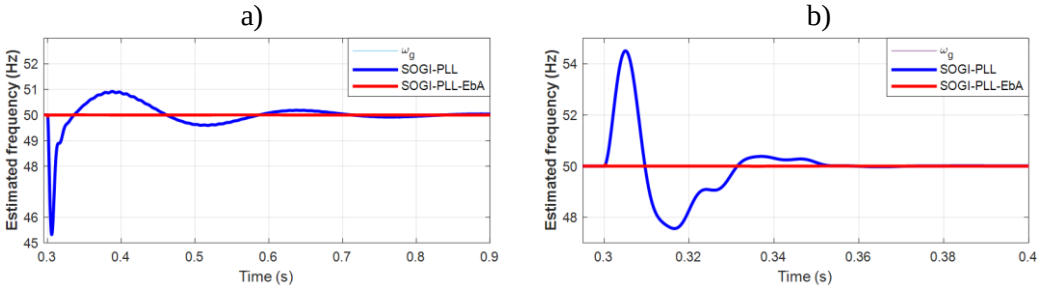

Fig. 80. SOGI-PLL and SOGI-PLL-EbA estimated frequency transient responses to 0.2 pu voltage sag and 1.8 pu voltage swell at 0.3s, respectively.

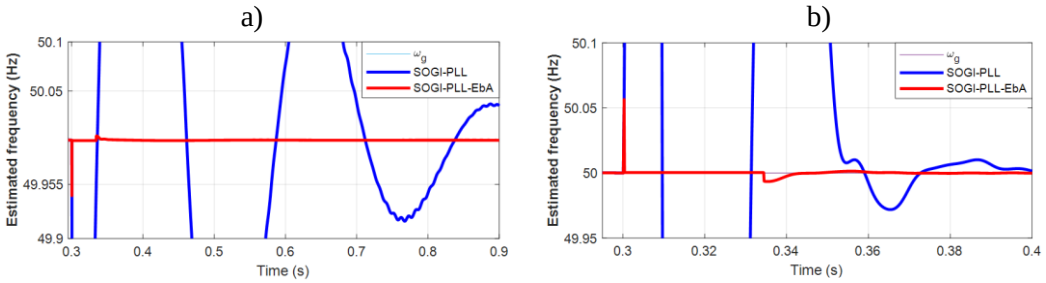

Fig. 81. Detail of the SOGI-PLL and SOGI-PLL-EbA estimated frequency transient responses to 0.2 pu voltage sag and 1.8 pu voltage swell at 0.3s, respectively.

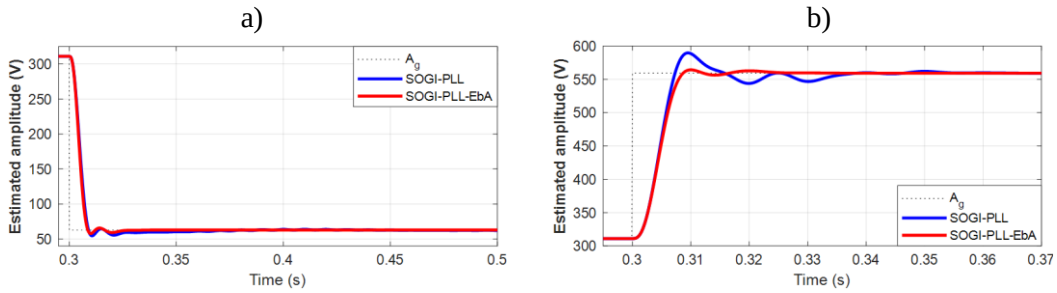

Fig. 82. SOGI-PLL and SOGI-PLL-EbA estimated amplitude voltage transient responses to 0.2 pu voltage sag and 1.8 pu voltage swell at 0.3s, respectively.

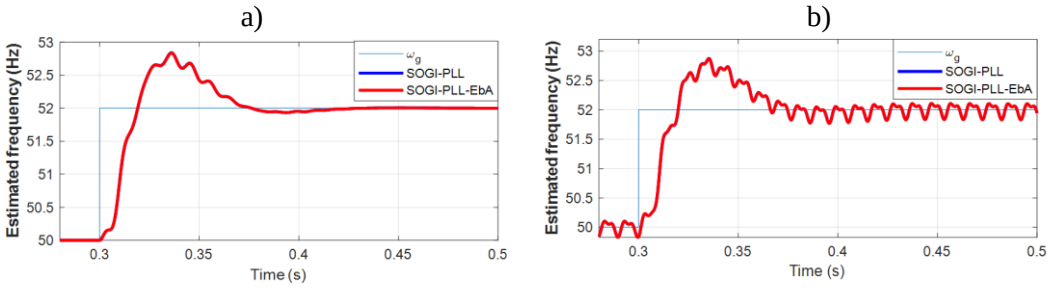

Fig. 83. Transient responses of the SOGI-PLL and SOGI-PLL-EbA to a frequency step perturbation of 2Hz. a) without harmonic distortion. b) with a 3rd harmonic and 3% amplitude voltage regarding nominal.

Likewise for the SOGI-FLL case, Figs. 84 to 85 depict the transient response of the SOGI-PLL and SOGI-PLL-EbA to voltage sags and swells of diferent durations involved in a fault transient. Fig. 84 is a fault transient that starts at $t = 0.3s$ and ends at $t = 0.8s$. These time duration is intended toshow how long it is the response of the SOGI-PLL and that the response of the SOGI-PLL-EbA remains unaffected. The fault goes from $1pu$ to $0.1pu$ and then back to $1pu$. Notice that the estimated amplitude it is also shown in the figure and the that, in this regard, the SOGI-PLL-EbA exhibits a better transient responses.

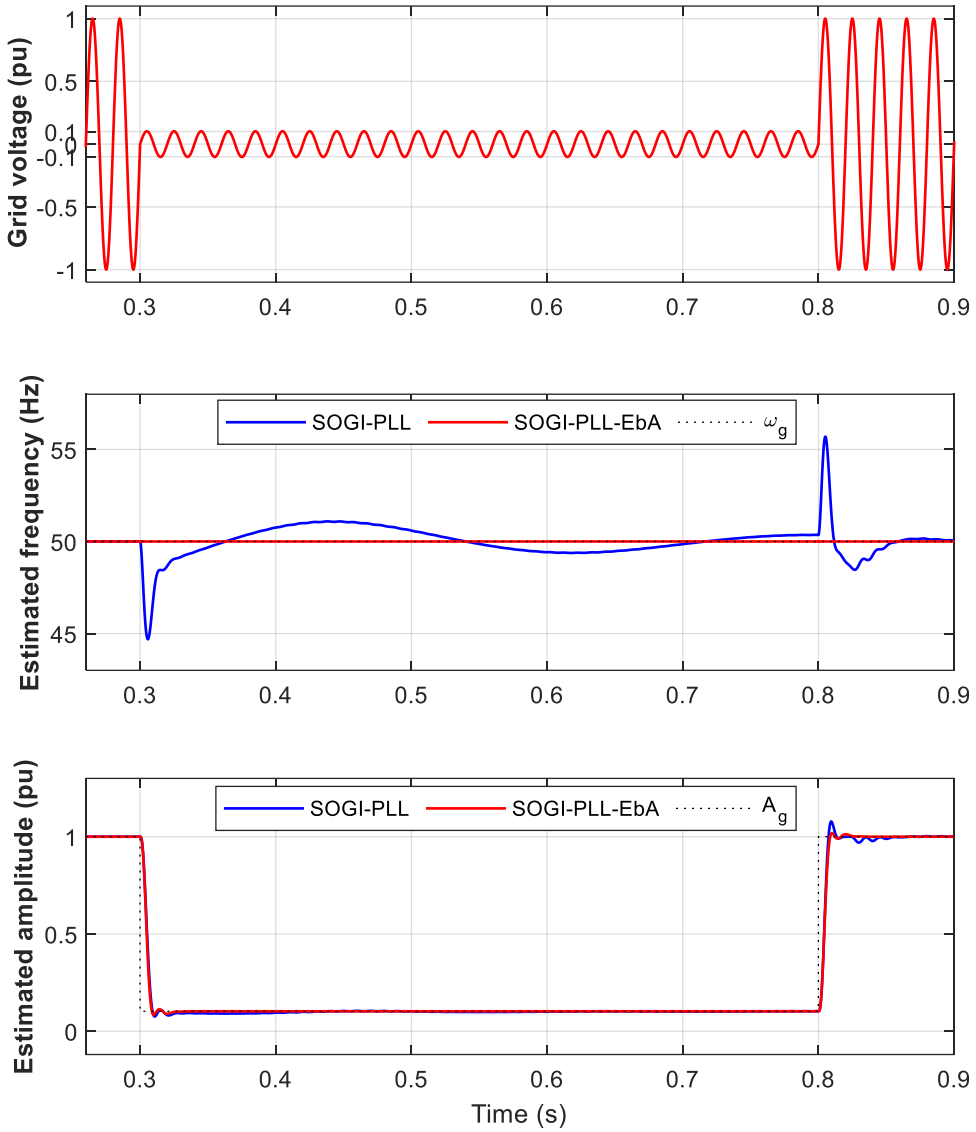

Fig. 84. Transient response of the SOGI-PLL and SOGI-PLL-EbA to a voltage sag from $1pu$ to $0.1pu$ at $t = 0.3s$ and then returns to $1pu$ at $t = 0.8s$.

Fig. 85 shows a shorter transient fault than the previous figure. It starts at $\boldsymbol{t = 0.3s}$ and ends at $\boldsymbol{t = 0.4s}$. The purpose of this figure is to show how the SOGI-PLL-EbA has a better capability to respond properly to shorter fault transients.

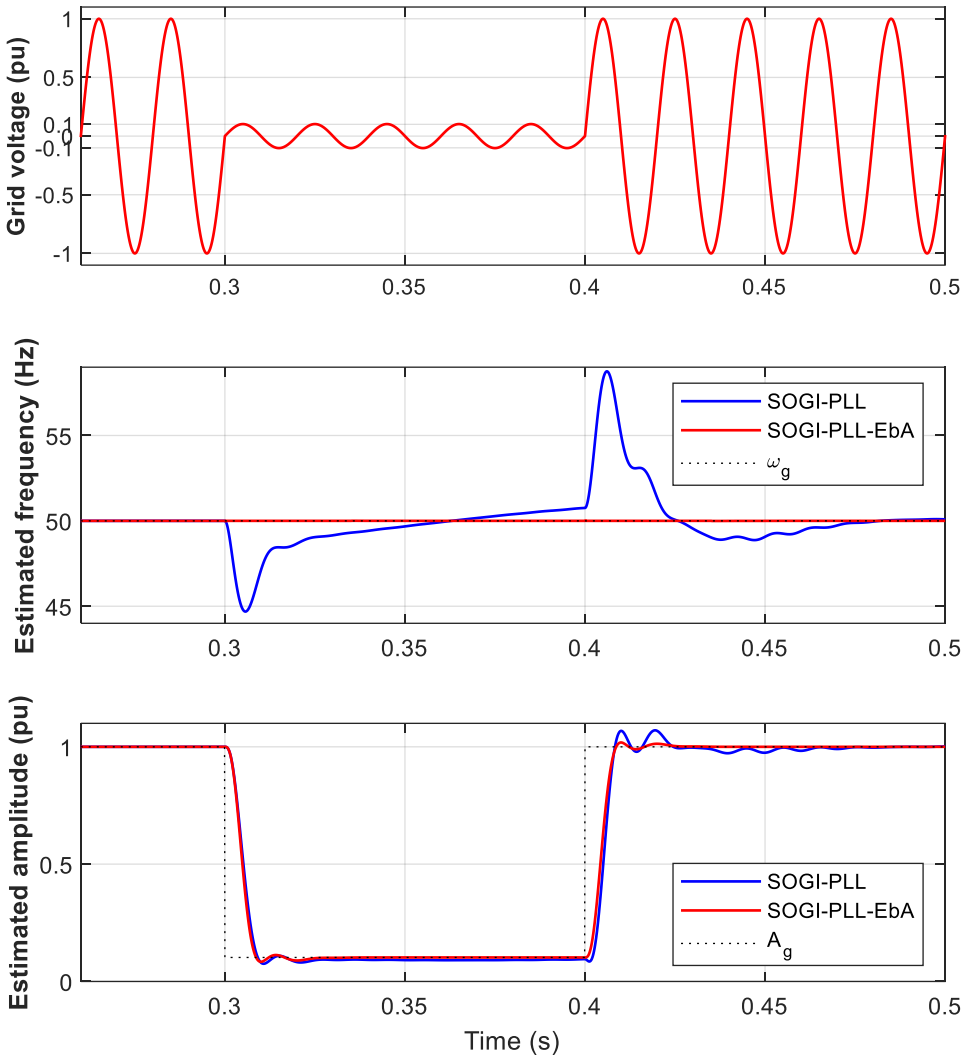

Fig. 85. Transient response of the SOGI-PLL and SOGI-PLL-EbA to a voltage sag from $1pu$ to $0.1pu$ at $t = 0.3s$ and then returns to $1pu$ at $t = 0.4s$.

Finally, Fig. 86 shows the response of the SOGI-PLL and SOGI-PLL-EbA to a fault transient that starts at $\boldsymbol{t = 0.3s}$ and ends at $\boldsymbol{t = 0.35s}$, going from $\boldsymbol{1pu}$ to $\boldsymbol{1.8pu}$. Notice how as in the previous case the SOGI-PLL-EbA respond well to the fault. In view on this result can be inferred that the SOGI-PLL-EbA could respond to a voltage flicker problem in the grid.

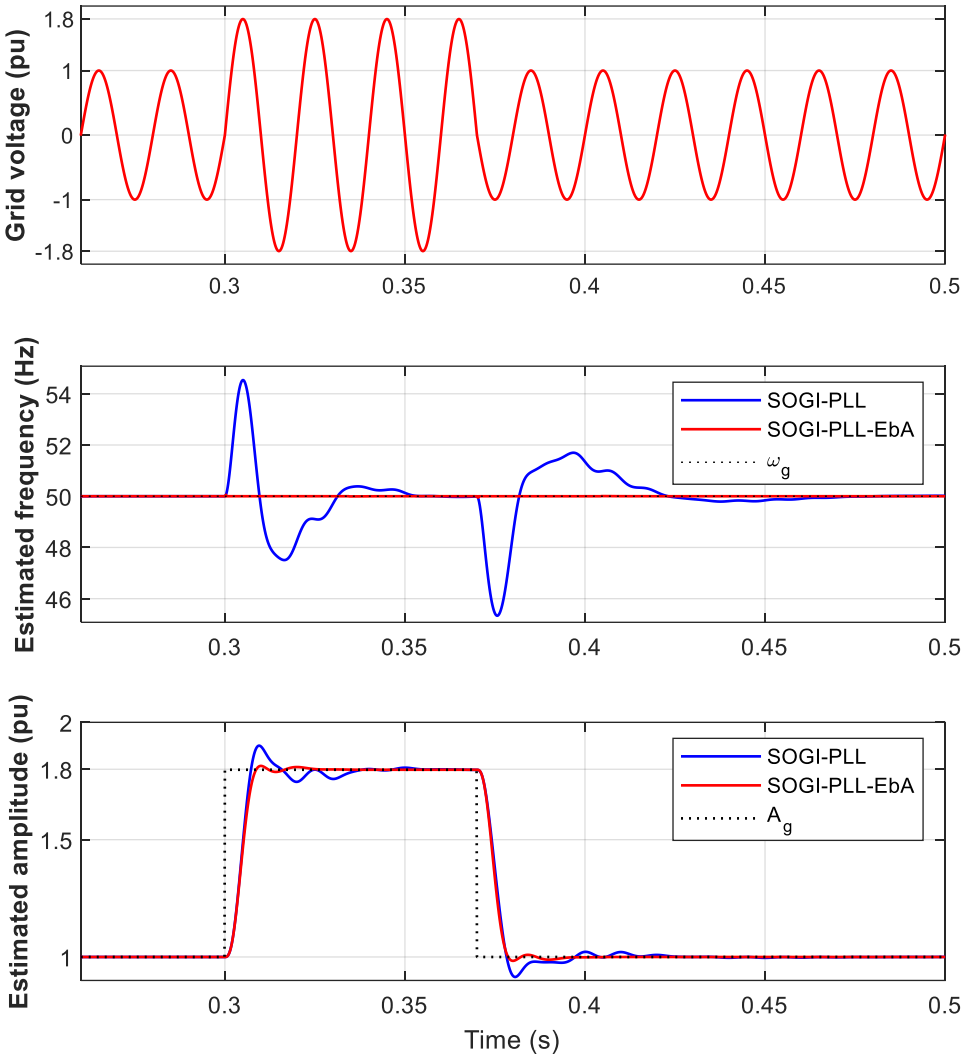

Fig. 86. Transient response of the SOGI-PLL and SOGI-PLL-EbA to a voltage swell from $1pu$ to $1.8pu$ at $t = 0.3s$ and then returns to 1pu at $t = 0.35s$.

6. Contribution and Conclusions

This work has been devoted to the analysis of the response of different grid monitoring methods to different problems in the grid network and simulations have been shown to see the magnitude of the induced perturbation in the amplitude voltage and frequency estimates. From this analysis and the literature review, the thesis has been focused into trying to improve the response to voltage sags of the SOGI-FLL structure in particular. The approaches made to face this problem had been applied also to voltage swells, since it has been concluded that they affected to the structure in a similar way than for voltages sags. Then, the research has been addressed to mitigate the impact of these two problems.

A first approach has been conducted using a FSM in the SOGI-FLL for defining different gains during the response profile of the estimated frequency. This approach had reduced the impact of voltage sags and swells but at expense of a complex structure that need to define different gains depending the depth level of the voltage sag and to be able to follow the frequency variations of the grid frequency. However, this approach has been the base to define a new approach based on the use of the error signal of the SOGI structure. This change in the point of view, allow to face the response action to the fault in a faster, simpler and effective manner. The application of this error-based approach to the SOGI-FLL has been much satisfactory, leading to a better results.
Finally, it has been found that this approach has could been applied with few modifications in its conception to the SOGI-PLL with good results that probe that could be a candidate to solve this problem also for this structure.

7. Future work

The approach developed in this thesis suggest us that it could be applied also for the SRF-PLL and the EPLL in future research, because voltage sags and swells have an important perturbation impact in all the structures.

8. Outcome

5.1. Paper Nr. 1: “A New SOGI-FLL Grid Frequency Monitoring with a Finite State Machine Approach for Better Response in Face of Voltage Sag and Swell Faults”

5.2. Paper Nr. 2: “SOGI-FLL Grid Frequency Monitoring with an Error-Based Algorithm for a Better Response in Face of Voltage Sag and Swell Faults”

9. References

[1]. François Martzloff National Institute of Standards and Technology Reprinted from Proceedings, PQA'97 Europe, Stockholm, 1997.

[2]. Golestan, S.; Guerrero, J.M.; Vasquez, J.C.; Abusorrah, A.M.; Al-Turki, Y.A. Standard SOGI-FLL and Its Close Variants: Precise Modeling in LTP Framework and Determining Stability Region/Robustness Metrics. IEEE Trans. Power Electron. 2020, 36, 409–422.

[3]. C. M. Hackl and M. Landerer, "Modified Second-Order Generalized Integrators With Modified Frequency Locked Loop for Fast Harmonics Estimation of Distorted Single-Phase Signals," in IEEE Transactions on Power Electronics, vol. 35, no. 3, pp. 3298-3309, March 2020, doi: 10.1109/TPEL.2019.2932790.

[4]. "IEEE Recommended Practice for Powering and Grounding Electronic Equipment - Redline," in IEEE Std 1100-2005 (Revision of IEEE Std 1100-1999) - Redline , vol., no., pp.1-703, 24 May 2006.

[5]. International Electrotechnical Commission, Geneva, Switzerland, www.iec.ch.

[6]. Fourier, J.B.J. (1822) Th´ eorie Analytique de la Chaleur, Paris.

[7]. A. E. Emanuel, "Harmonic in the Early Years of Electrical Engineering: A Brief Review of Events, People and Documents", IEEE, ICHQP, Oct 2000.

[8]. J. Lundquist, On Harmonic Distortion in Power Systems, Chalmers University of Technology, Goteborg, Sweden 2001.

[9]. R. Arseneau, G. T. Heydt, M. J. Kempker, "Application of IEEE Standard 519-1992 Harmonic Limits for Revenue Billing Meters", IEEE PES Winter Meeting, Baltimore, MD, January 21-25, 1996.

[10]. E. F. Fuchs, et al, "Sensitivity of Electrical Appliances to Harmonics and Fractional Harmonics of the Power Systems Voltage. Part II: Television Sets, Induction Watt-hour Meters and Universal Machines", IEEE PES Winter Meeting, New York, NY, February 2-7, 1986.18.

[11]. D. E. Rice, "Adjustable Speed Drive and Power Rectifier Harmonics, Their Effect on The Power Systems Components", IEEE IAS Annual Meeting, New York, NY, 1985.

[12]. W. Xu, et al, "A Three-phase Converter Model for Harmonic Analysis of HVDC Systems", IEEE PES Winter Meeting, New York, NY, January 30 – February 3, 1994.

[13]. E. F. Fuchs, et al, "Sensitivity of Electrical Appliances to Harmonics and Fractional Harmonics of the Power Systems Voltage. Part I: Transformers and Induction Machines", IEEE PES Winter Meeting, New York, NY, February 2-7, 1986.

[14]. M. Castilla, J. Miret, A. Camacho, J. Matas and L. G. de Vicuna, "Reduction of Current Harmonic Distortion in Three-Phase Grid-Connected Photovoltaic Inverters via Resonant Current Control," in IEEE Transactions on Industrial Electronics, vol. 60, no. 4, pp. 1464-1472, April 2013.

[15]. T. S. Key, J-S. Lai, "Costs and benefits of Harmonic Current Reduction for Switch Mode Power Supplies in a Commercial Office Building", IEEE IAS annual meeting, Lake Buena Vista, FL, October 8-12, 1995.

[16]. A. Omar, Ad. El-Rfaey, M. Moussa, and Y.G. Dessouky, "Review of DC Offset Compensation Techniques for Grid Connected Inverters," Int. Journ. of Power Electronics and Drive System (IJPEDS), vol. 9, no. 2, pp. 478-494, Jun. 2018.

[17]. Édison Massao Motoki , JoséMaria de CarvalhoFilho," Cost of Industrial Process Shutdowns Due to Voltage Sag and Short Interruption", 2021 by the authors. Licensee MDPI, Basel, Switzerland.

[18]. M. Castilla, J. Miret, A. Camacho, J. Matas and L. García de Vicuña, "Voltage Support Control Strategies for Static Synchronous Compensators Under Unbalanced Voltage Sags," in IEEE Transactions on Industrial Electronics, vol. 61, no. 2, pp. 808-820, Feb. 2014.

[19]. Ashad Ullah Qureshi , "Analysis of DVR in Distribution during Voltage Sags & Voltage Swells",Department of Electrical & Electronics Engineering SCOPE COLLEGE OF ENGINEERING, BHOPAL APRIL - 2016.

[20]. Stade, E., Fourier Analysis, John Wiley & Sons, Ltd, 2005.

[21]. Brigham, E., Fast Fourier Transform and Its Applications, Prentice-Hall, 1988.

[22]. Vainio, O., Ovaska, S.J. and Polla, M., 'Adaptive Filtering Using Multiplicative General Parameters for Zero- Crossing Detection'. IEEE Transactions on Industrial Electronics, 50(6), December 2003, 1340–1342.

[23]. K. De Brabandere, T. Loix, K. Engelen, B. Bolsens, J. Van den Keybus, J. Driesen, and R. Belmans, "Design and operation of a phase-locked loop with Kalman estimator-based filter for single-phase applications", Annual Conference of the IEEE on Industrial Electronics (IECON), Paris, France, 2006, pages 525–530.

[24]. T. Auspitzer, D. Guicking, and S. J. Elliott, "Using a fast-recursive-leastsquares algorithm in a feedback-controller," IEEE ASSP Workshop Applications Signal Processing Audio Acoustics, 1995.

[24]. D. Guicking and R. Schirmacher, "A broadband active noise control system using a fast RLS algorithm," in Proc. 3rd Int. Congr. Air- and Structure-Borne Sound and Vibration, vol. 2, 1994, pp. 1361–1368.

[26]. J. Matas, M. Castilla, J. Miret, L. G. de Vicuna, and R. Guzman, "Anadaptive prefiltering method to improve the speed/accuracy trade off of voltage sequence detection methods under adverse grid conditions," IEEE Trans. Ind. Electron., vol. 61, no. 5, pp. 2139–2151, May. 2014.

[27]. Mojiri, M., Karimi-Ghartemani, M. and Bakhshai, A., 'Time Domain Signal Analysis Using Adaptive Notch Filter'. IEEE Transactions on Signal Processing, 55(1), January 2007, 85–93.

[28]. Rodriguez, P. et al. Multiresonant frequency-locked loop for grid synchronization of power converters under distorted grid conditions. IEEE Trans. Ind. Electron., 2011. 58(1), p. 127–138.

[29]. S. Golestan, J. M. Guerrero, J. C. Vasquez, A. M. Abusorrah, and Y. Al-Turki "A study on three-phase FLLs," IEEE Transactions on PowerElectronics, .2018.

[30]. Rodriguez, P., Pou, J., Bergas, J., Candela, J. I., Burgos, R., and Boroyevich, D., Double Synchronous Reference Frame PLL for Power Converters Control, in IEEE 36th Power Electronics Specialists Conference (PESC)2005: Brazil. p. 1415-1421.

[31]. Nouralinejad, A., Bagheri, A., Mardaneh, M., and Malekpur M., Improving the Decoupled Double SRF PLL for Grid Connected Power Converters, in the 5th Power Electronics, Drive Systems and Technologies Conference (PEDSTC)2014: Iran. p. 347-352.

[32]. S. Nayak, S. Gurunath and N. Rajasekar, "Advanced single-phase inverse park PLL with tuning of PI controller for improving stability of grid utility using soft computing technique," 2016 Online International Conference on Green Engineering and Technologies (IC-GET), 2016, pp. 1-5, doi: 10.1109/GET.2016.7916732.

[33]. M. A. Akhtar and S. Saha, "Comparative Evaluation of different PD of TD-PLL Using Small Signal Modelling for Single Phase Grid Tied Inverters under Grid Disturbances," 2018 8th IEEE India International Conference on Power Electronics (IICPE), 2018, pp. 1-5, doi: 0.1109/IICPE.2018.8709532.

[34]. M. A. Akhtar and S. Saha, "IAE and ISE Performance Criterion Based Loop Filter Tuning of Transport Delay-Phase Locked Loop (TD-PLL) for Single Phase Grid Connected Inverters," 2018 8th IEEE India International Conference on Power Electronics (IICPE), 2018, pp. 1-5, doi: 10.1109/IICPE.2018.8709440.

[35]. F. Jiang et al., "Robustness Improvement of Model-Based Sensorless SPMSM Drivers Based on an Adaptive Extended State Observer and an Enhanced Quadrature PLL," in IEEE Transactions on Power Electronics, vol. 36, no. 4, pp. 4802-4814, April 2021, doi: 10.1109/TPEL.2020.3019533.

[36]. S. Mishra, A. Varshney and B. Singh, "Enhanced QPLL Based Position Estimation of RelSync Motor Drive for Electric Vehicle with Integrated Sources," 2021 IEEE 4th International Conference on Computing, Power and Communication Technologies (GUCON), 2021, pp. 1-6, doi: 10.1109/GUCON50781.2021.9573806.

[37]. M. İnci, M. Büyük, K. Ç. Bayındır and M. Tümay, "EPLL based controller for voltage harmonic mitigation in grid connected wind systems," 2017 4th International Conference on Control, Decision and Information Technologies (CoDIT), 2017, pp. 1157-1161, doi: 10.1109/CoDIT.2017.8102756.

[38]. M. Karimi-Ghartemani,"Linear and Pseudolinear Enhanced Phased-Locked Loop (EPLL) Structures," in IEEE Transactions on Industrial Electronics, vol. 61, no. 3, pp. 1464-1474, March 2014, doi: 10.1109/TIE.2013.2261035.

[39]. P. Chaudhary and M. Rizwan, "A three phase grid connected SPV power generating system using EPLL based control technique," 2017 Second International Conference on Electrical, Computer and Communication Technologies (ICECCT), 2017, pp. 1-6, doi: 10.1109/ICECCT.2017.8118004.

[40]. M. Karimi-Ghartemani, "Linear and Pseudolinear Enhanced Phased-Locked Loop (EPLL) Structures," in IEEE Transactions on Industrial Electronics, vol. 61, no. 3, pp. 1464-1474, March 2014, doi: 10.1109/TIE.2013.2261035.

[41]. S. Luo and F. Wu, "Improved Two-Phase Stationary Frame EPLL to Eliminate the Effect of Input Harmonics, Unbalance, and DC Offsets," in IEEE Transactions on Industrial Informatics, vol. 13, no. 6, pp. 2855-2863, Dec. 2017, doi: 10.1109/TII.2017.2679132.

[42]. S. Golestan, J. Matas, A. M. Abusorrah and J. M. Guerrero, "More-Stable EPLL," in IEEE Transactions on Power Electronics, vol. 37, no. 1, pp. 1003-1011, Jan. 2022, doi: 10.1109/TPEL.2021.3099839.

[43]. F. Wu and X. Li, "Multiple DSC Filter-Based Three-Phase EPLL for Nonideal Grid Synchronization," in IEEE Journal of Emerging and Selected Topics in Power Electronics, vol. 5, no. 3, pp. 1396-1403, Sept. 2017, doi: 10.1109/JESTPE.2017.2701498.

[44]. C. H. N. Martins, M. Geny Moreira and A. S. Vale-Cardoso, "A New Approach for EPLL-Based Frequency Estimation under Severe Disturbances," 2019 IEEE 10th Annual Information Technology, Electronics and Mobile Communication Conference (IEMCON), 2019, pp. 0862-0869, doi: 10.1109/IEMCON.2019.8936282.

[45]. S. Agrawal, D. Sharma, V. K. Gupta and R. K. Somani, "Performance Evaluation of 3-Phase 4-Wire SAPF based on Synchronizing EPLL with Fuzzy Logic Controller," 2018 2nd IEEE International Conference on Power Electronics, Intelligent Control and Energy Systems (ICPEICES), 2018, pp. 483-487, doi: 10.1109/ICPEICES.2018.8897490.

[46]. N. F. Jamaludin and A. F. Abidin, "A demodulation method with flicker power algorithm based Enhanced Phase-Locked Loop (EPLL)," 2014 IEEE Innovative Smart Grid Technologies - Asia (ISGT ASIA), 2014, pp. 204-209, doi: 10.1109/ISGT-Asia.2014.6873790.

[47]. S. Golestan, S. Y. Mousazadeh, J. M. Guerrero and J. C. Vasquez, "A Critical Examination of Frequency-Fixed Second-Order Generalized Integrator-Based Phase-Locked Loops," in IEEE Transactions on Power Electronics, vol. 32, no. 9, pp. 6666-6672, Sept. 2017, doi: 10.1109/TPEL.2017.2674973.

[48]. D. Janík, J. Talla, T. Komrska and Z. Peroutka, "Optimalization of SOGI PLL for single-phase converter control systems: Second order generalized integrator (SOGI)," 2013 International Conference on Applied Electronics, 2013, pp. 1-4.

[49]. S. Prakash, J. K. Singh, R. K. Behera and A. Mondal, "A Type-3 Modified SOGI-PLL With Grid Disturbance Rejection Capability for Single-Phase Grid-Tied Converters," in IEEE Transactions on Industry Applications, vol. 57, no. 4, pp. 4242-4252, July-Aug. 2021, doi: 10.1109/TIA.2021.3079122.

[50]. V. Blahnik, T. Kosan and J. Talla, "Control of single-phase AC/DC converter based on SOGI-PLL voltage synchronization," Proceedings of the 16th International Conference on Mechatronics - Mechatronika 2014, 2014, pp. 652-655, doi: 10.1109/MECHATRONIKA.2014.7018337.

[51]. S. Kalkoul, H. Benalla, K. Nabti and A. Reama, "Comparison Among Single-phase PLLs Based on SOGI," 2020 6th International Conference on Electric Power and Energy Conversion Systems (EPECS), 2020, pp. 118-122, doi: 10.1109/EPECS48981.2020.9304951.

[52]. H. K. Yada and M. S. R. Murthy, "Operation and control of single-phase DVR based on SOGI-PLL," 2016 IEEE International Conference on Power Electronics, Drives and Energy Systems (PEDES), 2016, pp. 1-5, doi: 10.1109/PEDES.2016.7914244.

[53]. F. Xiao, L. Dong, L. Li and X. Liao, "A Frequency-Fixed SOGI-Based PLL for Single-Phase Grid-Connected Converters," in IEEE Transactions on Power Electronics, vol. 32, no. 3, pp. 1713-1719, March 2017, doi: 10.1109/TPEL.2016.2606623.

[54]. Ke Chen, Wu Ai, Bing Chen and Yi Liu, "A simulation study on tracking and restructuring AC signals based on enhanced SOGI-PLL," 2016 IEEE Power and Energy Conference at Illinois (PECI), 2016, pp. 1-5, doi: 10.1109/PECI.2016.7459260.

[55]. M. Xie, H. Wen, C. Zhu and Y. Yang, "DC Offset Rejection Improvement in Single-Phase SOGI-PLL Algorithms: Methods Review and Experimental Evaluation," in IEEE Access, vol. 5, pp. 12810-12819, 2017, doi: 10.1109/ACCESS.2017.2719721.

[56]. J. Matas, H. Martín, J. de la Hoz, A. Abusorrah, Y. A. Al-Turki and M. Al-Hindawi, "A Family of Gradient Descent Grid Frequency Estimators for the SOGI Filter," in IEEE Transactions on Power Electronics, vol. 33, no. 7, pp. 5796-5810, July 2018, doi: 10.1109/TPEL.2017.2748920.

[57]. T. Ngo, Q. Nguyen and S. Santoso, "Improving performance of single-phase SOGI-FLL under DC-offset voltage condition," IECON 2014 - 40th Annual Conference of the IEEE Industrial Electronics Society, 2014, pp. 1537-1541, doi: 10.1109/IECON.2014.7048706.

[58]. A. Bendib, A. Chouder, K. Kara, A. Kherbachi and S. Barkat, "SOGI-FLL Based Optimal Current Control Scheme for Single-Phase Grid-Connected Photovoltaic VSIs with LCL Filter," 2018 International Conference on Electrical Sciences and Technologies in Maghreb (CISTEM), 2018, pp. 1-6, doi: 10.1109/CISTEM.2018.8613546.

[59]. D. G. Patiño, E. G. Guamá Erira, E. E. Rosero and J. R. Fuelagán, "SOGI-FLL for synchronization and fault detection in an inverter connected to the grid," 2015 IEEE PES Innovative Smart Grid Technologies Latin America (ISGT LATAM), 2015, pp. 833-838, doi: 10.1109/ISGT-LA.2015.7381264.

[60]. J. Matas, H. Martín, J. de la Hoz, A. Abusorrah, Y. Al-Turki and H. Alshaeikh, "A New THD Measurement Method With Small Computational Burden Using a SOGI-FLL Grid Monitoring System," in IEEE Transactions on Power Electronics, vol. 35, no. 6, pp. 5797-5811, June 2020, doi: 10.1109/TPEL.2019.2953926.

[61]. J. Park, D. Lee and T. L. Van, "Advanced single-phase SOGI-FLL using self-tuning gain based on fuzzy logic," 2013 IEEE ECCE Asia Downunder, 2013, pp. 1282-1288, doi: 10.1109/ECCE-Asia.2013.6579274.

[62]. D. G. Patiño, E. G. Guamá Erira, E. E. Rosero and J. R. Fuelagán, "SOGI-FLL for synchronization and fault detection in an inverter connected to the grid," 2015 IEEE PES Innovative Smart Grid Technologies Latin America (ISGT LATAM), 2015, pp. 833-838, doi: 10.1109/ISGT-LA.2015.7381264.

[63]. Q. Yan, R. Zhao, X. Yuan, W. Ma and J. He, "A DSOGI-FLL-Based Dead-Time Elimination PWM for Three-Phase Power Converters," in IEEE Transactions on Power Electronics, vol. 34, no. 3, pp. 2805-2818, March 2019, doi: 10.1109/TPEL.2018.2839659.

[64]. K. R. Patil and H. H. Patel, "Performance of shunt active power filter with DSOGI-FLL Under distorted grid voltage," 2017 Second International Conference on Electrical, Computer and Communication Technologies (ICECCT), 2017, pp. 1-6, doi: 10.1109/ICECCT.2017.8117997.

[65]. X. Mu, Y. Wang, R. Zhao and H. Xu, "Dual second-order generalized integrator based synchrophasor measurement and power-angle calculation under complicated grid conditions," The 16th IET International Conference on AC and DC Power Transmission (ACDC 2020), 2020, pp. 1604-1611, doi: 10.1049/icp.2020.0022.

[66]. D. Venkatramanan and V. John, "Dynamic Phasor Modeling and Stability Analysis of SRF-PLL-Based Grid-Tie Inverter Under Islanded Conditions," in IEEE Transactions on Industry Applications, vol. 56, no. 2, pp. 1953-1965, March-April 2020, doi: 10.1109/TIA.2019.2962763.

[67]. P. Marchi, F. Messina, L. R. Vega and C. G. Galarza, "A single-phase dynamic phasor estimation system: Analysis of performance and computational cost," 2016 IEEE Electrical Power and Energy Conference (EPEC), 2016, pp. 1-6, doi: 10.1109/EPEC.2016.7771764.

[68]. E. V. Appleton. Automatic synchronization of triode oscillators.Proc. Cambridge Phil. Soc., Vol. 21, No. 3, pp. 231, 1923.

[69]. H. de Bellescize. La reception synchrone. Onde Electr., 11, pp. 230-240, 1932.

[70]. A. B. Gregene, H. R. Camenzind. Frequency-selective integrated circuits using phase-lock techniques. IEEE Journal of Solid-State Circuits, Vol.4, No.4, pp. 216-225, 1969.

[71]. S. Ali, I. Setiawan and S. Handoko, "Design and Performance Test of Three Phased Synchronous Reference Frame-Phase Locked Loop (SRF-PLL) using DSPIC30F4011," 2018 5th International Conference on Information Technology, Computer, and Electrical Engineering (ICITACEE), 2018, pp. 51-56, doi: 10.1109/ICITACEE.2018.8576978.

[72]. T. Messo, J. Sihvo, D. Yang, X. Wang and F. Blaabjerg, "Improved delayed signal cancellation-based SRF-PLL for unbalanced grid," 2017 IEEE Energy Conversion Congress and Exposition (ECCE), 2017, pp. 3103-3110, doi: 10.1109/ECCE.2017.8096566.

[73]. S. Golestan, J. M. Guerrero, and J. C. Vasquez, “Three-phase PLLs: Areview of recent advances,” IEEE Transactions on Power Electronics, vol. 32, no. 3, pp. 1894-1907, Mar. 2017.

[74]. V. Kaura and V. Blasco, “Operation of a phase locked loop system under distorted utility conditions,” IEEE Trans. Ind. Appl., vol. 33, no. 1, pp. 58– 63, Jan./Feb. 1997.

[75]. M. A. Akhtar and S. Saha, "Comparative Evaluation of different PD of TD-PLL Using Small Signal Modelling for Single Phase Grid Tied Inverters under Grid Disturbances," 2018 8th IEEE India International Conference on Power Electronics (IICPE), 2018,pp.15,doi:10.1109/IICPE.2018.8709532.

[76]. Golestan, S.; Ebrahimzadeh, E.; Guerrero, J.M.; Vasquez, J.C. An Adaptive Resonant Regulator for Single-Phase Grid-Tied VSCs. IEEE Trans. Power Electron. 2018, 33, 1867–1873, doi:10.1109/tpel.2017.2736945.

[77]. Rodríguez, P.; Luna, A.; Candela, I.; Mujal, R.; Teodorescu, R.; Blaabjerg, F. Multiresonant Frequency-Locked Loop for Grid Synchronization of Power Converters Under Distorted Grid Conditions. IEEE Trans. Ind. Electron. 2010, 58, 127–138, doi:10.1109/tie.2010.2042420

[78]. Z. Xin, R. Zhao, F. Blaabjerg, L. Zhang, and P. C. Loh, “An improved fluxobserver for field-oriented control of induction motors based on dual second-order generalized integrator frequency-locked loop,” IEEE J.Emerging Sel. Top. Power Electron., vol. 5, no. 1, pp. 513–525, Mar. 2017.

[79]. R. Zhao, Z. Xin, P. C. Loh, and F. Blaabjerg, “A novel flux estimator based on multiple second-order generalized integrators and frequency-locked loop for induction motor drives,” IEEE Trans. Power Electron., vol. 32, no. 8,pp. 6286–6296, Aug. 2017.

[80]. Hong, P., M. Turk, and T.S. Huang. Gesture modeling and recognition using finite state machines. in Proceedings Fourth IEEE Int. Conf. on Automatic Face and Gesture Recognition (Cat. No. PR00580). 2000.

[81]. Typhoon HILInc. Available online: https://www.typhoon-hil.com/documentation/typhoon-hil-hardware-manual/hil46_series_user_guide/topics/hil4-6_abstract.html.2021